Influence of the substrate rheology on cell crawling

Haythem Chelly

THÈSE

Pour obtenir le grade de

DOCTEUR DE L'UNIVERSITÉ GRENOBLE ALPES

Spécialité : 2MGE : Matériaux, Mécanique, Génie civil, Electrochimie

Arrêté ministériel : 25 mai 2016

Présentée par

Haythem CHELLY

Thèse dirigée par **Claude VERDIER**,Directeur Fed3G (FR 3345), Université Grenoble Alpes
et co-encadrée par **Jocelyn ETIENNE**,Chargé de Recherches, Université Grenoble Alpes
et **Pierre RECHO**, CNRS

préparée au sein du **Laboratoire Laboratoire Interdisciplinaire de Physique**
dans **l'École Doctorale I-MEP2 - Ingénierie - Matériaux, Mécanique, Environnement, Energétique, Procédés, Production**

Influence de la rhéologie du substrat sur le rampement cellulaire

Influence of the substrate rheology on cell crawling

Thèse soutenue publiquement le **16 décembre 2021**, devant le jury composé de :

Monsieur Claude VERDIER
DIRECTEUR DE RECHERCHE, CNRS délégation Alpes, Directeur de thèse
Monsieur Davide AMBROSI
PROFESSEUR, Politecnico di Torino, Rapporteur
Monsieur Philippe MARCQ
MAITRE DE CONFERENCE HDR, Sorbonne Université, Rapporteur
Madame Alice NICOLAS
DIRECTRICE DE RECHERCHE, CNRS délégation Alpes, Présidente
Monsieur Christian GEINDREAU
PROFESSEUR DES UNIVERSITES, Université Grenoble Alpes, Examinateur
Monsieur Matthieu CARUEL
MAITRE DE CONFERENCE, Université Paris 12 - Val de Marne, Examinateur

UNIVERSITÉ GRENOBLE ALPES

Abstract

Laboratoire Interdisciplinaire de Physique

Doctor of Philosophy

Influence of the substrate rheology on cell crawling

by Haythem CHELLY

The mechanical scaffold of most eukaryotic cells is constituted of a cross-linked biopolymer meshwork that forms a skeleton connected to the substrate by dynamic bonds. Using energy derived from their metabolism, cells have the ability to move on various surfaces by self-organizing molecular motors (i.e. active cross-linkers) to produce traction forces and restructure their skeleton through a chemical treadmilling process. Such crawling motion can largely be affected by the physical nature of the substrate. Part of this interaction is due to the chemical affinity between the proteins insuring the cell adhesion and the substrate coating proteins. In the presence of traction forces applied by the cell skeleton, the ensuing bonding and debonding process leads to a complex effective friction law between the cell and its substrate over the long timescale relevant for cell motility. However, the substrate mechanical deformation also plays an important role as it feedbacks on the traction forces and thus restructures the cell skeleton flow. To illustrate some principles of this mechanical reciprocity, we investigate three prototypical situations where the effective friction law is considered in its simplest linear form but the substrate is allowed to deform. First, we analyze the case of a cell moving on a linear elastic substrate and show that even in the context of a linear friction, the global velocity of the cell depends on the substrate stiffness in a non-linear biphasic fashion. Second we consider a cell moving on a viscous substrate and characterize the renormalization of the effective linear friction by the substrate viscosity. Finally, we show that the limit of a vanishing friction coefficient leads to a generic cell motion that is independent of the substrate rheology and has a variational structure. The dynamics of the cell in this context can thus be viewed as minimizing a certain quasi-potential. With such tool, we characterize the metastability of cell substrate-independant cell crawling and show that cells can alterante their gait in the presence of a small biological noise.

UNIVERSITÉ GRENOBLE ALPES

Résumé

Laboratoire Interdisciplinaire de Physique

Doctorat

Influence de la rhéologie du substrat sur la motilité cellulaire

par Haythem CHELLY

La structure mécanique de la plupart des cellules eucaryotes est constitué d'un maillage de biopolymères réticulés qui forme un squelette relié au substrat par des liaisons dynamiques. En utilisant l'énergie dérivée de leur métabolisme, les cellules ont la capacité de se déplacer sur diverses surfaces en auto-organisant des moteurs moléculaires (c'est-à-dire des réticulateurs actifs) pour produire des forces de traction et restructurer leur squelette par un processus chimique de "treadmilling". Ce mouvement de reptation peut être largement affecté par la nature physique du substrat. Une partie de cette interaction est due à l'affinité chimique entre les protéines assurant l'adhésion des cellules et les protéines de revêtement du substrat. En présen–ce de forces de traction appliquées par le squelette cellulaire, le processus d'attache–ment et de détachement qui s'ensuit conduit à une loi de friction effective complexe entre la cellule et son substrat sur une échelle de temps longue pertinente pour la motilité cellulaire. Cependant, la déformation mécanique du substrat joue également un rôle important car elle rétroagit sur les forces de traction et restructure ainsi le flux du cytosquelette. Pour illustrer certains principes de cette réciprocité mécanique, nous étudions trois situations prototypiques où la loi de friction effective est considérée dans sa forme linéaire la plus simple mais où le substrat peut se déformer. Premièrement, nous analysons le cas d'une cellule se déplaçant sur un substrat élasti–que linéaire et nous montrons que même dans le contexte d'une friction linéaire, la vitesse globale de la cellule dépend de la rigidité du substrat d'une manière biphasique non linéaire. Ensuite, nous considérons une cellule se déplaçant sur un substrat visqueux et caractérisons la renormalisation de la friction linéaire effective par la viscosité du substrat. Enfin, nous montrons que la limite d'un coefficient de friction nul conduit à un mouvement cellulaire générique qui est indépendant de la rhéologie du substrat et possède une structure variationnelle. La dynamique de la cellule dans ce contexte peut donc être vue comme la minimisation d'un quasi-potentiel. Avec un tel outil, nous caractérisons la métastabilité de la réptation cellulaire indépendante du substrat et montrons que les cellules peuvent modifier leur démarche en présence d'un petit bruit biologique.

Remerciements

Ma grand-mère disait: "Rappelle toi toujours des personnes qui étaient là pour toi dans la difficulté." Dans cette épreuve difficile qu'était cette thèse, j'ai eu la chance d'avoir le soutien de beaucoup, et qu'ils soient rappelés dans ces "remerciements" n'est que la moindre des choses, car ils méritent bien plus que ces simples mots.

Maman, au moment où j'écris ces lignes tu es dans la chambre mitoyenne et ta simple présence est apaisante. Dès que tu a su qu'il ne me restait que quelques semaines pour rendre mon manuscrit, tu n'as pas hésité une seconde et tu as pris le train de Paris pour me rejoindre à Grenoble. Alors que j'ai 35 ans maintenant, tu me vois toujours comme ton petit garçon, dont il faut que tu t'occupes... et c'est plaisant. Mais c'est à moi de m'occuper de toi maintenant, à moi de te faire profiter des choses dont tu t'es privée pour nous et à ton tour de te reposer. Je t'aime fort.

Pierre, Claude et Jocelyn, rien n'aurait été possible sans votre aide. Vous vous rendiez toujours disponible pour discuter, me guider, que ce soit sur des questions scientifiques, administratives ou personnelles, vous n'étiez jamais avares en conseils... et ce, même le week-end. Bien que je n'ai qu'un an de différence avec toi Pierre, et que je sois le premier doctorant que tu encadres, tu t'es investi pleinement dans ce rôle et tu as su comment me gérer pour que je puisse donner le meilleur de moi-même. Tu m'as appris énormément de choses et transmis des bonnes méthodes de travail, ce sont des enseignements et des compétences qui me seront bénéfiques toute ma vie, et ça n'a pas de prix. Même si nous avions par moment des petits désaccords, tu as toujours fais les choses dans mon intérêt sans rien attendre en retour et pour ça et bien d'autres choses je te serais toujours reconnaissant. Tu as fais un travail formidable. Claude, dès le début de ma thèse, tu as fait en sorte que mon environnement de travail et de vie soit des plus agréables. En particulier lorsque ma première propriétaire a voulu m'extorquer de l'argent, ni une ni deux, qu'on se retrouvait dans ta voiture et que tu lui mettais un coup de pression. Tu as passé beaucoup de temps à m'initier aux protocoles expérimentaux afin que je puisse mieux apréhender la théorie, cela à d'autant plus de valeur à mes yeux, sachant la charge de travail que tu avais en parallèle. Jocelyn, tu as toujours su trouver les mots pour me remonter le moral pendant les périodes de doutes et de remises en question. De par ton intelligence émotionnelle et ta sagesse, peu importe l'état dans lequel je me trouvais avant de te parler, je ressortais toujours en confiance et plus motivé que jamais de nos discussions. Quant à l'enseignement que tu m'as prodigué sur les aspects numériques il est pour moi d'une valeur inestimable. Merci Pierre, Claude et Jocelyn, de m'avoir encadré et d'avoir été si patient avec moi, je me rends compte de la chance que j'ai eu de vous avoir en tant qu'encadrants.

Merci à toi Papa de m'avoir donné goût à la science depuis mon plus jeune âge. À vous, Ikram, Nader et Emir, vous avez tout fait pour m'alléger de certaines responsabilités pour que je puisse me consacrer à cette thèse, vous êtes mon soutien indefectible en tout temps. Souleyman, tu es venu au monde il y a peu et pourtant tu

me soutiens déjà à ta manière. Tes sourires me suffisent à recouvrer ma motivation. Hélas je n'ai pas pu profiter de toi autant que je le voulais ces derniers temps, mais je vais me rattraper promis :). Je te souhaite de devenir une bonne personne, humble, altruiste et généreuse. Je te fais plein de gros bisous sur tes p'tites joues.

Merci à Sofiane, Mohamed, Richard et Bruno qui venaient prendre la température ou même le pouls par moment et spécialement à Arthur, Adel et Damien, qui veillaient à ce que je ne manque de rien.

Et il y a ceux qui ne sont plus là pour lire ces remerciements, qui pour la plupart nous ont quitté pendant la période de ma thèse, à savoir mes grands-parents, ma tante, mon cousin et ma cousine, je vous remercie pour tout ce que vous avez fait pour moi tout au long de votre vie, et je vous souhaite d'être apaisés là où vous êtes.

Et je n'oublie pas même ceux que j'ai oublié :).

Contents

Chapter 1

Introduction

1.1 Context, background importance of the topic

Cell migration is essential in a wide range of physiological and pathological processes, as morphogenesis, wound healing, tumor metastasis and immune response. Therefore understanding cell motility is critical to develop adequate treatments to cure cancer metastasis, to design new matrices for regenerative tissue engineering and to engineer microcrawlers to achieve localized drug delivery.

1.1.1 The cytoskeleton

The cell can be roughly considered as constituted by a membrane containing, the cytoplasm, a nucleus and a *cytoskeleton*. The cytoskeleton represents the cell machinery responsible of its mechanical behavior, and is constituted of a meshwork of filamentous proteins that regulates the cell shape, morphology, stiffness, mechanical stability and drives its motility. Three different types of biopolymers compose the cytoskeleton filamentous network, namely *actin filaments*, *intermediate filaments* and *microtubules* (see Fig. 1.1).

The actin cytoskeleton is of primary importance in the cell motility and is the only one considered in this work. The polymerization of actin monomers, called *G-actin*, induces the formation of the two-stranded helical polymers constituting the actin filaments or *F-actin*. The polymerization of G-actin is an active process, as many other phenomena occurring within the cell, meaning that energy is needed in order for the process to take place at the rates observed in living cells. This energy is produced within the cell by the hydrolysis of adenosine triphosphate (ATP). The actin filament is polarized as it exhibits a plus and minus end, respectively the *barbed* and *pointed* end, where the plus end growth is faster than the one of the minus end (*Molecular biology of the cell.* 2008). This growth discrepancy between the two ends gives rise to a *treadmilling* phenomenon at steady-state, where the polymerization rate at the plus end compensates the depolymerization rate at the minus end. Thus the treadmilling motion constitutes a depolymerization/polymerization-driven motion at constant filament length. Filaments themselves can organize into a highly cross-linked planar protrusion located at the cell leading edge, called *lamellipodium*, as well as in *dorsal- ventral stress fibers*, which are basically thick cables of F-actin that

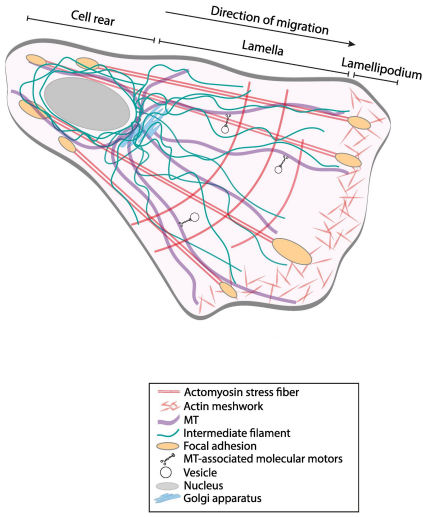

FIGURE 1.1: Schematic representation of a cell and its constituants (Seetharaman and Etienne-Manneville, 2020).

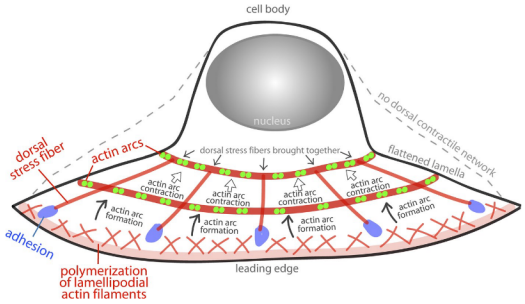

FIGURE 1.2: Arcs dynamics in a crawling cell (Burnette et al., 2014)

exerts traction force on the substrate through anchoring points or in actin arcs that linked dorsal stress fibers together (see Fig. 1.2).

Other essential components of the cytoskeleton are *myosin II* molecular motors, which are categorized as such, because they convert the chemical energy obtained from ATP hydrolysis into a power-stroke mechanical work. A motor is made of a *head* and a *tail* and can assembles with other motors by the tail to form a bipolar filament with heads at both ends of the assembly. The motors are either freely diffusing in the cytoplasm or cross-linking two actin filaments. When attached, the heads of a bipolar filament experience a conformational change creating a power stroke which induces parallel sliding of the cross-linked actin filaments (see Fig. 1.3). The molecular motors are the cause of cell contractility, which is a keystone of the cell motility along with the previously mentioned polymerization.

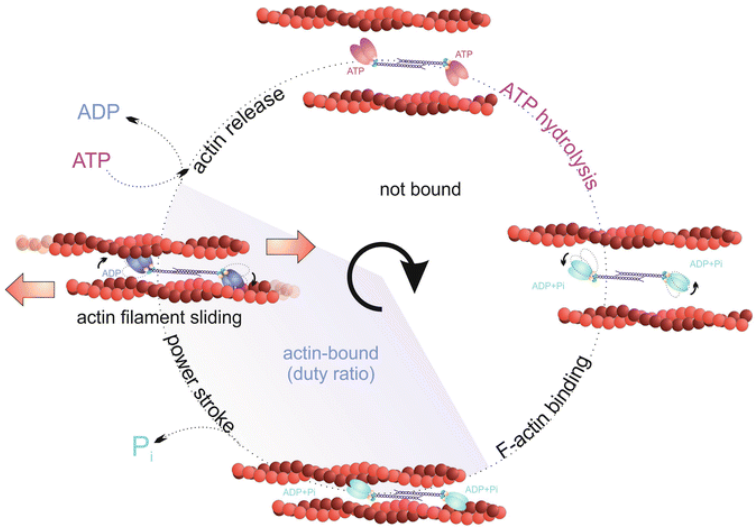

FIGURE 1.3: Myosin active actin-crosslinking (Juanes-García, Llorente-González, and Vicente-Manzanares, 2018)

1.1.2 Influence of the ECM mechanical properties on cell functions

Abundant evidence shows that the extracellular matrix (ECM) can no longer be considered only as a rigid structure simply supporting cell migration. Instead it is now clear that the mechanical properties of the ECM significantly influence a range of cell functions. Therefore cell dynamics cannot in general be considered independently of the substrate when studying its migration for example. A few examples of such complex interplay between the cell and the matrix are listed below.

During the process of embryogenesis, stem cells evolving on soft matrices differentiate into a neurogenic lineage (neuron-like), on rigid matrices they differentiate into an osteogenic lineage (bone-like), while at intermediate elasticity they differentiate into a myogenic lineage (muscle-like) (Engler et al., 2006). Another general effect is the preferred cell migration from zones of lower substrate rigidity to zones of higher substrate rigidity following a process called durotaxis (Lo et al., 2000). Furthermore, Peyton and Putnam, 2005 showed that cells exhibit maximal velocity at an intermediate matrix stiffness. Later on, Reinhart-King, Dembo, and Hammer, 2008 discovered a mechanical communication process between two or more cells through a two dimensional compliant substrate. They found that cells react to substrate deformations induced by the traction forces exerted by neighboring cells and transmitted *via* the substrate. Therefore the more compliant the substrate is, the wider the communication range is. These results were later on also confirmed in a three dimensional extracellular environment (Ma et al., 2013). Finally, Solon et al., 2007 linked the cell's internal stiffness to the one of the substrate, as on soft matrices the cell rigidity matched the substrate one while it reached a plateau above a substrate rigidity threshold ($\sim$ 20 kPa).

These examples constitute strong evidence that the mechanical properties of the ECM has an impact on a wide variety of cell functions and also suggest that the

cell is able to sense its mechanical environment (*mechanosensing*) and adapt its response accordingly. This dynamic bidirectional interaction between the cell and the ECM, consisting of sensing the mechanical cues, then transmitting them (*mechanotransduction*) to the cell to finally adapt its behaviour according to these physical cues, is termed as *mechanoreciprocity* or *mechanical reciprocity* (Roskelley and Bissell, 1995; Dado and Levenberg, 2009; Schultz et al., 2011; Van Helvert, Storm, and Friedl, 2018).

A disruption in the mechanical reciprocity pathway, whether in the mechanosensors, the mechanotransducers or the actuators (the module or component actively governing the mechanical response of the cell, such as the cytoskeleton, the adhesions...), can provide pathological conditions to the triggering or expansion of diseases, such as cancers and cardiovascular diseases among others. An abnormal response to physical cues can also be the cause of developmental disorders, such as Hutchinson-Gilford progeria syndrome, characterized by a dramatically fast ageing (Dufort, Paszek, and Weaver, 2011). Cancers are often associated with fibrosis, an excessive formation of extracellular matrix, and is proven to be an important factor in its initiation, growth and metastasis (Haak, Tan, and Tschumperlin, 2018). During wound healing or inflammation, myofibroblasts restore the mechanical integrity of the tissue and in the physiological conditions they should revert to their initial phenotype (fibroblasts) or eventually die, by detaching themselves from the substrate (anoikis), as soon as the homeostasis is reached. However, when they fail to correctly interpret or respond to the mechanical cues of the ECM, myofibroblasts do not revert to fibroblasts, instead they further differentiate into a much more active phenotype than myofibroblasts, referred to *cancer-associated fibroblasts* (Chandler et al., 2019), which will contribute to excessive stiffening of the ECM by producing even more ECM proteins. This is one reason why tumors are stiffer than healthy tissues. The feedback loops associated with physiological and pathological behaviour of fibroblasts in case of disruption of the tissue mechanical integrity are represented Fig. 1.4 (Humphrey, Dufresne, and Schwartz, 2014). Because cancer mimics the chronic inflammation it is referred to as a "wound that does not heal" (Dvorak, 1986; Schäfer and Werner, 2008).

As discussed above, because of the mechanical reciprocity, increased ECM stiffness is a catalyst of various diseases. Based on this observation a new and promising field of the medicine has emerged, the *mechanomedicine*. It aims at providing a therapeutic treatment, by either targeting the ECM mechanical properties or by altering the mechanoreciprocity pathway (Lampi and Reinhart-King, 2018).

1.1.3 Focal adhesion: main actor of the mechanoreciprocity

As mentioned above, the mechanical reciprocity first relies on the mechanosensing. If the cell is unable to feel its mechanical environment, obviously it can not adapt to it. The main sensing machinery of the cell lies at the contact between the cell and its

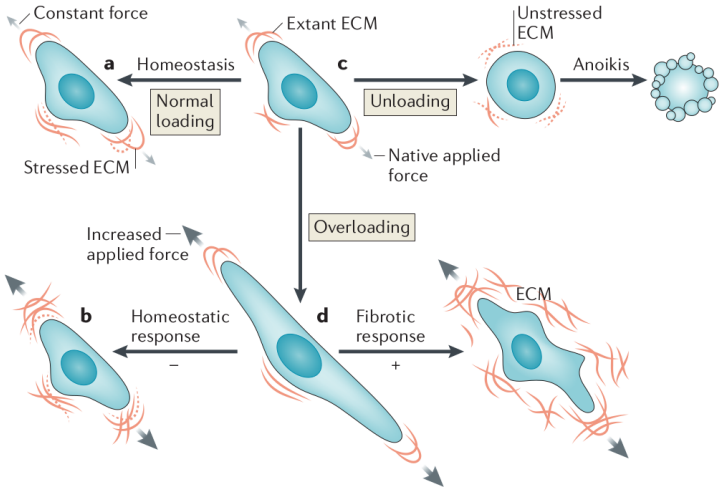

FIGURE 1.4: Tensional homeostasis disruption (Humphrey, Dufresne, and Schwartz, 2014)

substrate and is mediated by so-called focal adhesions (FAs) linking the cell cytoskeleton and its actin meshwork to the substrate. A comprehensive review of focal adhesions can be found in Geiger, Spatz, and Bershadsky, 2009. FAs are constituted by a myriad of proteins interacting with each other in order to integrate mechanical cues, such as ECM rigidity and external forces. Within this protein assembly, some act as mechanosensors as they undergo conformational changes in response to mechanical stimuli. Among them, the most studied ones are *integrin*, *talin* and *p130Cas*. Their combination forms a module, which mechanically links the actin cytoskeleton to the ECM (see Fig. 1.5). Integrins are transmembrane proteins, that can either be in an inactive or active state and must be activated in order to be able to bind to substrate-coating proteins, such as fibronectin. The integrin is activated when "brushed" by the flow of actin. Once bound to the ECM, another mechanosensitive protein, talin, binds to the inner part of integrin. This assembly constitutes a so-called *nascent adhesion* or *focal complex* and is highly unstable. Above a load threshold, talin experiences force-dependent unfolding, unraveling a binding site for vinculin, which in turn promotes the clustering of integrins and the binding of actin filaments at its tail. In parallel, the p130Cas also experiences force-dependent stretching which will indirectly trigger a sequence of events transducing the mechanical signal into a biochemical one, such as the activation of RhoGTPase, which will induce cytoskeleton contractility and polymerization.

Force-dependent conformational changes of mechanosensing proteins, trigger the clustering of integrins as well as the production of RhoGTPase proteins, which in turn increase the contractile activity and polymerization of the cytoskeleton, yielding an increased mechanical load in the adhesion, thus ultimately reinforcing the focal adhesion and the production of cytoskeleton-regulating proteins by re-entering the loop (see Fig. 1.6). This loop is essential to the adhesion maturation process and indirectly to other cell functions using adhesion, such as migration, differentiation...

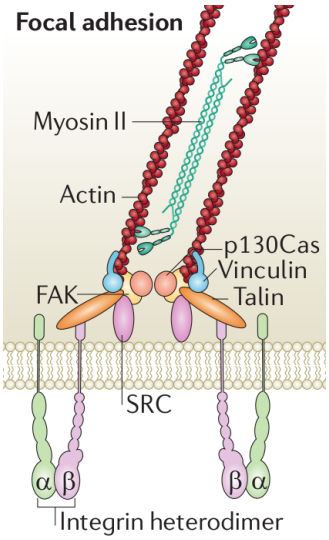

FIGURE 1.5: Constitution of a focal adhesion (Dufort, Paszek, and Weaver, 2011).

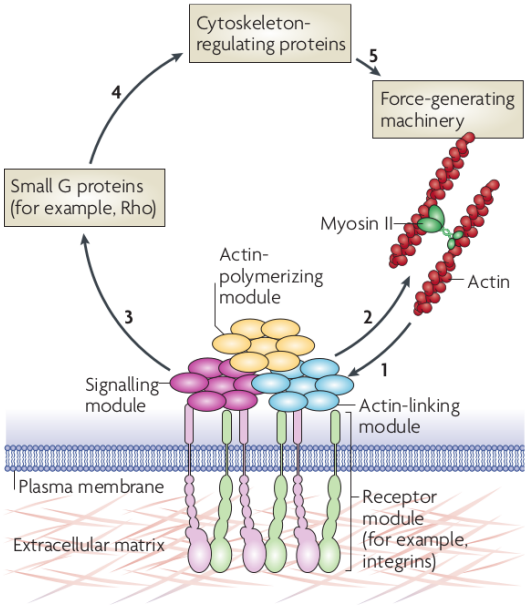

FIGURE 1.6: Schematic representation of the mechanical reciprocity with a positive feedback loop between (Geiger, Spatz, and Bershadsky, 2009).

This positive feedback loop and more generally the focal adhesion constitutes an important block of the mechanoreciprocity at a molecular level, as it involves the mechanosensing *via* the sensory module composed by integrin, talin, vinculin and p130Cas (among others), mechanostransduction *via* the production of cytoskeleton regulating proteins (such as RhoGTPase) and finally the cell response *via* the rearrangement of the cytoskeleton.

It has been experimentally observed that cells develop more stable and mature adhesions on stiff substrates than on soft ones (Discher, Janmey, and Wang, 2005) (see Fig. 1.7), and eventually fail to attach on too soft substrates.

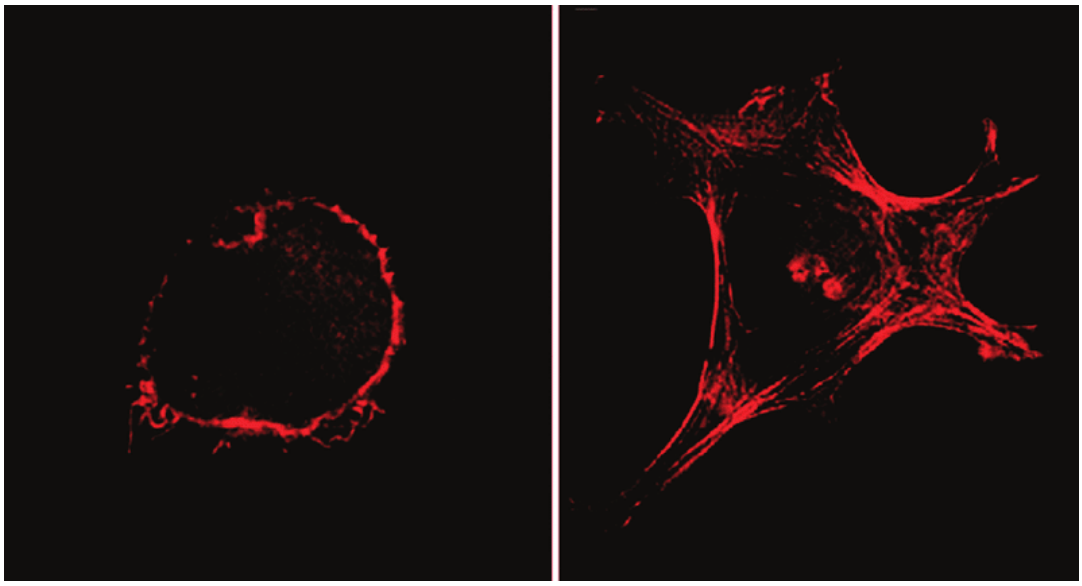

FIGURE 1.7: Cell on a soft substrate (left) and on a stiff substrate (right) (Discher, Janmey, and Wang, 2005).

This phenomenon is a direct consequence of the FA-related mechanoreciprocity and can be explained with the motor-clutch model (see Fig. 1.8). At the front of the cell, actin monomers (*G-actin*) polymerize into actin filament (*F-actin*), due to the presence of *Arp2/3* proteins in the vicinity of the cell membrane, resulting in a forward motion of the membrane. As the actin polymerization rate is very high at the tip of the cell and the tension of the membrane opposes its extension, a *retrograde flow* of actin from the front towards the center of the cell is generated. Meanwhile depolymerization of the actin filament into actin monomers occurs in the bulk, where molecular motors (*myosin II*) pull actin filaments backwards and therefore also contribute to the retrograde flow.

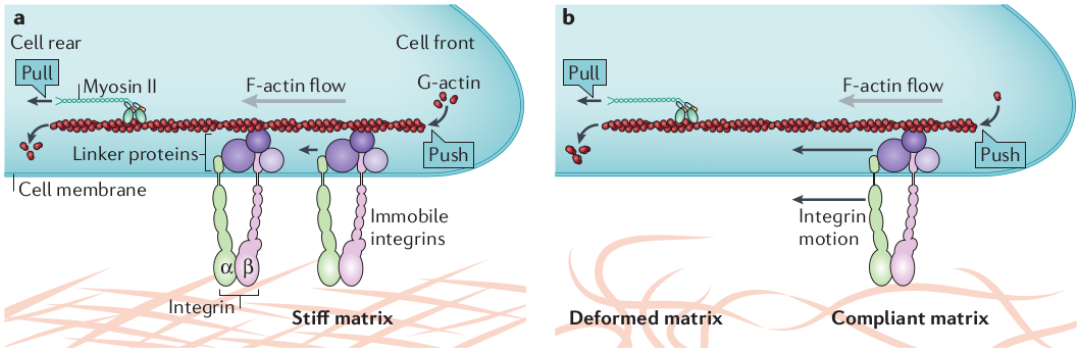

FIGURE 1.8: Motor-clutch model on stiff and soft extracellular matrix

If the anchorage of focal adhesions in the ECM is fixed, e.g. in a stiff matrix, the retrograde flow thus generates a large loading rate of the focal adhesions. This can trigger the positive feedback loop of mechanoreciprocity discussed above. However on a soft substrate, there will be a greater matrix deformation under the traction

forces exerted by the cell. Thus, the loading rate of the FA is small and can therefore be insufficient to trigger the positive feedback loop which would result in the maturation of the adhesion, instead adhesions stay in a nascent state and eventually spontaneously vanish (Pelham and Wang, 1997).

1.1.4 Cell migration

Depending on the cell phenotype different locomotion modes can be adopted.

The cell crawling motion is achieved by the combination of different phenomena and is classically represented by a four-step cycle (see Fig. 1.9), according to Abercrombie, 1980. First a protrusion extends at the leading edge of the cell. This protrusion, called lamellipodium, is the result of the polymerization of actin (G-Actin) into actin filament bundles (F-actin) in the vicinity of the cell membrane, pushing the membrane forward. As explained above, both the reaction force of the membrane and the action of molecular motors combine to generate a *retrograde flow* of actin from the lamellipodium towards the center of the cell. Next, the lamellipodium adheres to the substrate the cell is evolving on, first through small short-lasting nascent adhesions, which after a maturation process may evolve to form stable focal adhesions. After that, the cell contracts through the action of molecular motors (myosin II), which can bind to two actin filament and pull them together. Due to the contractile forces, the FAs at the rear of the cell detaches inducing an overall motion of the cell forward.

It has been experimentally observed that cells exhibit a maximal speed on substrates of intermediate stiffness (Peyton and Putnam, 2005). This can be explained by the previously described reinforcement of the FAs due to the bidirectional interaction between the cytoskeleton and substrate. Indeed, because the cell develops more stable and mature adhesion on stiff substrates, this tends to resist to the cell motion, while on very soft substrates, adhesions are too weak for the cell to be able to transmit traction forces to the substrate effectively, which explains the biphasic behaviour of the cell speed with respect to the substrate stiffness.

From another perspective Palecek et al., 1997 experimentally extracted a biphasic relationship between cell speed and adhesion density. At too low adhesion density the cell is unable to form stable adhesion, while at too high adhesion density the cell is able to enter the FA reinforcement loop and eventually results in stable adhesions resisting the cell motion.

The present section has highlighted the importance of considering the cell and the ECM together, because of the mechanical crosstalk occurring between them and the large influence this mechanoreciprocity has on many fundamental cell functions, such as adhesion and migration. While a broad range of the literature does not address the cell-ECM mechanoreciprocity, by considering cell migration on rigid substrates, in the next section, we establish a non-exhaustive list of the physical modeling attempts to simulate or understand cell migration on compliant substrates.

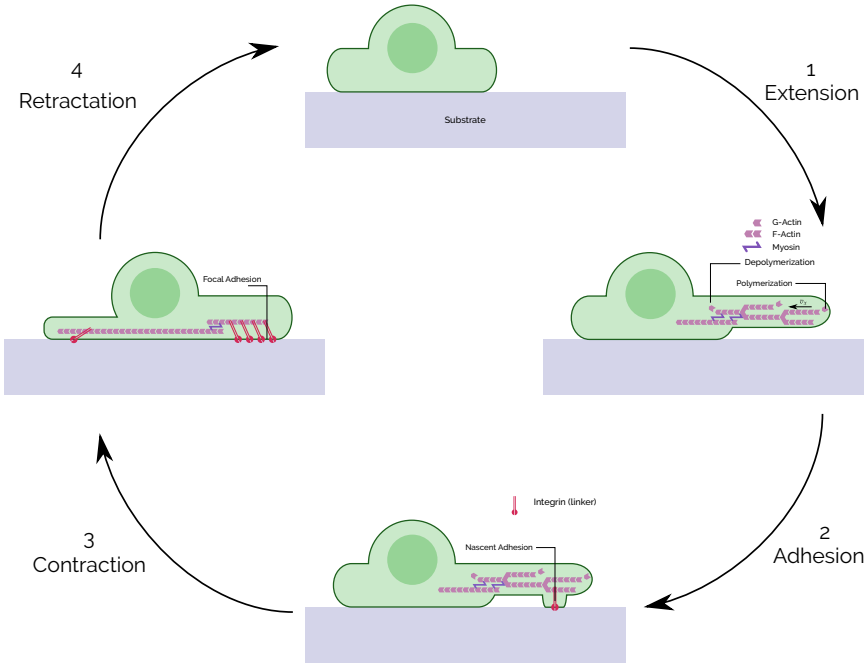

FIGURE 1.9: Cell motility steps

1.2 Models of single cell migration on a compliant substrate

Modeling cell migration on a compliant substrate requires to model the cell, the substrate and the interaction between them. We roughly distinguish two categories, namely microscopic and macroscopic descriptions.

1.2.1 Microscopic description

The microscopic description or agent-based modeling focuses on modeling the different agents and their interactions at the molecular scale, based on the available informations on the agents. Starting from the molecular scale, two bottom-up approaches can be implemented in order to build large-scale theories, one is based on analytical statistical tools, such as the mean-field theory, the other is based on computational stochastic simulations, such as Monte-Carlo simulations.

Minimal agent-based models of sliding friction have been explored by Srinivasan and Walcott, 2009; Li, Bhimalapuram, and Dinner, 2010; Sabass and Schwarz, 2010; Sens, 2013 to investigate the interaction between a moving actin filament and stochastic bonds, based on the molecular-clutch model and inspired by the Lacker-Peskin model (Lacker and Peskin, 1986). The actin filament is considered as rigid,

integrin proteins (clutches) are modeled by hookean springs that undergo stochastic engagement and disengagement to the substrate. The mechanosensitivity is implemented, by assuming a force sensitive detachment rate obeying Bell's law (Bell, 1978).

Using a computational stochastic model, Chan and Odde, 2008 investigated the influence of the compliance of the substrate on the filament dynamics. In this model, the actin filament is pulled by molecular motors generating a retrograde flow. The filament slides at a constant velocity in the case where no clutch is engaged, else the velocity decreases as the force applied by the motor increases until the motor stall force is reached, thus following a Hill-like relationship. The forces are transmitted to the substrate through the engaged bonds. The substrate is assumed to be elastic and for sake of simplicity is modeled as a single spring of stiffness, *i.e.* only an overall displacement of the substrate is assumed.

The clutch model can predict a biphasic relationship between the applied traction force and the substrate stiffness (see Appendix D), thus the maximal force transmission is reached at an optimal substrate rigidity. It is explained by the fact that, above the optimal stiffness, the forces in the clutches increase very fast, yielding to detachment rates greater than attachment rates, therefore only a small amount of clutches are engaged and for a small amount of time. In this regime the actin velocity is high while the transmitted forces are low, these features characterize the frictional slippage regime. On the other hand, when the stiffness lies below the optimal stiffness, the forces in the clutches increase so slowly, that the bonds break before reaching high loads. From these observations Elosegui-Artola, Trepat, and Roca-Cusachs, 2018 deduced that the loading rate was the main regulator of the cell mechanosensitivity. Besides, the clutch model was also able to predict stick-slip motion at moderate loading rates when a critical force is reached the bonds fail in a catastrophic manner until no bond is left attached, next the clutch re-engage and the loop is repeated. While this basic model allows a better understanding of the mechanosensing process and replicates cell migration modes observed experimentally, the extrapolation of the results to the whole cell level is not straightforward. To overcome this limitation Bangasser et al., 2017 implemented a minimal cell model constituted of three clutch modules. The results of this model were consistent with those of a single motor clutch as an optimal rigidity for traction forces transmission emerged from the simulations.

The results show a biphasic (i.e. bell-shaped) relationship between the cell traction force and the actin velocity: at sufficiently small actin velocity, the loading in the bonds increases slowly, which leads to a linear increase of the traction force with the actin velocity. For higher actin velocity, the loading rate in the bonds is high, therefore they break very rapidly and the traction force decreases with the actin velocity. Using this microscopic approach, Sens, 2020 formulated a simple cell model consisting of two stochastic adhesion modules linked by a spring. This local non-linear dependence of the traction force on the actin velocity has been used to explain the

well-established experimental observation that the global cell velocity depends on the fibronectin ligand density in a biphasic way (DiMilla, Barbee, and Lauffenburger, 1991; Palecek et al., 1997).

These models give a biphasic behavior dictated by a nonlinear behavior of adhesion molecules.

1.2.2 Macroscopic description

The macroscopic description is a phenomenological approach aiming to capture the relevant dynamical behaviors from effective continuum theories.

As described in the previous section, the adhesion is an essential process of cell crawling. Several macroscopic models of adhesion have been proposed in the literature. An approach investigated by Stéphanou et al., 2008 consists in modeling the mechanosensitive process of adhesion formation and maturation by introducing three different steps of adhesion, namely adhesion spot, focal complex and focal adhesion, each one being characterized by its lifetime and resistance to traction. While the mechanics of the cytoskeleton is modeled using the continuum two-phase flow model (Alt and Dembo, 1999), the adhesion are modeled as discrete entities. Transport models of adhesions were also developed in order to take into account the adhesions maturation process due to integrins activation and aggregation, where integrins are transported in one of the four following states: free, actin-bound, substrate-bound and actin-substrate-bound (Palecek, Horwitz, and Lauffenburger, 1999; Möhl, 2005; Kuusela and Alt, 2009). One of the approach is based on the aforementioned observation that agent-based models of sliding friction between an actin filament and stochastics bonds resulted in a biphasic relationship between the cell traction force and the cytoskeleton retrograde flow velocity. Similarly, starting from the general trend that stationary cells generate large traction forces while showing a slow actin flow and on the contrary motile cells generate small traction forces with a fast retrograde flow, Barnhart et al., 2015 deduced that the frictional slippage is weaker at the rear of a motile cell than in stationary cells, and thus introduced a nonlinear actin flow-dependent friction coefficient to ensure a decreased cell-substrate coupling above a critical actin flow velocity. Nevertheless, the experimental observation (Schwarz and Gardel, 2012) that, below a velocity threshold, the transmitted traction force evolves linearly with the actin velocity, has led to disregard this complexity and consider the simple viscous friction law $T_x = \xi v$, where T_x represents the uniaxial traction force exerted by the cell on the substrate, v is the cytoskeleton retrograde flow velocity and ξ represents an effective viscous friction coefficient. Indeed this representation of adhesion has been extensively used in plenty of models (Jülicher et al., 2007; Rubinstein et al., 2009) and is also the one retained in the present model. Note, that by nature the force balance is bidirectional (action-reaction law) and thus encompass the focal adhesion-induced mechanoreciprocity.

Models considering the cell as a effective solid medium are suited to describe static rather than motile conditions. Falling in this category, Deshpande, McMeeking, and Evans, 2006; Deshpande, McMeeking, and Evans, 2007 developed a two dimensional model with a constitutive law with an active and passive contributions. The active stress is constructed using homogeneization techniques and is related to the dynamics of the contractile actomyosin stress fibers. Using this model the authors were able to understand more deeply the physics of adherent cells.

However, based on the observation that the cytoskeleton undergoes highly dynamic changes in the cell migration process, it has been characterized by a viscoelastic fluid-like behaviour at sufficiently large time-scales relevant for migration. Two main active drivings have been implemented in these models to reproduce cell migration of rigid substrates; distributed contraction of the molecular motors and turnover of the actin meshwork. Under the simplifying consideration that the cytoplasm is made of the cytoskeleton and a solvent, Dembo and Harlow, 1986 developed a model of interpenetrating two-phase flow model. The two phases are assumed to be Newtonian incompressible fluids. The contractility of the cytoskeleton phase is ensured by introducing an actin density-dependent negative pressure (Alt and Dembo, 1999; Kuusela and Alt, 2009). Instead of considering the solvent, Rubinstein et al., 2009 described the main components of the cytoskeleton by advection-reaction-diffusion equations on their densities. It is based on the observation that the molecular motors are advected by the polymerization and contractility-driven retrograde flow of the actin filaments. In this representation the F-actin turnover is modeled by an advection-reaction equation. The polymerization occuring at the leading edge is taken into account with a Stefan-like boundary condition. Two concentrations of molecular motors are considered, those that cross-link two fibers of the cytoskeleton, therefore advected by the skeleton retrograde flow and those freely diffusing in the cytoplasm. Assuming moreover a first-order kinetic attachment and detachment rates, the dynamics of the population of attached motors is governed by an advection-reaction equation, wheras the dynamics of the population of detached motors is governed by a diffusion-reaction equation. As for the previously introduced two-phase flow model, the active stress due to the molecular motors contractility is isotropic, acting as a negative pressure. However unlike the previous model the magnitude of this active stress is assumed to be proportional to the density of attached motors. More complex active gel models that also account for the cytoskeleton fibers orientation (Jülicher et al., 2007; Tjhung, Marenduzzo, and Cates, 2012; Giomi and DeSimone, 2014; Camley et al., 2017) have been introduced to understand various instabilities that lead to cell motion and some complex cell motion dynamics.

From another perspective which does not explicitly solve force balance within the cell, Ziebert, Swaminathan, and Aranson, 2012 modeled the cytoskeleton by an averaged orientation field of the actin filament network in a phase-field framework, which is adapted from the advected-field approach (Biben and Misbah, 2003; Biben,

Kassner, and Misbah, 2005) developed to model vesicle dynamics where the membrane is advected via hydrodynamics forces. In the phase-field approach, an auxiliary field, known as the phase-field or phase function, is introduced and is used to discriminate between the interior and the exterior of the cell. In the context of cell crawling, the cell membrane is advected by the internal forces generated by the cytoskeleton.

Several methods have been explored to introduce the influence of the rheology of the substrate on existing models of cell motility. Within the phase-field framework, Ziebert and Aranson, 2013; Löber, Ziebert, and Aranson, 2014 introduced reaction-diffusion adhesion dynamics involving a substrate displacement-dependent detachment to ensure the gripping (resp. slipping) below (resp. above) a substrate displacement critical value. While Ziebert and Aranson, 2013 used a single global spring to model the elastic substrate in the fashion of Chan and Odde, 2008, Löber, Ziebert, and Aranson, 2014 improved this previous model by locally resolving the viscoelastic incompressible substrate displacement. In these models a local traction force exerted by a cell generates a non-local displacement of the substrate under the cell and therefore induces a local reorganization of the cell cytoskeleton which ultimately impacts its motility dynamics in a non trivial way. Lelidis and Joanny, 2013 modeled the cell as a one-dimensional continuum active gel medium interacting with an elastic substrate through discrete focal adhesions. They considered a semi-infinite substrate and deduced the displacement of the substrate due to the cell traction force within a plane strain framework. Another approach is simply an extension of the previously mentioned linear viscous friction model to the case of a deformable substrate by considering the difference between the actin velocity v and the substrate velocity v^s in the friction law, such that $\boldsymbol{T} = \xi(v - v^s)$. Wong and Tang, 2011 implemented this friction law with a space-dependent friction coefficient to model the interaction between a hyperelastic cell and a finite-size hyperelastic substrate. Hassan, Biel, and Kim, 2019 also used this law combined with a phase-field model for the cell, where a migration directional bias was introduced in order to promote cell migration in the direction of increasing substrate rigidity. More recently, Zhang et al., 2020 used a similar approach with an actin polymerization bias towards substrate tensile regions (resulting from external forces or cell traction forces) to promote cell migration in these directions. Using a Cellular Potts Model, in which the phenomenological description of a cell is achieved by minimizing a functional in a subset of lattice sites representing the cell, Oers et al., 2014 inspired by the implementation of chemosensitive functions in Savill and Hogeweg, 1997, introduced an ECM mechanosensitive function in the form of Hamiltonian to capture durotaxis. This model was then extended to the migration on viscoelastic substrate by Goychuk et al., 2018.

1.3 A simple approach to model cell migration on a compliant substrate

The mechanoreciprocity is the sum of two contributions a bare mechanical and a chemo-mechanical one. When evolving on a compliant substrate the pure mechanical contribution plays an important role. Indeed the cell exerts traction forces on the substrate inducing non-local deformations of the matrix, which will in turn result in the reorganization of the cytoskeleton. In order to take into account the bare mechanoreciprocity within crawling models on a compliant substrate, the stress within the cell and the substrate must be explicitly solved. In Ziebert and Aranson, 2013, the non-local deformation of the substrate is not taken into account. While the non-locality is addressed in Löber, Ziebert, and Aranson, 2014, the stress within the cell is not explicitly solved for. Lelidis and Joanny, 2013 operate at an imposed cell velocity and in the limit where the substrate is much stiffer than the cell. In their model, Zhang et al., 2020 do not solve the force balance within the cell, and assume instead an *a priori* actin retrograde flow velocity and an actin polymerization bias towards substrate tensile regions (resulting from external forces or cell traction forces) to promote cell migration in these directions.

In the present work, we want to investigate what phenomena can be captured from a minimalistic cell migration model without introducing any *a priori* bias, in other words we want to extract the cell response to *bare* mechanical contribution of cell-ECM interaction, *i.e.* when considering the mechanical reciprocity from a pure mechanical standpoint, without integrating the mechanical effects resulting from FAs biochemical signaling.

In order to address to this issue, we generalize the minimalistic one dimensional mechanical model of Recho, Putelat, and Truskinovsky, 2015, designed to model cell migration on a rigid substrate, to the case of the migration on a compliant substrate. The cell is modeled as a thin layer (height h) of active gel slab of length $L(t) = l_+(t) - l_-(t)$, where $l_\pm(t)$ denotes the cell ends at time t, and is confined to move on a one-dimensional straight track of width δ oriented along the $x-$direction.

The orthonormal frame of reference $(\boldsymbol{e_x}, \boldsymbol{e_y}, \boldsymbol{e_z})$ is chosen such that the substrate is semi-infinite in the $\boldsymbol{e_z}$ direction and material points are labeled by the spatial coordinate $\boldsymbol{r} = (x, y, z)$. The contact interface between the cell and the substrate at time t is defined by the two-dimensional domain $\Omega_C(t) = [l_-(t), l_+(t)] \times [-\delta/2, \delta/2]$. Considering that the cell is very thin compared to its length ($h \ll L$), we assume that the cell only exerts forces tangentially to the substrate

$$\boldsymbol{T}(\boldsymbol{r}, t) = T_x(x, t)\, \boldsymbol{e_x} + T_y(x, t)\, \boldsymbol{e_y}, \tag{1.1}$$

where $\boldsymbol{r} \in \Omega_C(t)$. Since we shall project all equations in the x-direction, it will not be needed to specify T_y. Because the track is assumed to be thin ($\delta \ll L$), $T_{x,y}$ are assumed to only depend on the x-coordinate.

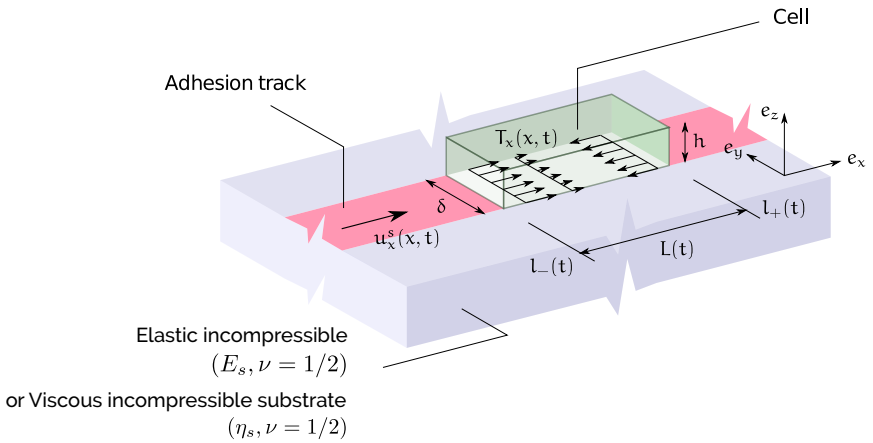

FIGURE 1.10: Scheme of the model of a cell crawling on a semi-infinite incompressible visco-elastic substrate. The thin adhesion track (in red) of width $\delta \ll L$ allows a one dimensional motion of the cell along the $x-$axis. The cell (in green), extending from l_- to l_+ exerts traction forces T_x on the substrate, inducing a displacement u_x^s of the substrate at the surface.

We consider two concentrations of molecular motors, those that cross-link two fibers of the cytoskeleton (concentration c), therefore advected by the skeleton retrograde flow (velocity v) and those that are free to diffuse (coefficent D_m) in the cytoplasm (concentration m) (Rubinstein et al., 2009). There is an attachment (rate k_a) and detachment (rate k_d) dynamics between these two populations that lead to the following coupled system:

$$\begin{cases} \partial_t c + \partial_x(cv) = k_a m - k_d c \\ \partial_t m - D_m \partial_{xx} m = k_d c - k_a m. \end{cases} \tag{1.2}$$

While we assume that the rate of detachment k_d is fixed, the rate of attachment $k_a = k_a^0 g(c)$ decreases with the concentration c because of steric hindrance. The function $g(c)$ is therefore positive and decreasing to zero as c becomes large.

Assuming that the system remains close to its chemical equilibrium because the rates are large compared to the transport and diffusion ($k_a, k_d \gg v/L, D/L^2$), we have that (Putelat, Recho, and Truskinovsky, 2018)

$$m \approx \frac{k_d}{k_a^0} \frac{c}{g(c)}.$$

Plugging this approximation in (1.2) and assuming that k_d/k_a^0 is a small parameter while $D = D_m k_d/k_a^0$ remains finite, the motor concentration follows the non-linear drift-diffusion equation

$$\partial_t c + \partial_x(cv - D\partial_x(f(c/c_0)c)) = 0, \tag{1.3}$$

where $f(c/c_0) = 1/g(c)$ and the definition of c_0 is given below.

Because the cell membrane is not permeable to motors, zero-flux boundary conditions are associated with (1.3)

$$\partial_x c(l_\pm(t), t) = 0, \tag{1.4}$$

such that the average concentration of motors is a constant set by the initial concentration:

$$c_0 = \frac{1}{L}\int_{l_-}^{l_+} c(x,t)dx. \tag{1.5}$$

Following Kruse et al., 2006, the cell cytoskeleton is assumed to be a one-dimensional layer of active gel. Moreover, the actin meshwork is assumed to be infinitely compressible. Therefore the constitutive law describing the cell active behaviour reads

$$\sigma = \eta\partial_x v + \chi c, \tag{1.6}$$

where $\sigma(x,t)$ is the axial stress within the cytoskeleton, η represents its viscosity and χ the contractility per molecular motor.

In order to understand the influence of the substrate rigidity on cell motility from a purely mechanical standpoint, we need a relation linking the flow of the cell cytoskeleton to the substrate deformation. Using the same approach as Wong and Tang, 2011; Hassan, Biel, and Kim, 2019; Zhang et al., 2020, we model the adhesion with a viscous friction law involving the relative velocity between the cytoskeleton and the substrate:

$$T_x = \xi(v - v_x^s), \tag{1.7}$$

where v_x^s corresponds to the projection of the substrate velocity on the $x-$axis. Additionally assuming a thin film approximation $h \ll L$, since inertia can be neglected, the force balance within the cytoskeleton is given by (Roux et al., 2016), (1.7) becomes

$$h\partial_x\sigma = \xi(v - v_x^s). \tag{1.8}$$

Such relation takes into account the cell's internal activity via the actin retrograde flow, while the influence of the compliance of the substrate is encompassed in the substrate velocity. Taking $v_x^s = 0$ in (1.8), we recover the friction law in the case of a rigid substrate.

For simplification, we will only consider a cell crawling motion at constant length in this work, thus (1.8) is associated with stress boundary conditions at the cell moving edges such that

$$\sigma|_{l_-} = \sigma|_{l_+} = \sigma_b, \tag{1.9}$$

where σ_b is an unknown residual stress representing the constraint fixing the cell length and imposing that the two cell fronts move with the same velocity $V(t) = \dot{l}_- = \dot{l}_+$. This boundary condition typically emerges as a limit when an effective spring that connects the two fronts has a stiffness tending to infinity while $L(t)$ tends to the rest length of the spring. The unknown residual stress σ_b results from this

double limit. See Putelat, Recho, and Truskinovsky, 2018 for more details.

Finally, the protrusion and retraction of the moving fronts are given by the Stefan boundary conditions

$$\dot{l}_{\pm} = v|_{l_-} + v_- = v|_{l_+} + v_+, \tag{1.10}$$

where v_+ and v_- are the given polymerization and depolymerization velocities at the leading edge (l_+) and trailing edge (l_-). See Recho and Truskinovsky, 2013 for details. More realistic albeit more complex models of actin protrusion and retraction of the cell fronts can be found in Ambrosi and Zanzottera, 2016; Giverso and Preziosi, 2018.

In this work, we investigate the effect of bare mechanoreciprocity through three prototypical situations where the effective friction law is considered in its simplest linear form but the substrate is allowed to deform. In chap. 2 we analyze the case of a cell moving on a linear elastic substrate, while in chap. 3 we consider a cell moving on a viscous substrate. Finally, in chap. 4, we study the cell motion in the limit of a vanishing friction coefficient. While in chap. 2, we consider a polymerization/depolymerization driven retrograde flow and assume that the motors concentration is homogeneous, in chap. 3 and chap. 4, $v_{\pm}$ are neglected and the inhomogeneity of the motors concentration is the driving force of the retrograde flow.

Chapter 2

The influence of substrate elasticity on cell polymerization-driven crawling

2.1 Introduction

In the present chapter (submitted for publication to *Int. J. Nonlinear Mech., July 2021*), by extending one of the simplest model of the cytoskeleton actin turnover driven cell crawling (Kruse et al., 2006; Jülicher et al., 2007) to the case of a deformable elastic substrate, we show that taking into account the substrate displacement is sufficient to explain a biphasic relation relating the cell velocity to the substrate stiffness (Stroka and Aranda-Espinoza, 2009; Peyton and Putnam, 2005). Therefore it is not necessary to invoke a non-linear dependence of the traction force on the actin velocity as in Barnhart et al., 2015 who introduced a non-linear actin flow-dependent friction coefficient to ensure a decreased cell-substrate coupling above a critical actin flow velocity or indeed a direct dependence of the active force production machinery on the substrate stiffness (Dokukina and Gracheva, 2010; Sarvestani, 2011) to reach this conclusion.

In order to understand the influence of the substrate rigidity on cell motility from a purely mechanical standpoint, we need a relation linking the flow of the cell cytoskeleton to the substrate deformation. For simplicity we assume a semi-infinite elastic substrate, implying that the thickness of the extra-cellular matrix (ECM) substrate is large compared to the cell size as opposed to the situation studied in (Nicolas and Safran, 2004) where the ECM and adhesion plane form a thin film. The two opposed limits (thick or thin ECM) have been further studied in (Nicolas and Safran, 2006) in the context of the focal adhesion size regulation. In this semi-infinite case, the non-local response of the compliant substrate to a local traction force within the small deformation framework, is given by the Cerruti-Boussinesq solution in the three dimensional case. However if the geometry of the contact is invariant in one direction, a plane strain assumption can apply, leading to a Flamant problem (Johnson, 1987). Both strategies have been employed to characterize the contact between the cell and the substrate. The plane strain assumption has been made by Qian, Wang, and Gao,

2008 in order to simulate the detachment process of a focal adhesion and estimate its lifetime, and by Lelidis and Joanny, 2013 to investigate the effect of substrate rigidity on cell motility with uniformly distributed discrete focal adhesions. The plane strain assumption represents a valid only if the substrate deformation orthogonal to the principal loading direction is negligible. Besides, the substrate displacement found within this framework is not bounded at infinity, thus an arbitrary length needs to be introduced, above which the displacement vanishes. These issues do not arise when considering the three dimensional problem. Traction Force Microscopy (TFM), the method to evaluate the cell traction forces from a measured substrate displacement field, requires the resolution of an inverse problem based on the Boussinesq-Cerruti solution (Dembo et al., 1996; Ambrosi, 2006; Michel et al., 2013; Sabass et al., 2008). In this chapter we propose an approach to obtain a simple relationship between the actin velocity and the substrate displacement under the simplifying hypotheses of a one-dimensional cell crawling on a semi-infinite incompressible elastic substrate. This model corresponds to the situation where the cell is constrained to move on a thin adhesion track.

The chapter is organized as follows. In sec. 2.2, we build the mathematical model corresponding to our geometric assumptions by constructing the kernel governing the response of the semi-infinite elastic substrate to the cell traction force field. We operate under the hypotheses that the friction with the substrate is linear, and that the substrate is a linear elastic medium. Next, in sec. 2.3, we couple this model of the contact with one of the simplest models of actin-based cell motility to obtain a coupled system relating the actin flow field, global cell velocity and substrate displacement. We then study traveling waves (TW) solutions of this problem in sec. 2.4 and give explicit solutions for some special cases of the actin turnover dynamics as well as asymptotic solutions when the substrate is infinitely hard (cell tractions negligible compared to the substrate stiffness) or soft (cell tractions large compared to the substrate stiffness). Then in sec. 2.5, we obtain numerically a biphasic behavior of the steady state velocity as a function of either the substrate rigidity or the cell–substrate friction coefficient. In sec. 2.6, we propose an experimental setup to validate this theory, using T24 bladder cancer cells migrating on substrates of different rigidities (5 kPa, 8 kPa and 28 kPa), confined along thin fibronectin–coated tracks. The actin cytoskeleton flow velocity and the substrate displacement are measured and projected along the cell major axis. Although we were not able to obtain sufficiently motile cells to interrogate our theoretical model in detail, we could estimate the friction coefficient for static cells on substrates of different rigidities. The experimental setup does contain some limitations to address in the future, including the lack of accuracy of the actin acquisition and the need to build thinner cell tracks to improve the applicability of the 1D hypothesis but the values obtained for the friction coefficient are already consistent with the literature describing cell crawling on a rigid substrate.

2.2 Model of the contact between the cell and the substrate

We consider a cell moving on a semi-infinite elastic substrate and restrict our analysis to small deformation of the substrate, neglecting both physical and geometrical non-linearities of the elastic problem. In particular, we shall not differentiate the Eulerian and Lagrangian frames in our approach. Taking advantage of the fact that the track is thin compared to the cell length, we suppose that the traction force in (1.1) only depends on the coordinate along the track. Defining the Boussinesq-Green kernel for a semi-infinite incompressible elastic medium of Young modulus E_s (Landau and Lifshitz, 1959)

$$\mathcal{G}(x,y,z) = \frac{3}{4(x^2+y^2+z^2)^{3/2}\pi E_s}\begin{pmatrix} 2x^2+y^2+z^2 & xy & xz \\ xy & x^2+2y^2+z^2 & yz \\ xz & yz & x^2+y^2+2z^2 \end{pmatrix},$$

we can express the displacement of the substrate $\boldsymbol{u}$ due to cell traction forces

$$\boldsymbol{u}(\boldsymbol{r},t) = \int_{\Omega_C} \mathcal{G}(\boldsymbol{r}-\boldsymbol{r}')\boldsymbol{T}(\boldsymbol{r}',t)\mathrm{d}\boldsymbol{r}', \tag{2.1}$$

From now on, we consider the simple case of a cell confined to move on a one-dimensional straight track of width δ oriented along the $x-$direction (See Fig. 1.10). The cell length $L(t)$ is defined by $L(t) = l_+(t) - l_-(t)$, where $l_\pm(t)$ denotes the cell ends, therefore $\Omega_C(t) = [l_-(t), l_+(t)] \times [-\delta/2, \delta/2]$. The cell geometric center is thus $O(t) = (l_+(t) + l_-(t))/2$.

Plugging (1.1) into (2.1) we obtain the following integral expression of the displacement in the substrate:

$$\boldsymbol{u}(x,y,z,t) = \int_{l_-(t)}^{l_+(t)} \int_{-\delta/2}^{\delta/2} \frac{3}{4((x-x')^2+(y-y')^2+z^2)^{3/2}\pi E_s} \tag{2.2}$$

$$\begin{pmatrix} (x-x')(T_y(x',t)(y-y')) + T_x(x',t)\left(2(x-x')^2+(y-y')^2+z^2\right) \\ (y-y')(T_x(x',t)(x-x')) + T_y(x',t)\left((x-x')^2+2(y-y')^2+z^2\right) \\ (T_x(x',t)(x-x') + T_y(x',t)(y-y'))z \end{pmatrix} \mathrm{d}x'\mathrm{d}y'. \tag{2.3}$$

Averaging the displacement over the y-direction leads to the following simplification

$$\bar{\boldsymbol{u}}(x,z,t) = \int_{l_-(t)}^{l_+(t)} \int_{-\delta/2}^{\delta/2} \int_{-\delta/2}^{\delta/2} \frac{3}{4\delta((x-x')^2+(y-y')^2+z^2)^{3/2}\pi E_s} \tag{2.4}$$

$$\begin{pmatrix} T_x(x',t)\left(2(x-x')^2+(y-y')^2+z^2\right) \\ T_y(x',t)\left((x-x')^2+2(y-y')^2+z^2\right) \\ T_x(x',t)(x-x')z \end{pmatrix} \mathrm{d}x'\mathrm{d}y'\mathrm{d}y. \tag{2.5}$$

Next, by taking the value of the displacement at $z = 0$, we find

$$\boldsymbol{u}^s(x,t) = \int_{l_-(t)}^{l_+(t)} \int_{-\delta/2}^{\delta/2} \int_{-\delta/2}^{\delta/2} \frac{3}{4\delta((x-x')^2+(y-y')^2)^{3/2}\pi E_s} \tag{2.6}$$

$$\begin{pmatrix} T_x(x',t)\left(2(x-x')^2+(y-y')^2\right) \\ T_y(x',t)\left((x-x')^2+2(y-y')^2\right) \\ 0 \end{pmatrix} \mathrm{d}x'\mathrm{d}y'\mathrm{d}y, \tag{2.7}$$

which shows that the surface remains flat during the motion. Projecting $\boldsymbol{u}^s(x,t)$ in the x-direction and performing the integrals in y, we finally obtain

$$u_x^s(x,t) = \int_{l_-(t)}^{l_+(t)} \phi\left(\frac{x'-x}{\delta}\right) T_x(x',t)\mathrm{d}x', \tag{2.8}$$

where

$$\phi(x) = \frac{3\log\left(\frac{1+\sqrt{1+x^2}}{|x|}\right)}{2\pi E_s} = \frac{3\,\mathrm{arcsch}\,(|x|)}{2\pi E_s}. \tag{2.9}$$

and arcsch denotes the inverse hyperbolic cosecant.

In a real experimental context, the substrate is not semi-infinite but has a finite thickness. To justify the use of such approximation we set a homogeneous loading where $T_x(x,t) = T_0$ and $x \in [-L/2, L/2]$ and compare the ensuing averaging displacement at the surface and in the bulk. Thus with

$$\bar{\bar{u}}_x(z) = \frac{3T_0}{4\pi\delta L E_s} \int_{-L/2}^{L/2}\int_{-L/2}^{L/2}\int_{-\delta/2}^{\delta/2}\int_{-\delta/2}^{\delta/2} \frac{\left(2(x-x')^2+(y-y')^2+z^2\right)}{\left((x-x')^2+(y-y')^2+z^2\right)^{3/2}}\mathrm{d}x'\mathrm{d}x\mathrm{d}y'\mathrm{d}y,$$

we wish to find z such that $\bar{\bar{u}}_x(z) \ll \bar{\bar{u}}_x(0)$. Assuming that both $L \gg \delta$ and $|z| \gg \delta$, we find that at leading order,

$$\bar{\bar{u}}_x(0) = \frac{3\delta T_0}{\pi E_s}\tanh\left(\frac{2L}{\delta}\right)$$

and (z being negative)

$$\bar{\bar{u}}_x(z) = -\frac{3L\delta T_0}{4\pi E_s z}.$$

In order to have $\bar{\bar{u}}_x(z)/\bar{\bar{u}}_x(0) \ll 1$, we typically need to impose that $|z| \gg L$.

Note that, in (2.8), when $x \ll 1$, ϕ simplifies to the so-called plane strain kernel $\phi_0(x) = -3\log(|x|/2)/(2\pi E_s)$ (Timoshenko and Goodier, 1970) while it leads to the plane stress kernel $\phi_\infty(x) = 3/(2|x|\pi E_s)$ in the opposite limit where $x \gg 1$ (Johnson, 1987). See Fig. 2.1. Although ϕ_0 is singular at $x = 0$, its integral exists in the Cauchy principal value sense. In contrast, ϕ_∞ is singular and not integrable at $x = 0$, which would lead to an infinite displacement at $x = 0$. However, while ϕ_∞ tends to zero at infinity, ϕ_0 is unbounded at $x = \infty$, which led Timoshenko and Goodier, 1970 to introduce an arbitrary cut-off length x_∞ at which the displacement vanishes ($u_x^s(x_\infty) = 0$) to regularize such situation. Remarkably, the kernel ϕ we obtain from

the Boussinesq-Cerruti solution within the thin track framework, encompasses the advantages of both ϕ_0 and ϕ_∞, namely the integrability at $x = 0$ and the vanishing substrate displacement at $x = \infty$, because ϕ behaves like ϕ_0 near the singularity $x = 0$ and like ϕ_∞ far from the origin.

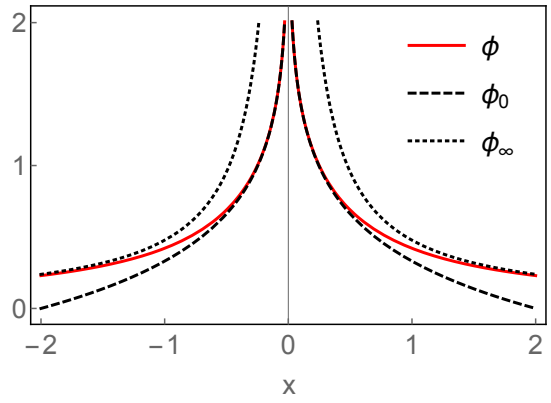

FIGURE 2.1: The non-local interaction kernel ϕ and the kernels ϕ_0 and ϕ_∞ which represent the two limiting behaviors of plane strain and plane stress, respectively. Parameter $E_s = 1$.

In order to eliminate the time-dependence of the integral boundaries, we re-map the problem using the change of variables $\bar{x} = 2(x - O(t))/L(t)$ and $\bar{t} = t$, which leads to the partial derivative relations:

$$\partial_x(.) = \frac{2}{L}\partial_{\bar{x}}(.) \text{ and } \partial_t(.) \overset{\text{def}}{=} \frac{D(.)}{D\bar{t}} = \partial_{\bar{t}}(.) - \frac{2}{L}\left(\dot{O} + \frac{\dot{L}}{2}\bar{x}\right)\partial_{\bar{x}}(.),$$

where the superimposed dot denotes the time derivatives. Introducing the cell aspect ratio $\epsilon(t) = 2\delta/L(t)$ yields

$$u_x^s(\bar{x}, t) = \frac{L(t)}{2}\int_{-1}^{1} \phi\left(\frac{\bar{x}' - \bar{x}}{\epsilon(t)}\right) T_x(\bar{x}', t)\mathrm{d}\bar{x}', \tag{2.10}$$

and injecting (1.7) into (2.10) knowing that $v^s = \partial_t u_x^s(x, t)$ gives

$$u_x^s(x, t) + \frac{\xi L(t)}{2}\int_{-1}^{1} \phi\left(\frac{x' - x}{\epsilon(t)}\right)\frac{Du_x^s(x', t)}{Dt}\mathrm{d}x' = \frac{\xi L(t)}{2}\int_{-1}^{1} \phi\left(\frac{x' - x}{\epsilon(t)}\right) v(x', t)\mathrm{d}x', \tag{2.11}$$

where for simplicity of the notations and from now on, we shall use the same symbol to denote the re-scaled variables, i.e. $\bar{x} := x$ and $\bar{t} := t$.

Assuming the actin retrograde flow velocity v is known, (2.11) is a singular integro-differential equation. In the case of an infinite domain of integration, explicitly solving this type of equation is generally performed by switching to the Fourier domain. In our case where the domain of integration is a finite interval, the functional basis that diagonalizes the symmetric operator ϕ is not explicit as in the case of the plane strain kernel ϕ_0 (Boyd, 2001; Canuto et al., 2012), making the expression of u_x^s as a function of v non-transparent. Note that while the integration of x' is performed over the finite segment $[-1, 1]$, x takes value on the whole real line such that

the boundary conditions associated to the convective time derivative D/Dt are the canonical ones (u_x^s and all its derivatives tend to zero).

2.3 Coupling with a simple model of protrusion based motility

Assuming a uniform distribution of the molecular motors c_0, from (1.6) we can write the simplified cell constitutive behavior as

$$\sigma = \frac{2\eta}{L}\partial_x v + \chi c_0, \tag{2.12}$$

where, $x \in [-1, 1]$ is the rescaled variable introduced above.

Knowing that $v_x^s = Du_x^s(x,t)/Dt$, the spatial rescaled expression of the force balance (1.8) reads

$$\frac{2h}{L}\partial_x \sigma = \xi\left(v - \frac{Du_x^s(x,t)}{Dt}\right). \tag{2.13}$$

Rescaling (1.9) and combining it with (1.6), the boundary condition on stress imposes that

$$\partial_x v|_{-1} = \partial_x v|_1,$$

while the rescaled Stefan boundary conditions from (1.10)

$$\dot{l}_\pm = v|_{\pm 1} + v_\pm. \tag{2.14}$$

We introduce the quantities $\Delta V = v_+ - v_-$ representing the mismatch between polymerization and depolymerization and $V_m = (v_+ + v_-)/2$ representing the average turnover. A first mechanism at the origin of the motility in the model described above is the accretion of actin at the leading edge exactly compensated by the removal of actin at the trailing edge. This leads to a propulsion at velocity V_m which is independent of both the substrate and the cell constitutive behavior. Added to this mechanism, the mismatch between polymerization and depolymerization with a preserved length L of the cell implies a certain flow in the cell, exerting traction forces on the substrate proportional to ΔV. This second contribution depends on the substrate stiffness as well as on the friction coefficient with the substrate in a non-trivial manner that we seek to characterize.

We non-dimensionalize the time by $\eta/(\chi c_0)$, the distance by $L/2$ and the stress by χc_0. Combining (2.11) with (2.12) and (2.13), and denoting $u = u_x^s$ and $\tilde{v} = v - v_0$, where

$$v_0(x) = -\Delta V \frac{\sinh(\alpha^{-1}x)}{2\sinh(\alpha^{-1})} \tag{2.15}$$

is a Dirichlet lift function that accounts for the asymmetry in the protrusion/retraction kinetics at the boundaries, we obtain the non-dimensional problem

$$\begin{cases} \tilde{v}(x,t) = \frac{1}{\alpha}\int_{-1}^{1} G\left(\frac{x-x'}{\alpha},\alpha\right)\frac{Du(x',t)}{Dt}\mathrm{d}x' \\ u(x,t) = \gamma\int_{-1}^{1}\Phi\left(\frac{x-x'}{\epsilon}\right)\partial_{x'x'}[v(x',t)+v_0(x')]\mathrm{d}x'. \end{cases} \tag{2.16}$$

In (2.16), the three non-dimensional parameters

$$\epsilon = \frac{2\delta}{L},\ \alpha = \sqrt{\frac{4\eta h}{\xi L^2}} \text{ and } \gamma = \frac{3h\chi c_0}{\pi L E_s}.$$

respectively represent the track aspect ratio, the ratio of the hydrodynamic length and the cell length and the substrate compliance compared to the cell contractile stress. For simplicity, we keep the same notations for the non-dimensional (de)polymerization velocities $v_\pm$ and their dimensional counterparts. The non-dimensional symmetric kernels representing the non-local behavior of the active viscous cytoskeleton and the elastic substrate respectively read:

$$G(x,\alpha) = \frac{\cosh(\alpha^{-1}+x)}{2\sinh(\alpha^{-1})} - \mathrm{H}(x)\sinh(x) \qquad \text{and} \qquad \Phi(x) = \operatorname{arcsch}(|x|),$$

where H is the Heaviside function. Thus, G corresponds to the resolvent of the elliptic problem (Recho, Putelat, and Truskinovsky, 2015)

$$-\alpha^2\partial_{xx}\tilde{v} + \tilde{v} = \frac{Du}{Dt}$$

with periodic boundary conditions on $\tilde{v}$:

$$\partial_x\tilde{v}|_{-1} = \partial_x\tilde{v}|_1 \text{ and } \tilde{v}|_{-1} = \tilde{v}|_1. \tag{2.17}$$

Importantly, while $\tilde{v}(x,t)$ is only defined for values of $x \in [-1,1]$ (i.e. within the cell), $u(x,t)$ is defined on the whole real line ($-\infty < x < \infty$). Note also that as $\dot{L} = 0$ and u is rescaled by $L/2$, the convective derivative in (2.16) takes the simple form

$$Du/Dt = \partial_t u - V\partial_x u$$

.

After $\tilde{v}$ and u are obtained from (2.16), the dynamics of the moving fronts can be found from (2.14) which leads to

$$V(t) = V_m + \frac{\tilde{v}|_{-1} + \tilde{v}|_1}{2} \tag{2.18}$$

We provide in Table 2.1 some rough estimates of the various rheological coefficients entering the model. One should however bear in mind that these coefficients can vary over several orders of magnitude depending on the biological conditions

name	symbol	typical value
cytoskeleton viscosity	η	100 kPa s (Jülicher et al., 2007; Rubinstein et al., 2009)
contractility	χc_0	1 kPa (Jülicher et al., 2007; Rubinstein et al., 2009)
friction coefficient	ξ	10 Pa s μm^{-1} (Kruse et al., 2006; Barnhart et al., 2011)
lamelipod height	h	1 μm (Kruse et al., 2006)
cell length	L	50 μm
(de)polymerization velocities	$v_\pm$	0.2 μm s^{-1} (Larripa and Mogilner, 2006; Kruse et al., 2006)
substrate stiffness	E_s	10 kPa
track width	δ	5 μm
characteristic length	$L/2$	25 μm
characteristic time	$\eta/(\chi c_0)$	100 s
characteristic velocity	$\chi c_0 L/(2\eta)$	0.25 μm s^{-1}
characteristic stress	χc_0	1 kPa
track slenderness	$\epsilon = 2\delta/L$	0.2
hydrodynamic coefficient	$\alpha = \sqrt{4\eta h/(\xi L^2)}$	0.1
substrate softness	$\gamma = 3h\chi c_0/(\pi L E_s)$	0.02
turnover asymmetry	$\Delta V = 2\eta(v_+ - v_-)/(\chi c_0 L)$	1
turnover average	$V_m = \eta(v_+ + v_-)/(\chi c_0 L)$	1

TABLE 2.1: Rough estimates of the material coefficients, characteristic scales and dimensionless parameters definitions. Some parameters are subjected to several orders of magnitude variations.

and these values should therefore be taken with care. The interest of the type of reduced model that we present rather lie in capturing some physical effects with a minimal baggage than describing cell crawling at a quantitative level.

2.4 Traveling wave solutions

We now seek for traveling wave solutions of (2.16)-(2.18) where V is a constant and $\partial_t u = 0$, implying that $Du/Dt = -V\partial_x u$. In such a case, (2.16) can be combined into the following single integral equation:

$$\alpha^2 f(x) - \gamma V \int_{-1}^{1} \frac{f(x')}{x'-x}\mathrm{d}x' - \int_{-1}^{1} R(x,x')f(x')\mathrm{d}x' = -\frac{\Delta V}{2}x + V - V_m \qquad (2.19)$$

where $f(x) = \partial_{xx}(\tilde{v}(x) + v_0(x)) = (\tilde{v}(x) + v_0(x) + V\partial_x u)/\alpha^2$ represents the substrate traction force and

$$R(x,x') = \gamma V \underbrace{\frac{(x-x')/\epsilon^2}{1+(x-x')^2/\epsilon^2 + \sqrt{1+(x-x')^2/\epsilon^2}}}_{=R_1(x,x')} + \underbrace{H(x-x')(x-x') + \frac{x+1}{2}x'}_{=R_2(x,x')}$$

is a kernel that does not contain any singularity. The R_1 part is reminiscent of the elastic interaction with the substrate (regular part) and the R_2 contribution represents a second order antiderivative with appropriate boundary conditions accounted for by the righthandside of (2.19). The unknown crawling velocity V in (2.19) is fixed by the global force balance constraint:

$$\int_{-1}^{1} f(x)\mathrm{d}x = 0. \qquad (2.20)$$

Solutions for specific choices of the turnover dynamics A simple solution of (2.19) can be found when $v_+ = -v_-$ when the two fronts are symmetrically polarized in opposite directions leading to $V_m = 0$. In this case, we can set $V = 0$ and obtain $f(x) = f_0(x) = -\Delta V \sinh(\alpha^{-1}x)/(2\alpha^2 \sinh(\alpha^{-1}))$. This corresponds to $\tilde{v} = 0$ (i.e. $v(x) = v_0(x)$) and

$$u(x) = \gamma u_0(x) = \gamma \int_{-1}^{1} \Phi\left(\frac{x - x'}{\epsilon}\right) \partial_{x'x'} v_0(x') \mathrm{d}x'.$$

We show in Fig.2.2 the typical trend of such substrate displacement that is induced by a traction force distribution with an even symmetry with respect to the layer center. The substrate displacement reaches its (anti-symmetric) maxima close to the cell

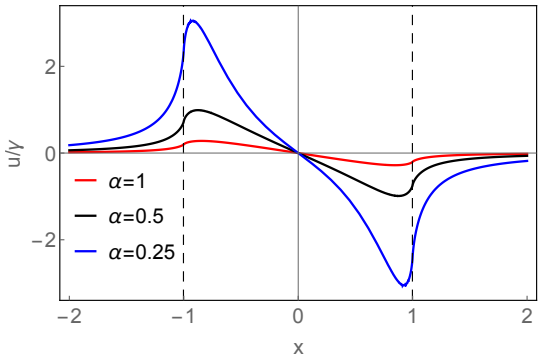

FIGURE 2.2: Displacement u_0 of the substrate induced by the actin velocity field $v = v_0$ corresponding to a static configuration. The dashed lines indicate the normalized cell fronts. Parameters are $\epsilon = 0.2$ and $\Delta V = 1$.

boundaries and sharply decays to zero outside of the cell as no traction forces are imposed in this region. Another simple case is when $v_+ = v_-$, leading to $f = 0$. Thus $\tilde{v} = 0$, $u = 0$ and $V = V_m$. This corresponds to the trivial situation where the actin protrusion and retraction are happening at the same rate at each cell edge, corresponding to a pure treadmilling movement without any internal flow of the filamentous actin. As a result, there are no traction forces and no substrate deformation. This specific situation is rather unrealistic for most cell types as traction forces are known to be applied on the substrate during motion.

More generally, we are interested in the dependence of V on γ for an arbitrary choice of V_m and ΔV. For this, we start by analytically analyzing the asymptotic behavior of V when $\gamma \ll 1$.

Solutions in the limit of underformable substrate When $\gamma = 0$ (i.e. the substrate is undeformable), the solution of (2.19) is again $f(x) = f_0(x)$ corresponding to $\tilde{v} = 0$, $u = 0$ and $V = V_m$. This is the classical case investigated by Jülicher et al., 2007 in the case of an infinitely stiff substrate and generalized by Recho and Truskinovsky, 2013

in the presence of external loading. We can further expand the solution of (2.16)-(2.18) at first order when $\gamma \ll 1$

$$\tilde{v}(x) \simeq \gamma v_1(x) \text{ and } V \simeq V_m + \gamma V_1.$$

Note that the domain of accuracy of such approximation outside of the limit $\gamma \ll 1$ should however be investigated numerically. The validity of such approximation clearly also relies on the fact that V_1 remains finite, such that γV_1 is indeed small compared to V_m.

From (2.16), we obtain,

$$v_1(x) = -\frac{V_m}{\alpha}\int_{-1}^{1} G\left(\frac{x-x'}{\alpha}, \alpha\right) \partial_{x'} u_0(x') \mathrm{d}x'$$

and thus,

$$V_1 = -\frac{V_m}{\alpha}\int_{-1}^{1} G\left(\frac{1-x'}{\alpha}, \alpha\right) \partial_{x'} u_0(x') \mathrm{d}x',$$

which after some standard manipulations takes the form:

$$\frac{V_1}{V_m} = -\frac{\Delta V \operatorname{csch}^2(1/\alpha)}{4\alpha^4}\int_0^2 \operatorname{arcsch}\left(\frac{x}{\epsilon}\right)\left(\alpha \sinh\left(\frac{x}{\alpha}\right) + (x-2)\cosh\left(\frac{x}{\alpha}\right)\right) \mathrm{d}x. \tag{2.21}$$

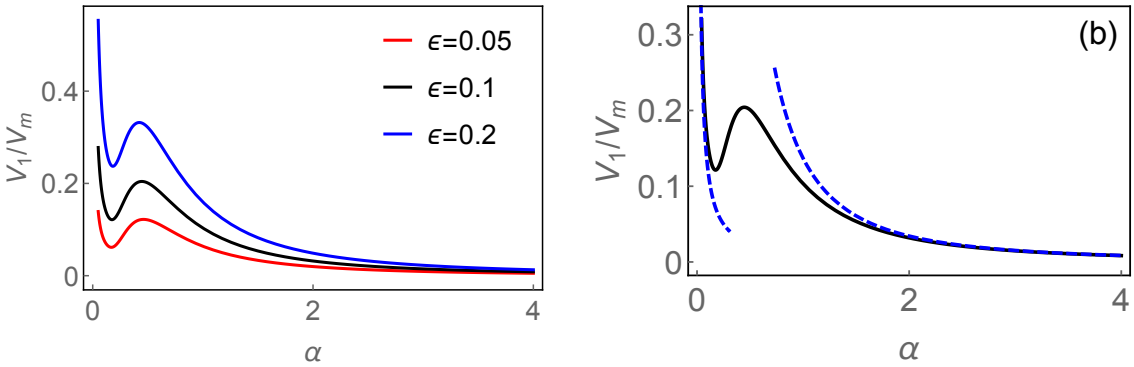

FIGURE 2.3: (a) Normalized value of the increase of velocity due to a small deformability of the substrate as a function of the slippage coefficient of the cell with respect to the substrate. (b) Asymptotic regimes for large and small α as obtained by formulas (2.22). Parameter $\Delta V = 1$.

We illustrate the behavior of V_1 as a function of the parameter α in Fig. 2.3 (a). As V_1 is always positive for a positive value of ΔV, the influence of a small substrate deformability is to increase the cell velocity compared to its value V_m on an undeformable substrate since the flow induced by ΔV in this case promotes motion in the positive direction. A more subtle effect is that the influence of the friction coefficient on the additional speed due to the substrate small deformability is not monotonic. In some parameter ranges, a more adhesive substrate can lead to an increased velocity since traction forces stemming from the actin flow are more effective for the

propulsion. But the opposite effect is also true in other cases since an increase of adhesion can also effectively increase the friction force opposing to the motion. While this effect is lost in the limit of an undeformable substrate, we demonstrate that it can readily be observed for a slightly deformable substrate ($\gamma \ll 1$). We further illustrate this property by analytically computing the dependence of V_1 in (2.21) when α is either small or large to find

$$\frac{V_1}{V_m} \underset{\alpha\to 0}{\sim} \frac{\Delta V \epsilon}{4\alpha\sqrt{\epsilon^2+4}} \text{ and } \frac{V_1}{V_m} \underset{\alpha\to\infty}{\sim} \frac{\Delta V \epsilon \left(2\log\left(\frac{\sqrt{\epsilon^2+4}+2}{\epsilon}\right)+\epsilon-\sqrt{\epsilon^2+4}\right)}{4\alpha^2}. \tag{2.22}$$

These asymptotic expressions, both decreasing with α, are plotted on Fig. 2.3 (b). The cross-over regime between them corresponds to a situation where the velocity increases with α, in a parameter range when the corresponding hydrodynamic length is comparable to the cell length ($\alpha \sim 1$). Note that when V_1 blows up close to $\alpha = 0$, the first order expansion breaks down as the product γV_1 is not necessarily small any more. Thus, this behavior does not correspond to a physically meaningful regime. This type of non-linear dependence between the cell velocity and the substrate adhesiveness was also found in a continuum model representing an actin gel with turnover and linear friction with the substrate by Callan-Jones and Voituriez, 2013. However, the origin of the effect is completely different as the authors consider an infinitely stiff substrate with an internal active stress that depends on the actin density in a non-linear fashion.

Solutions in the limit of highly deformable substrate We now consider the opposite limit where $\gamma \gg 1$ and the substrate is highly deformable. In this case, we seek a solution of (2.19) where $f \ll 1$ while $\tilde{f} = \gamma f$ remains finite. Thus, (2.19) reduces to

$$-V\left(\int_{-1}^{1}\frac{\tilde{f}(x')}{x'-x}\mathrm{d}x' + \int_{-1}^{1} R_1(x,x')\tilde{f}(x')\mathrm{d}x'\right) = -\frac{\Delta V}{2}x + V - V_m \tag{2.23}$$

Observe first that this implies that results will be independent of α in this limit. Indeed, any finite value of the friction coefficient has the same role in the transmission of traction forces because the substrate is already highly deformable. This integral equation with a singular Cauchy kernel is numerically solved following the approach of Karpenko, 1966. The asymptotic value of V is displayed on Fig. 2.4 as a function of the track aspect ratio ϵ. We also show in inset of Fig. 2.4 the spatial dependence of the traction force and the substrate displacement in this limit for several values of ϵ. As expected from the combination of the two limiting relations $\partial_{xx}(\tilde{v}+v_0) \simeq 0$ and $-\alpha^2\partial_{xx}\tilde{v}+\tilde{v} = -V\partial_x u$ (see (2.16)) with associated boundary conditions (2.17), we numerically recover that the substrate displacement on $[-1,1]$ assumes the quadratic form $u(x) = \Delta V/(4V)x^2 + (V_m/V-1)x + \mathrm{Cst}$ where Cst is a constant that remains to be set. For large track aspect ratios (which also correspond

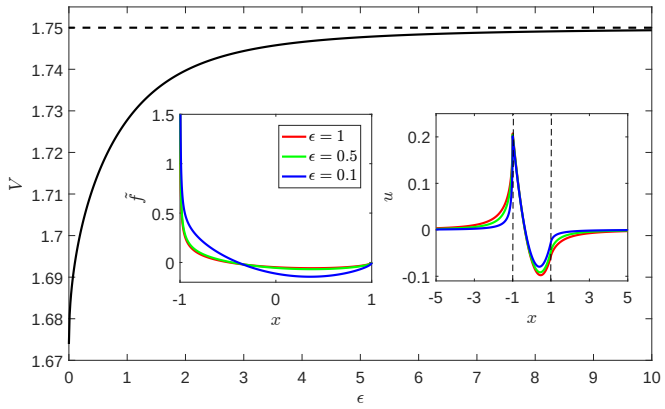

FIGURE 2.4: Crawling velocity in the limit $\gamma \gg 1$ as a function of ϵ. (see (2.23)). The dashed line represents the asymptotic value $V = V_m + \Delta V/4$. In inset, we show the traction forces exerted on the substrate rescaled by γ and the substrate displacement for some values of ϵ. The traction forces display a square root singularity at the trailing edge $x = -1$. Parameters are $\Delta V = 1$ and $V_m = 1.5$.

to a plane strain situation), (2.23) can be further simplified to

$$-V \int_{-1}^{1} \frac{\tilde{f}(x')}{x' - x} \mathrm{d}x' = -\frac{\Delta V}{2} x + V - V_m, \tag{2.24}$$

which solution can be expressed as (see Karpenko, 1966)

$$\tilde{f}(x) = \left(\tilde{f}_0 P_0^{(1/2,-1/2)}(x) + \tilde{f}_1 P_1^{(1/2,-1/2)}(x) \right) \sqrt{\frac{1-x}{1+x}}.$$

In the above expression, $P_{0,1}^{(1/2,-1/2)}$ are the first two Jacobi polynomials (of order zero and order one) with parameters $1/2$ and $-1/2$ and their coefficients are given by

$$\tilde{f}_0 = V - V_m - \Delta V/4 \text{ and } \tilde{f}_1 = -\frac{\Delta V}{2}.$$

Given the integral condition (2.20) $\tilde{f}_0$ has to vanish, leading to the asymptotic velocity when both γ and ϵ are large $V = V_m + \Delta V/4$.

Having clarified the two limits $\gamma \ll 1$ and $\gamma \gg 1$, which are associated to two different values of the crawling velocity and traction forces profiles, we turn to quantifying the dependence of the crawling on the substrate softness γ and the slip coefficient with the substrate α.

2.5 Biphasic relation of the cell velocity

Using again the approach developed in Karpenko, 1966, we compute numerically the solution of (2.19) for the realistic parameters reported in Table 2.1. The unknown velocity in (2.19) is found by dichotomy starting from the value $V = V_m$. We show

on Fig. 2.5 and Fig. 2.6 the resulting dependence of the cell velocity driven by the internal flow as a function of the substrate softness and the slippage coefficient with the substrate. On the left panels of these figures, we also display the typical traction

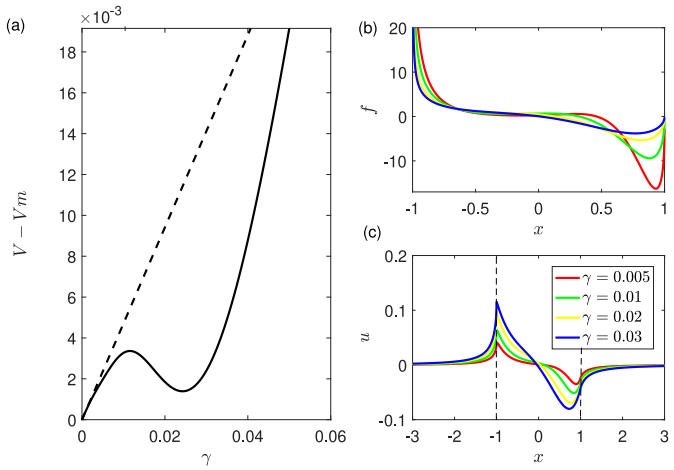

FIGURE 2.5: Dependence of the crawling velocity of the substrate softness. (a) $V - V_m$ as a function of γ displays a biphasic dependence in a realistic range of γ (see Table 2.1). For larger γ, the velocity increases again to reach its asymptotic value given in Fig. 2.4. The dashed line represents the slope of the curve for small γ given by (2.21). Traction forces exerted on the substrate (b) and substrate displacement (c) for several values of γ. Parameters are $\epsilon = 0.2$, $\alpha = 0.1$, $\Delta V = 1$ and $V_m = 1.5$.

force distributions exerted on the substrate and the displacement field at the contact surface as a function of the spatial coordinate. The central symmetry of these distributions is broken, which leads to a non zero flow-driven crawling velocity. The traction forces self-adjust with the substrate displacement and lead to biphasic behaviors of the crawling velocity as a function of both the substrate rigidity and adhesion, as experimentally observed in Palecek et al. (1997) and Peyton and Putnam (2005). The crawling velocity cannot be directly related to the magnitude of the traction force or the mechanical work performed on the substrate as the odd component of f does not contribute to motility. However, we do observe that the $V(\gamma)$ curve is associated with a biphasic behavior of the work of the traction forces $W = \int_{-1}^{1} f(x)u(x)\mathrm{d}x$ while their magnitude $I = \int_{-1}^{1} |f(x)|\mathrm{d}x$ keeps decreasing as γ increases. This is consistent with Fig. 2.5 where we observe that the magnitude of traction forces decreases while the one of the substrate displacement increases when γ varies between 0.01 and 0.02, which corresponds to the biphasic region for V. We quantity this effect on Fig. 2.7, where we show the variation of I and W as a function of γ. A plausible explanation of the present biphasic regime of the velocity in γ is therefore that while the traction forces decrease with the substrate stiffness, their work is maximal at a certain value of γ leading to an optimal propulsion at least at a local level close to this value.

But this explanation does not hold for the global biphasic behavior in α shown in

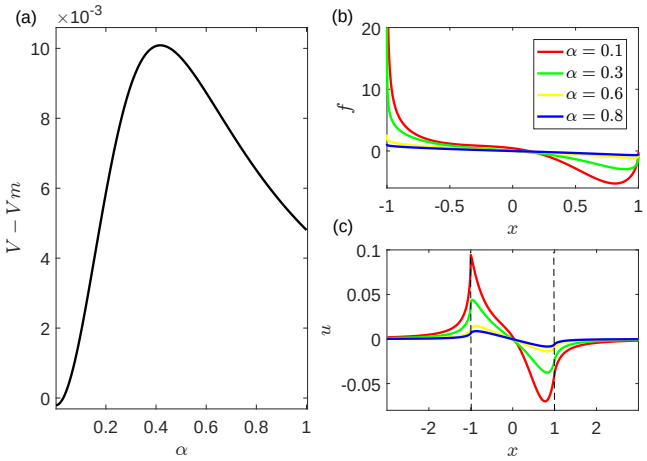

FIGURE 2.6: Dependence of the crawling velocity on the slip coefficient with the substrate. (a) shows the biphasic regime as a function of α. Traction forces (b) and substrate displacements (c) are given for some specific values of α. Parameters are $\epsilon = 0.2$, $\gamma = 0.02$, $\Delta V = 1$ and $V_m = 1.5$.

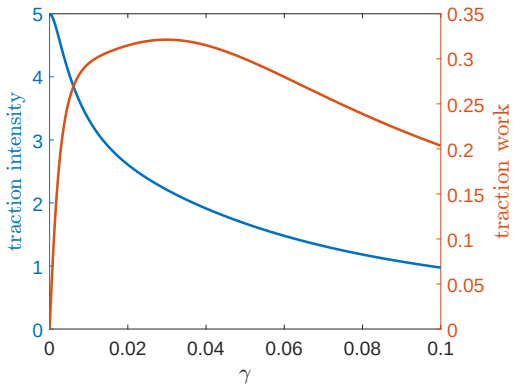

FIGURE 2.7: Evolution of the traction force magnitude $I = \int_{-1}^{1} |f(x)| \mathrm{d}x$ and traction force work $W = \int_{-1}^{1} f(x)u(x)\mathrm{d}x$ as a function of γ at a fixed α. Parameters are $\epsilon = 0.2$, $\alpha = 0.1$, $\Delta V = 1$ and $V_m = 1.5$.

Fig. 2.6 where both the magnitude of the traction forces and their mechanical work on the substrate keep decreasing as α increases. In this case, the importance of the substrate stiffness is to regularize the behavior of the velocity when α is small. Indeed, in the limit where the substrate is very stiff, the velocity expansion blows up when $\alpha \ll 1$ as we show in Fig. 2.3, indicating that the expansion is no longer valid in this regime. A finite γ is sufficient to restore a finite value of the speed when $\alpha \to 0$ (see Fig. 2.6) and regularizes the problem. Physically, $\alpha \ll 1$ corresponds to a large friction coefficient where outside of sharp boundary layers, $v = v^s$ such that the cytoskeleton velocity is transmitted to the substrate. It is therefore expected that the substrate deformability is playing an important role in fixing the velocity in this regime. The other limit where $\alpha \gg 1$ corresponds to a vanishing friction coefficient between the cell and the substrate and the two problems therefore uncouple. We can

thus expect that $V = V_m$ in this regime as the substrate deformation stops contributing to the crawling motion. In between these two regimes, Fig. 2.6 shows that there exists a friction coefficient which maximizes the crawling velocity as traction forces are transmitted to the substrate contributing to the propulsion while the coupling with the substrate is minimally braking the motion.

Contrary to the biphasic regime with respect to the substrate stiffness, the biphasic regime with respect to the substrate friction coefficient is not due to the precise constitutive behavior of the substrate. To demonstrate this, we consider in Appendix A an exponential kernel replacing $\Phi(x)$ by $\Phi_{\exp}(x) \sim \exp(-|x|)$. Such non-singular kernel mimics the non-local feedback of the substrate on the cell motion but is of a shorter range compared to $\Phi(x)$ as it implies that the characteristic lengthscale of the displacement decay in response to a point force is $\sim \epsilon$ while it is ~ 1 for the elastic kernel. In this case, while we recover a generic biphasic regime for the $V(\alpha)$ curve, the $V(\gamma)$ curve is monotonically increasing.

2.6 Experimental platform

We then aimed at constructing an in-house experimental platform to investigate in details the influence of the substrate rigidity on the cell motion and check the range of validity of our simple one-dimensional theoretical model. To do so, it is necessary to produce a substrate with a suitable pattern and appropriate stiffness. To answer this request, patterning methods and cell-compatible hydrogels have been developed that are able to create protein micropatterns on substrates with varied stiffness (Grevesse, Versaevel, and Gabriele, 2014; Grevesse et al., 2013). Hydroxy-PAAm(polyacrylamide) are good candidates and can be functionnalized with fibronectin. After cell seeding on such hydrogels, it is possible to acquire microscopic images of the cells and track fluorescent beads embedded within the substrate in order to study the relationship between cell migration and substrate deformation. Added to this, we used T24 epithelial bladder cancer cells which have been transfected with actin–GFP (Peschetola et al., 2013), so that the actin velocity can be measured. We can therefore image at the same time the substrate beads and the actin meshwork as shown in Fig.2.8 to estimate the substrate displacement and the actin velocity. The necessary steps to follow are detailed in B. In order validate our 1D-model, we project the actin velocity and the substrate displacement on the major axis of the cell, where the origin of the axis corresponds to the cell center (see Fig. 2.9). For a reason that is not yet clear to us, our cells were poorly motile and we therefore restricted our analysis to an acquisition sequence of 15 time frames with a 5 s time lag between them where the cell remains almost static. In this situation, we measured an incremental displacement of the substrate of the order of the measurement uncertainties, corresponding to the resolution of the measurement where $\partial_t u_x^s \ll v$.

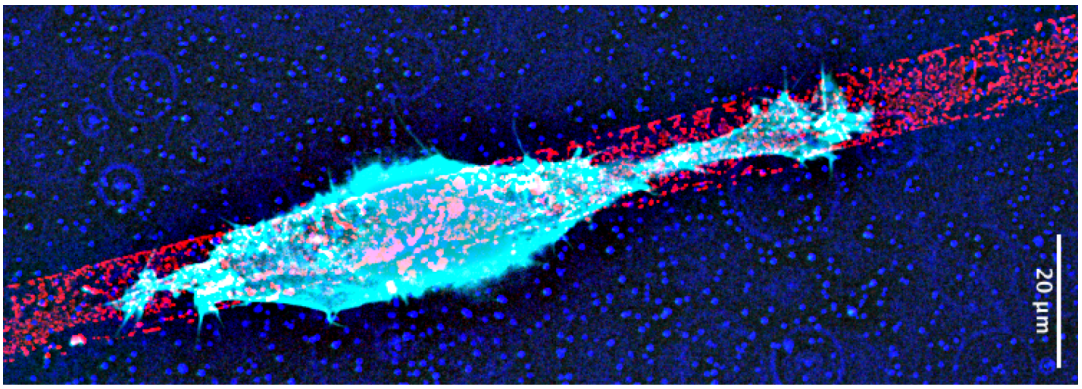

FIGURE 2.8: Fluorescent cell (actin in cyan) migrating on a fibronectin track (red) $w \sim 13\,\mu$m on a gel with embedded beads (dark blue).

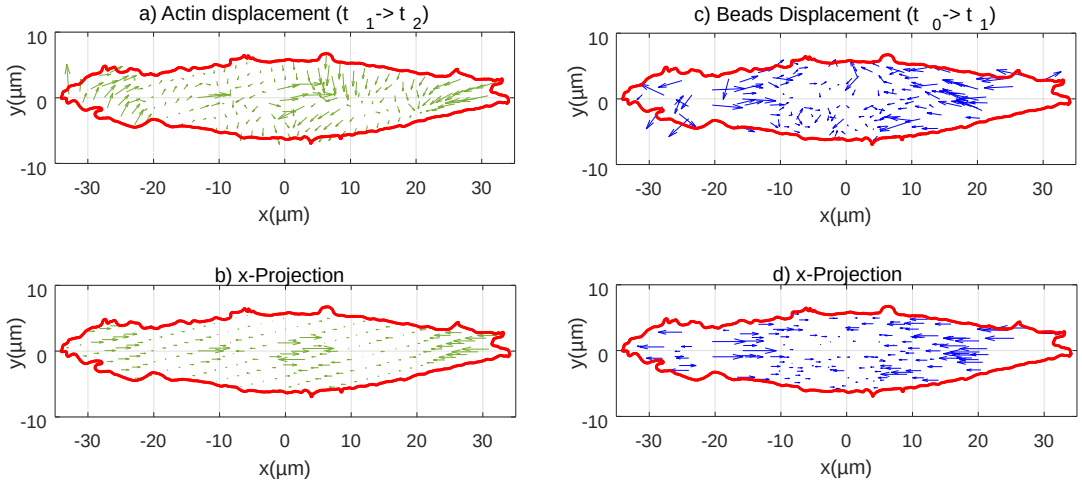

FIGURE 2.9: (a) Actin displacement between two successive acquired time frames (t_2 and t_1 are separated by 5 s) and (b) its projection along the track direction. (c) Beads displacements between a given time frame (t_1) and a reference configuration where the cell is absent (after detachment) (t_0). The projection along the track axis is shown on (d).

Therefore (2.11) becomes a simple integral equation relating u_x^s and v:

$$u_x^s(x) = \frac{\xi L}{2} \int_{-1}^{1} \phi\left(\frac{x' - x}{\epsilon}\right) v(x')\mathrm{d}x', \tag{2.25}$$

Due to the resolution of the measurements, a linear approximation of the actin retrograde flow velocity is appropriate, as pushing the approximation to higher order would essentially capture noise. Thus we write $v(x) \simeq v_1 x$, where the coefficient v_1 can be physically interpreted as the slope of (2.15) at the origin. In order to reduce the effect of fluctuations, a linear regression is performed at every time frame and then averaged over the total number of frames:

$$v(x) = \frac{1}{N} \sum_{n=1}^{N} v_1^n x,$$

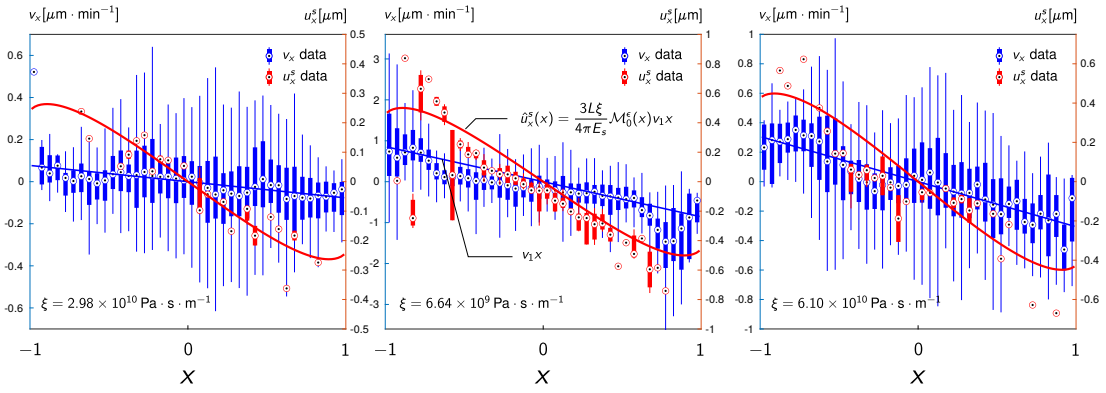

(A) $E_s = 5$ kPa (B) $E_s = 8$ kPa (C) $E_s = 28$ kPa

FIGURE 2.10: Estimation of the friction coefficient ξ from the experimental data for three different substrate rigidities (5 kPa, 8 kPa, 28 kPa). Over one sequence (15 frames with a 5s timestep), the measured actin velocity is represented using 40 blue boxplots and the measured substrate displacement under the cell using 40 red boxplot. Each boxplot is computed considering all the data points in 1/40 of the cell. The blue line represents the linear regression of the measured actin velocity over the sequence. The red line is the predicted substrate displacement obtained using our model (2.26), where the value of ξ is extracted by performing a least square minimization between the predicted (red line) and measured (red boxplots) substrate displacements.

where N is the total number of time frames in a sequence ($N = 15$) and $v_1^n x$ is the linear regression of the actin velocity for frame n. From (2.25), the substrate displacement for $x \in [-1, 1]$ for the linearized expression of v reads,

$$u_x^s(x) = \frac{3L\xi}{4\pi E_s} v_1 x \mathcal{M}_0^\epsilon(x). \tag{2.26}$$

where,

$$\begin{aligned}\mathcal{M}_0^\epsilon(x) =& \epsilon \operatorname{arcsinh}\left(\frac{1-x}{\epsilon}\right) + \epsilon \operatorname{arcsinh}\left(\frac{1+x}{\epsilon}\right) \\ &+ (1-x)\log\left(\frac{\epsilon + \sqrt{(1-x)^2+\epsilon^2}}{1-x}\right) + (1+x)\log\left(\frac{\epsilon + \sqrt{(1+x)^2+\epsilon^2}}{1+x}\right).\end{aligned}$$

The complete method leading to the derivation of the expression of $\mathcal{M}_0^\epsilon$ is developed in detail in the next chapter 3.2.

We then estimate ξ by minimizing the distance between the predicted substrate displacement (2.26) for the measured actin retrograde flow velocity and the substrate displacement from the experimental data. The results for three different substrate rigidities (E_s = 5 kPa, 8 kPa and 28 kPa) are shown in Fig. 2.10. In these plots the actin velocity and substrate displacement experimental data are represented using boxplots. We observe strong fluctuations of the actin velocity for the 5 kPa and 28 kPa rigidities, while the data points are much more concentrated in the 8 kPa case. This is due to the fact, that in the cases of 5 kPa and 28 kPa, the cells where

not elongated enough (not 1D), thus at the same abscissae, we could measure two opposite velocities in some cases. The actin retrograde flow was also difficult to track because of the diffuse fluorescence.

While the friction coefficient seems to exhibit a slight dependency to the substrate rigidity, ranging from 6.64×10^9 Pa.s.m^{-1} to 6.10×10^{10} Pa.s.m^{-1}, more data are needed to extract a clear tendency, as only one cell sequence was retained for each substrate rigidity. Because $\partial_t u_x^s \ll v$, the viscous friction law (1.7) reduces to $T_x(x,t) = \xi v(x,t)$, which corresponds to the friction law on a rigid substrate. This gives us a comparison point to evaluate the relevance of our model. Indeed, while obviously the substrate displacement between soft and rigid substrates cannot be compared (being zero in the latter), the friction law is identical in this specific case. Therefore to validate our model the friction coefficient for a compliant substrate has to be of the same order as the one for a rigid substrate, which we note ξ_r. Extended work has already been done to characterize cell crawling on rigid substrates by mean of a viscous friction law (Jülicher et al., 2007; Rubinstein et al., 2009) and ξ_r has been evaluated to be of the order of $10^9 - 10^{10}$ Pa.s.m^{-1}. With our model we successfully recover a friction coefficient of the same order of magnitude as the one obtained on a rigid substrate.

With this validated experimental setting, we plan to investigate in details situations where the cell is strongly motile in the future.

2.7 Conclusion

Starting from a linear elastic semi-infinite substrate and a viscous friction law linearly relating the cell traction forces and the relative velocity between the actin and the substrate, we modeled the mechanical interaction between a crawling cell and a compliant substrate for cells confined to move on thin micropatterned fibronectin tracks. This model of the cell contact was then coupled with one of the simplest model of cell propulsion based on actin turnover. In such a model, the polymerization at the cell front and its depolymerization at the cell back leads to two motility mechanisms. The addition and removal of actin monomers induces a certain treadmilling velocity that is independent of external conditions but also a retrograde flow of actin from the cell front to its back exists and is dependent on the mechanical coupling with the substrate. Because of such non-local coupling, we find that the dependence of the cell velocity on either the substrate stiffness at a given friction coefficient or the friction coefficient at a given substrate stiffness are not monotonic. This offers an interesting paradigm to complement other theories directly invoking a local non-linear dependence of the friction force on the actin flow to explain this global non-monotonicity. Experimentally, through the simultaneous monitoring of the substrate displacement and the actin retrograde flow velocity for static cells, we were able to extract the effective friction coefficient that enters in our model for different substrate rigidities by performing model-based data-fitting. We observed a

small variation of the friction coefficient with the substrate rigidity, but the values globally lie in the same magnitude range. We find values of the friction coefficient of the same order as the ones previously reported for cells crawling on a rigid substrate suggesting that it is legitimate to consider this parameter as fixed regardless of the substrate rigidity. In the case of the 5 kPa and 28 kPa subtrate rigidities, the cells were not elongated enough to consider them as one dimensional and the actin acquisition resolution was poor. To address these issues it would be necessary to be able to pattern thinner fibronectin tracks.

We expect our experimental method to be of greater interest for cell types and substrate rigidities where the actin retrograde flow and the rate of deformation of the substrate are comparable and the cells are more motile than in the present work. Another perspective is to couple the present model of non-local cell-to-substrate contact to the paradigmatic case of contraction-driven cell motility (Recho, Putelat, and Truskinovsky, 2015) where we expect complex intermittent gaits to appear from the coupling of the Keller-Segel instability to the non-locality induced by the substrate elasticity.

Chapter 3

The influence of substrate viscosity on cell contraction-driven crawling

3.1 Model formulation

In the present chapter, we consider a cell moving on a viscous substrate. As the model formulation has a lot in common with the elastic substrate's one of chap. 2 sec. 2.2, we adapt the elastic model to the viscous case by considering the substrate velocity $\boldsymbol{v}^s$ instead of the substrate displacement $\boldsymbol{u}^s$. The velocity of the incompressible substrate $\boldsymbol{v}^s$ due to the cell traction forces is derived from the Stokeslet solution and, following the methodology of the sec. 2.2, we obtain

$$\begin{aligned} v_x^s(x,t) &= \int_{l_-(t)}^{l_+(t)} \phi\left(\frac{x'-x}{\delta}\right) T_x(x',t)\mathrm{d}x', \\ \text{where now } \phi \text{ reads } \phi(x) &= \frac{1}{4\pi\eta_s}\log\left(\frac{1+\sqrt{1+x^2}}{|x|}\right). \end{aligned} \tag{3.1}$$

Compared to the previous expression (2.8), the shear viscosity of the substrate η_s has replaced $2E_s/3$.

For sake of simplicity, we do not consider the steric hindrance of the molecular motors in this chapter, thus we take $f(c/c_0) = 1$ in the transport equation (1.3)

$$\partial_t c + \partial_x(cv - D\partial_x c) = 0. \tag{3.2}$$

Whereas we considered a polymerization-driven cell crawling in the previous chapter, here the investigated cell motion is contractility-driven, therefore $v_\pm = 0$ in the Stefan boundary condition (1.10):

$$V(t) = \dot{l}_- = \dot{l}_+ = v|_{x=l_-} = v|_{x=l_+}. \tag{3.3}$$

Re-scaling the spatial variable x using the mapping function ψ defined as

$$\begin{aligned} \psi\colon [l_-(t), l_+(t)] &\longrightarrow [-1/2, 1/2] \\ x &\longmapsto \frac{1}{l_+(t)-l_-(t)}\left(x - \frac{l_+(t)+l_-(t)}{2}\right), \end{aligned}$$

and introducing the cell aspect ratio $\epsilon = \delta/L$, the problem reads

$$\begin{cases} v_x^s(x,t) = h\int_{-1/2}^{1/2} \phi\left(\frac{x'-x}{\epsilon}\right)\partial_{x'}\sigma(x',t)dx' \\ \frac{h}{L}\partial_x\sigma = \xi(v - v_x^s) \\ \sigma = \frac{\eta}{L}\partial_x v + \chi c \\ \partial_t c + \frac{1}{L}\partial_x\left[c(v-V) - \frac{D}{L}\partial_x c\right] = 0. \end{cases} \tag{3.4}$$

with the boundary conditions,

$$\sigma|_{-1/2} = \sigma|_{1/2},\ V = v|_{-1/2} = v|_{1/2} \text{ and } \partial_x c|_{\pm 1/2} = 0. \tag{3.5}$$

For sake of clarity we use the same symbol to denote the non-dimensional spatial quantity. The unknowns of problem (3.4)-(3.5) are the velocity fields $v_x^s(x,t)$ and $v(x,t)$, the stress field $\sigma(x,t)$, the motor concentration field $c(x,t)$ and the velocity of the moving fronts $V(t)$.

Note that in this chapter we chose a different spatial rescaling on $[-1/2, 1/2]$ whereas in the previous chapter the rescaled interval was $[-1,1]$, because it is more convenient to work on an interval of length unity. The choice made in the previous chapter was motivated by the fact that we initially wanted to explore Chebyshev expansions to derive some analytical solutions, but this work was not brought to completion.

3.2 The local approximation of the substrate velocity

In order to get around the difficulty of solving a singular integro-differential equation on a segment of finite length without periodic boundary conditions, we propose in the present section, a method based on Taylor expansions to formulate a local approximation of this model.

To deduce a local approximation of our model, we perform a Taylor expansion of the traction forces for x' near x. To this end we first introduce the variable u which is defined by the difference between x' and x and is here assumed to be small. Therefore making the change of variables $u = x' - x$ in (3.1) and performing the previously introduced spatial scaling gives

$$v_x^s(x,t) = L\int_{-1/2-x}^{1/2-x} \phi\left(\frac{u}{\epsilon}\right) T_x(x+u,t)\mathrm{d}u. \tag{3.6}$$

A priori the traction forces function is not continuous on the real line, because the substrate is free of load outside the contact area with the cell Ω_c, thus it exhibits discontinuities at the cell fronts $x = \pm 1/2$ and is therefore not analytic on the real line. However we assume T_x is analytic in the open interval $]-1/2, 1/2[$, ensuring

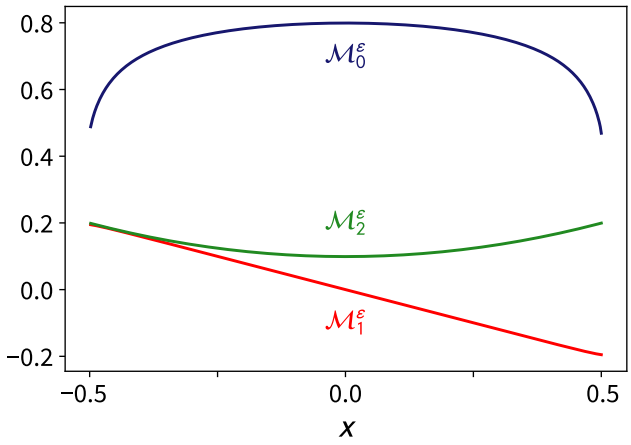

FIGURE 3.1: Representation of the three first $\mathcal{M}_i^\epsilon$ for $\epsilon = 0.1$. Domination of $\mathcal{M}_0^\epsilon$ over the other moments in the loaded region.

the convergence of the Taylor series to T_x. Thus we can write

$$T_x(x+u,t) = \sum_{i=0}^{\infty} \frac{u^i}{i!} \partial_x^i T_x(x,t).$$

Injecting this expression into (3.6) leads to

$$v_x^s(x,t) = \frac{L}{4\pi\eta_s} \sum_{i=0}^{\infty} \frac{\partial_x^i T_x(x,t) \mathcal{M}_i^\epsilon(x)}{i!}, \tag{3.7}$$

where

$$\begin{aligned}
\mathcal{M}_i^\epsilon(x) &= 4\pi\eta_s \int_{-1/2-x}^{1/2-x} u^i \phi\left(\frac{u}{\epsilon}\right) \mathrm{d}u \\
&= \frac{1}{(1+i)^2} \Bigg((1/2-x)^{i+1} \Bigg({}_2F_1\left(\frac{1}{2}, \frac{1+i}{2}, \frac{3+i}{2}, -\frac{(1/2-x)^2}{\epsilon^2}\right) \\
&\quad + (1+i) \log\left(\frac{\epsilon + \sqrt{(1/2-x)^2+\epsilon^2}}{1/2-x}\right)\Bigg) \\
&\quad - (-1/2-x)^{i+1} \Bigg({}_2F_1\left(\frac{1}{2}, \frac{1+i}{2}, \frac{3+i}{2}, -\frac{(1/2+x)^2}{\epsilon^2}\right) \\
&\quad + (1+i) \log\left(\frac{\epsilon + \sqrt{(1/2+x)^2+\epsilon^2}}{1/2+x}\right)\Bigg)\Bigg).
\end{aligned}$$

In the above expression, ${}_2F_1$ denotes the hypergeometric function defined as ${}_2F_1(a,b;c;z) = \sum_{n=0}^{\infty} \frac{(a)_n (b)_n}{(c)_n} \frac{z^n}{n!}$ for $|z| < 1$, where the notation $(q)_n$ stands for $(q)_n = (q+n-1)!/(q-1)!$.

As it appears in Fig 3.1, $\mathcal{M}_0^\epsilon$ dominates the moments of higher orders when ϵ is small, thus the zeroth-order moment dictates the behavior of the substrate velocity in the loaded domain. It is therefore relevant to introduce the approximated substrate

velocity $\hat{v}_x^s$ defined as

$$\hat{v}_x^s(x,t) = \frac{L}{4\pi\eta_s} T_x(x)\mathcal{M}_0^\epsilon(x), \tag{3.8}$$

where

$$\begin{aligned}\mathcal{M}_0^\epsilon(x) =& \epsilon \operatorname{arcsinh}\left(\frac{\frac{1}{2}-x}{\epsilon}\right) + \epsilon \operatorname{arcsinh}\left(\frac{\frac{1}{2}+x}{\epsilon}\right) \\ &+ \left(\frac{1}{2}-x\right)\log\left(\frac{\epsilon+\sqrt{(\frac{1}{2}-x)^2+\epsilon^2}}{\frac{1}{2}-x}\right) + \left(\frac{1}{2}+x\right)\log\left(\frac{\epsilon+\sqrt{(\frac{1}{2}+x)^2+\epsilon^2}}{\frac{1}{2}+x}\right).\end{aligned}$$

From now on, we will refer to this approximation as the zeroth-order approximation, as it is based on the zeroth-order Taylor expansion of the traction force. Our approximation replaces the non-local dependence of v_x^s on the axial traction force by the explicit spatial dependence $\mathcal{M}_0^\epsilon$.

As $T_x = h\partial_x\sigma/L$, we can re-express the zeroth-approximation (3.8) as

$$\hat{v}_x^s(x,t) = \frac{h}{4\pi\eta_s}\partial_x\sigma\mathcal{M}_0^\epsilon(x). \tag{3.9}$$

3.3 Numerical verification of the approximation

We investigate the reliability of the zeroth-order approximation of the substrate velocity previously obtained by computing the remainder between the exact and approximated substrate velocity. In order to perform this analysis the exact solution (3.6) needs to be known.

To do so, let us consider T_x to be a polynomial of degree n for $x \in]-1/2, 1/2[$ such that $T_x(x,t) = \sum_{k=0}^n T_k(t)x^k$. As the cell only exerts traction forces on Ω_c, T_x is extended to zero outside. Plugging the polynomial expression of the traction force into (3.6), we get

$$v_x^s(x,t) = L\sum_{k=0}^n T_k(t)\int_{-1/2-x}^{1/2-x}(x+u)^k\phi\left(\frac{u}{\epsilon}\right)\mathrm{d}u. \tag{3.10}$$

Using the binomial formula in the previous expression and the normalization yields

$$v_x^s(x,t) = \frac{L}{4\pi\eta_s}\sum_{k=0}^n\sum_{i=0}^k T_k(t)\begin{pmatrix}k\\i\end{pmatrix}x^{k-i}\mathcal{M}_i^\epsilon(x). \tag{3.11}$$

One major feature achieved by this formulation is that it is valid on the real line, while the domain of validity of the local formulation (3.7) is restricted to $]-1/2, 1/2[$. However both formulations are equivalent on $]-1/2, 1/2[$.

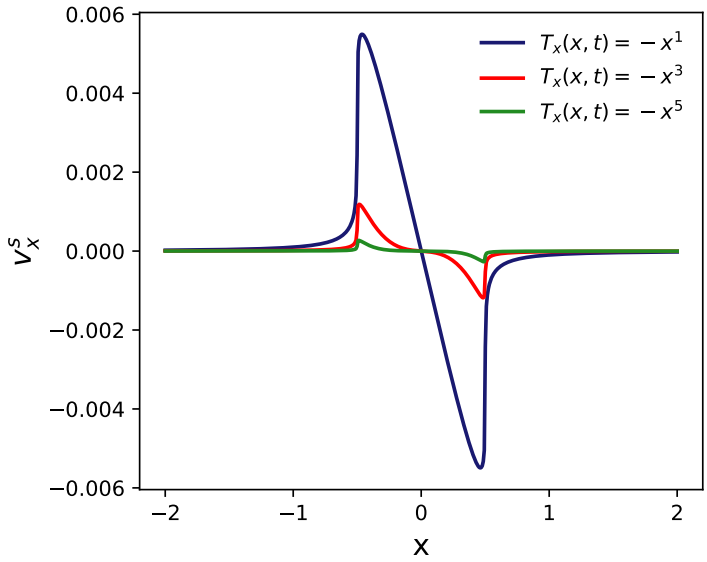

FIGURE 3.2: Exact solution of v_x^s for $\epsilon = 10^{-2}$. The traction force is chosen to be of the polynomial form $T(x,t) = -x$ (blue), $T(x,t) = -x^3$ (red) and $T(x,t) = -x^5$ (green), in order to satisfy the constraint $\int_{-1}^{1} T_x(x,t)\mathrm{d}x = 0$, imposed by the global force balance.

Indeed, if $i > k$ then by convention $\begin{pmatrix} k \\ i \end{pmatrix} = 0$ and (3.11) can be re-written

$$v_x^s(x,t) = \frac{L}{4\pi\eta_s} \sum_{i=0}^{n} \sum_{k=0}^{n} T_k(t) \begin{pmatrix} k \\ i \end{pmatrix} x^{k-i} \mathcal{M}_i^\epsilon(x). \tag{3.12}$$

Because $\partial_x^i T_x(x,t) = \sum_{k=0}^{n} \frac{k!}{(k-i)!} T_k(t) x^{k-i}$, we finally obtain

$$v_x^s(x,t) = \frac{L}{4\pi\eta_s} \sum_{i=0}^{n} \frac{\partial_x^i T_x(x,t) \mathcal{M}_i^\epsilon(x)}{i!}. \tag{3.13}$$

So if T_x is a polynomial the domain of validity of (3.7) can be extended from $]-1/2, 1/2[$ to the whole space.

Now that we found an exact expression of the substrate velocity as a finite sum for any polynomial traction force, a comparison between the exact and zeroth-order expression can be performed.

To this end we choose T_x to be an odd function of the polynomial form, in order to satisfy the constraint imposed by the global force balance $\int_{-1}^{1} T_x(x,t)\mathrm{d}x = 0$,

$$T_x(x,t) = -x^{2n+1}.$$

The exact substrate velocity obtained using (3.11) is shown on Fig. 3.2 for $T_x(x,t) = -x$, $-x^3$ and $-x^5$. The substrate velocity abruptly drops outside the loading region showing that the boundary layers in $\mathcal{M}_0^\epsilon$ are a direct consequence of the free-load boundary conditions.

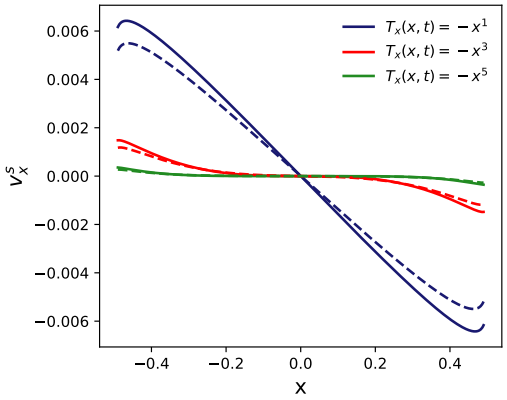

FIGURE 3.3: Comparison between exact (dashed line) and approximated zeroth-order (solid line) solutions of v_x^s with $\epsilon = 10^{-3}$. The traction force is chosen to be of the polynomial form $T(x,t) = -x$ (blue), $T(x,t) = -x^3$ (red) and $T(x,t) = -x^5$ (green), in order to satisfy the constraint $\int_{-1}^{1} T_x(x,t)\mathrm{d}x = 0$, imposed by the force balance.

A graphical comparison between the exact and approximated substrate velocity is represented in Fig. 3.3 for the same parameters as Fig. 3.2 except that $\epsilon = 10^{-3}$. The zeroth-order approximation (3.8) reproduces well the general behavior of v_x^s. However, while the approximation is sufficiently accurate in the bulk (especially as n increases), it overestimates the effect of traction at the vicinity of the cell edges.

In order to estimate the accuracy of our approximation, the exact and approximated substrate velocities are compared by computing the L^2-norm of the remainder, i.e. the relative error between the exact expression and the zeroth-order approximation, defined by

$$R_\epsilon = \frac{\|v_x^s - \hat{v}_x^s\|_2}{\|v_x^s\|_2}.$$

As the framework of our theory is based on a thin track assumption ($\delta \ll L$), we investigate the behavior of this error for decreasing value of the cell aspect ratio ϵ. This error is plotted in Fig. 3.4. At a fixed polynomial degree of T_x the relative error decreases towards zero with decreasing ϵ. This confirms the previously stated domination of $\mathcal{M}_0^\epsilon$ over the moments of higher orders at small values of ϵ and therefore shows the good accuracy of the zeroth-order approximation for ϵ small.

3.4 The space-dependent effective friction coefficient

Using the zeroth order approximation, we can re-write (1.8) such that

$$(h/L)\partial_x \sigma(x,t) = \xi_{\text{eff}}(x,t) v_x(x,t), \tag{3.14}$$

where

$$\xi_{\text{eff}}(x,t) = \xi\left(1 - v_x^s(x,t)/v(x,t)\right). \tag{3.15}$$

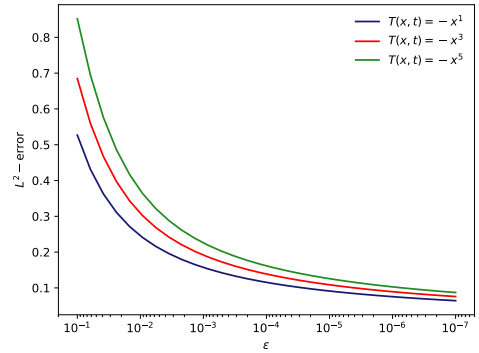

FIGURE 3.4: Relative L2-error convergence analysis.

ξ_{eff} is a space-dependent effective friction coefficient encompassing the substrate deformation.

Injecting (1.8) into (3.9) yields

$$\hat{v}_x^s(x,t) = \frac{L\xi}{4\pi\eta_s}(v(x,t) - v_x^s(x,t))\mathcal{M}_0^\epsilon(x). \tag{3.16}$$

Equating v_x^s and $\hat{v}_x^s(x,t)$, we obtain

$$\hat{v}_x^s(x,t) = \frac{v(x,t)}{1 + \frac{4\pi\eta_s}{L(t)\xi\mathcal{M}_0^\epsilon(x)}}. \tag{3.17}$$

Thus an approximate friction coefficient can be derived by injecting the previous expression in (3.15) and reads

$$\xi f(x), \text{ with } f(x) = \frac{1/(\xi L)}{1/(\xi L) + \mathcal{M}_0^\epsilon(x)/(4\pi\eta_s)}. \tag{3.18}$$

Using the dimensionless parameters

$$\mathcal{Z} = \xi L/\eta,$$

the ratio of elastic and viscous length scales,

$$\mathcal{S} = \eta/\eta_s,$$

the ratio of cell and substrate viscosities, the expression of the effective coefficient is

$$\mathcal{Z} f(x), \text{ with } f(x) = \frac{1/\mathcal{Z}}{1/\mathcal{Z} + \mathcal{S}\mathcal{M}_0^\epsilon(x)/(4\pi)}. \tag{3.19}$$

It has been experimentally shown, that focal adhesions (FAs), connecting the actin cytoskeleton to the substrate, are forming at the front and the rear of a cell, therefore several mathematical models for cell motility introduced an a priori space dependent drag coefficient based on experimental data (Mogilner and Verzi, 2003),

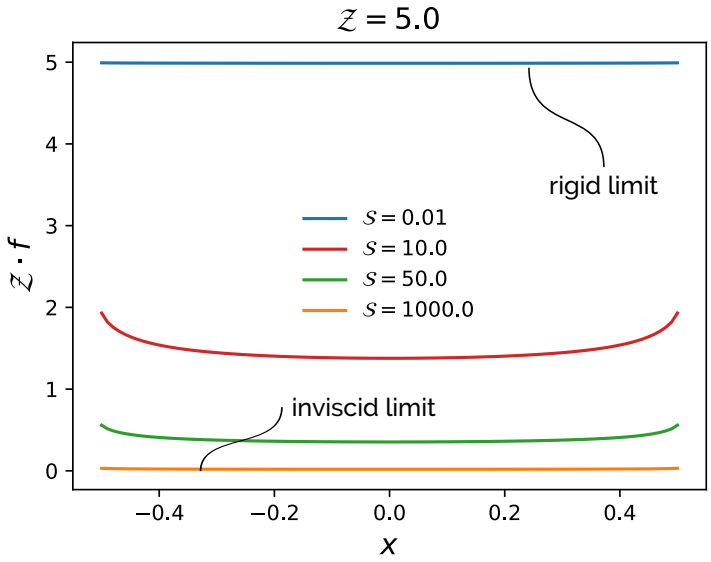

FIGURE 3.5: Spatial evolution of the scaled effective drag coefficient $\mathcal{Z}f$ for different values of scaled substrate viscosity $\mathcal{S}$. In the inviscid limit ($\mathcal{S} \to 0$), there is no coupling between cell and substrate as $\mathcal{Z}f \to 0$.
In the rigid limit ($\mathcal{Z}f \to \infty$), the coupling between cell and substrate is constant over the contact surface as $\mathcal{Z}f \to \mathcal{Z}f$.

which represents the spatial distribution of focal adhesions. In our approach, no previous knowledge of the distribution of focal adhesions is needed, as a space-dependent effective drag coefficient spontaneously arises by formulating the local approximation of problem (3.4).

The shape of this effective drag coefficient illustrated Fig. 3.5 is in qualitative agreement with the experiments as it exhibits higher values at the cell edges.

We recover the same behavior of the effective friction coefficient as Novak et al., 2004, who modeled the interaction between cell and substrate by incorporating the transport equations of integrin in order to simulate the process of adhesion maturation (see Fig 3.6a), and as Lelidis and Joanny, 2013, who used discrete focal adhesions on a viscoelastic substrate (see Fig 3.6b).

In the inviscid limit ($\mathcal{S} \to \infty$), there is no coupling between cell and substrate as $\mathcal{Z}f \to 0$. In the rigid limit ($\mathcal{S} \to 0$), the coupling between cell and substrate is constant over the contact surface as $\mathcal{Z}f \to \mathcal{Z}$.

3.5 Motility initiation by substrate rigidification

The original problem (3.4) involved a singular integro-differential equation. By applying the zeroth-order approximation through the introduction of the previously obtained effective friction coefficient, it is now reduced to the following system of

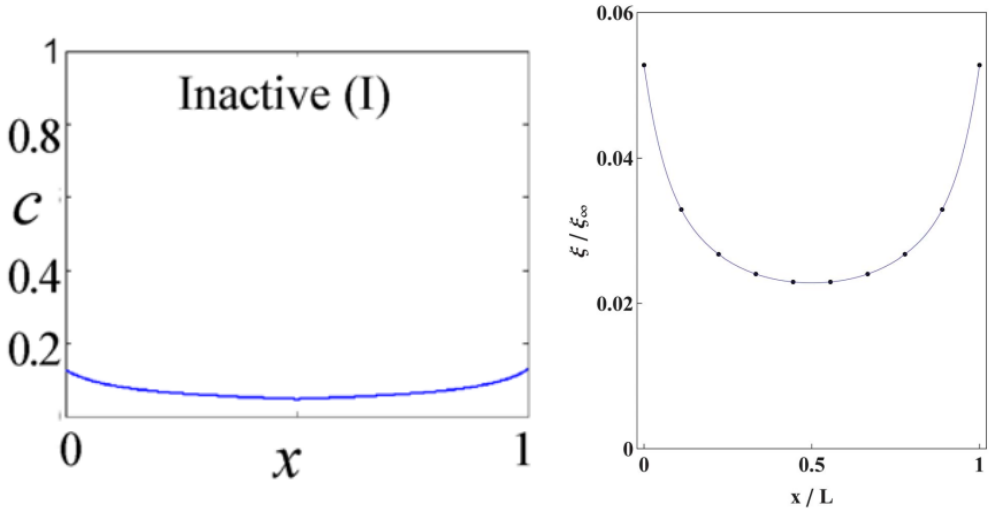

(A) (B)

FIGURE 3.6: (A) Integrin distribution under the cell (Novak et al., 2004) (B) Effective friction coefficient obtained by Lelidis and Joanny, 2013 using a discrete approach of the contact between the cell and a viscoelastic substrate.

PDEs (3.20) with a space-dependent coefficient

$$\begin{cases} \frac{h}{L}\partial_x \sigma = \xi f v \\ \sigma = \frac{\eta}{L}\partial_x v + \chi c \\ \partial_t c + \frac{1}{L}\partial_x \left[c(v - V) - \frac{D}{L}\partial_x c \right] = 0 \end{cases} \tag{3.20}$$

with the boundary conditions

$$\sigma|_{-1/2} = \sigma|_{1/2}, \partial_x \sigma|_{-1/2} = \partial_x \sigma|_{1/2} \text{ and } \partial_x c|_{\pm 1/2} = 0,$$

and the initial condition

$$c(x, 0) = c^0.$$

Re-scaling the length by L, the time by L^2/D, the stress by $\eta D/L^2$, the viscosity of the substrate by η and the concentration by c_0, we obtain the following non-dimensional coupled problem

$$\begin{cases} -\frac{\mathcal{H}}{\mathcal{Z}}\partial_x \left(\frac{\partial_x \sigma}{f} \right) + \sigma = \mathcal{P} c \\ \partial_t c + \partial_x \left[c(\frac{\mathcal{H}}{\mathcal{Z}} \frac{\partial_x \sigma}{f} - V) - \partial_x c \right] = 0, \end{cases} \tag{3.21}$$

with the boundary conditions

$$\sigma|_{-1/2} = \sigma|_{1/2}, \partial_x \sigma|_{-1/2} = \partial_x \sigma|_{1/2} \text{ and } \partial_x c|_{\pm 1/2} = 0,$$

and the initial condition

$$c(x, 0) = 1.$$

Here the dimensionless cell velocity reads

$$V = \frac{\mathcal{H}}{\mathcal{Z}} \frac{\partial_x \sigma|_{\pm 1/2}}{f(\pm 1/2)}.$$

We introduced two supplementary dimensionless parameters:

$$\mathcal{P} = \chi c_0 L^2/(\eta D),$$

the dimensionless measure of motor contractility and

$$\mathcal{H} = h/L,$$

the normalized cell height.

3.6 Numerical implementation

We choose to use a centered finite difference scheme on a regular grid in order to spatially discretize $(3.21)_1$, while the advection-diffusion equation $(3.21)_2$ is discretized using a finite volume approach (see fig. 3.7). $(3.21)_1$ imposes, that the quantities σ and c should be evaluated at the same nodes. The cell is discretized in n elementary volumes, where σ and c are evaluated at the center of each volume and at the interfaces, the velocity and fluxes.

Starting from an initial distribution of motors c_0, we compute the stresses inside the cell and deduce the actin retrograde flow velocity as well as the cell speed. The time is incremented using a Courant-Friedrichs-Lewy condition and the new motors distribution is computed from the stress. The process is iterated until steady-state is reached.

In order, to implement the boundary condition $\partial_x \sigma|_{-1/2} = \partial_x \sigma|_{1/2}$, two ghost nodes for σ were added outside the cell ends.

Using a centered finite difference method, the discretization of $(3.21)_1$ and its associated periodic boundary conditions reads,

$$\begin{cases} \frac{\mathcal{H}}{\mathcal{Z}} \left(-\frac{1}{f_i \Delta x^2} - \frac{f_i'}{2\Delta x f_i^2} \right) \sigma_{i-1}^k + \left(1 + \frac{2\mathcal{H}}{\mathcal{Z} f_i \Delta x^2} \right) \sigma_i^k + \frac{\mathcal{H}}{\mathcal{Z}} \left(-\frac{1}{f_i \Delta x^2} + \frac{f_i'}{2\Delta x f_i^2} \right) \sigma_{i+1}^k = \mathcal{P} c_i^k \\ \sigma_0 = \sigma_n \\ \sigma_1 = \sigma_{n+1} \end{cases}, \tag{3.22}$$

where $(.)_i^k$ represents the discretized value of a dummy quantity at the node i and time k.

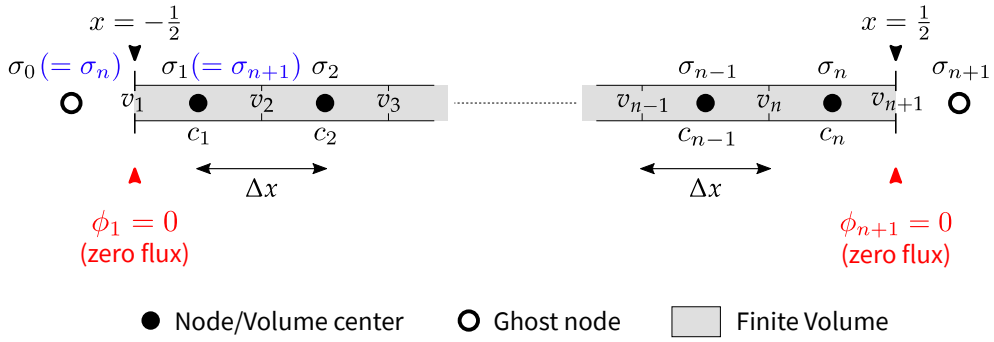

FIGURE 3.7: Representation of the scattered regular grid used for the discretization of (3.21). The cell, ranging from $x = -1/2$ to $x = 1/2$, is discretized in n elementary volumes. The internal stress σ is computed using a finite difference method and c using a finite volume method and are evaluated at the same nodes. The cytoskeleton retrograde flow speed v is deduced from σ also using a centered finite difference method, and thus is evaluated at the volumes interfaces. The discretization of the boundary conditions is achieved using periodic boundary conditions on σ (blue), while the zero flux condition at both cell ends remains a condition on the flux when discretized (red).

In the matrix form (3.22) reads,

$$\begin{bmatrix} 1 & 0 & 0 & 0 & 0 & -1 & 0 \\ 0 & 1 & 0 & 0 & 0 & 0 & -1 \\ \alpha_1 & \beta_1 & \gamma_1 & 0 & 0 & 0 & 0 \\ 0 & \alpha_2 & \beta_2 & \gamma_2 & 0 & 0 & 0 \\ 0 & & \ddots & \ddots & \ddots & 0 & 0 \\ 0 & 0 & 0 & \alpha_{n-1} & \beta_{n-1} & \gamma_{n-1} & 0 \\ 0 & 0 & 0 & 0 & \alpha_n & \beta_n & \gamma_n \end{bmatrix} \begin{bmatrix} \sigma_0^k \\ \sigma_1^k \\ \sigma_2^k \\ \sigma_3^k \\ \vdots \\ \sigma_n^k \\ \sigma_{n+1}^k \end{bmatrix} = \mathcal{P} \begin{bmatrix} 0 \\ 0 \\ c_1^k \\ c_2^k \\ \vdots \\ c_{n-1}^k \\ c_n^k \end{bmatrix} \tag{3.23}$$

where $\alpha_i = \frac{\mathcal{H}}{\mathcal{Z}} \left(-\frac{1}{f_i \Delta x^2} - \frac{f_i'}{2\Delta x f_i^2} \right)$, $\beta_i = 1 + \frac{2\mathcal{H}}{\mathcal{Z} f_i \Delta x^2}$ and $\gamma_i = \frac{\mathcal{H}}{\mathcal{Z}} \left(-\frac{1}{f_i \Delta x^2} + \frac{f_i'}{2\Delta x f_i^2} \right)$.

The periodic boundary conditions on σ are implemented into the two first lines of the right-hand-side (RHS) matrix. Because the cell is migrating at a constant length, the RHS matrix does not depend on time, therefore it needs to be calculated and inversed only once at the start of the simulation.

The actin retrograde flow velocity v at the volume interfaces is deduced from σ,

$$v_i^k = \frac{\mathcal{H}}{\mathcal{Z} \Delta x} \frac{\sigma_{i+1}^k - \sigma_i^k}{f_i}.$$

One important remark has to be made here that f' is not defined at the cell ends, as $f'(x = \pm 1/2) \to \infty$. However, because of our discretization strategy, this value is not needed. Indeed f_i' is calculated at the nodes or elementary volumes centers and not at the interfaces. The cell ends coincide with interfaces where only the velocity is computed, which requires the value of f not f'.

Using the finite volume method, the discretization of the advection-diffusion

equation of the molecular motors $(3.21)_2$ together with the zero-flux boundary conditions at the cell ends and the initial condition on the motors distribution reads (Euler-explicit time discretization)

$$\begin{cases} c_i^{k+1} = c_i^k + \frac{\Delta t}{\Delta x}(\phi_i^k - \phi_{i+1}^k) \\ \phi_1^k = 0 \\ \phi_{n+1}^k = 0 \\ c_i^0 = c^0, \end{cases} \tag{3.24}$$

where ϕ_i^k and ϕ_{i+1}^k denote the sum of the advective and diffusive fluxes at time k and at the left resp. the right interface of the $i-$th elementary volume. The expression of ϕ_i^k is given by,

$$\phi_i^k = \frac{c_i^k + c_{i-1}^k}{2}(v_i^k - V) - \frac{c_i^k - c_{i-1}^k}{2}|v_i^k - V| - \frac{c_i^k - c_{i-1}^k}{\Delta x} \tag{3.25}$$

As we chose an explicit time discretization, the largest admissible timestep Δt ensuring the stability of the scheme is evaluated using the Courant-Friedrichs-Lewy condition and reads

$$\Delta t = \frac{\Delta x}{\max\left(|v_i - V| + \frac{2}{\Delta x}\right)}. \tag{3.26}$$

The steady-state is considered reached when the residual of the motors concentration becomes lower than an arbitrary threshold value.

3.7 Results

When considering the present minimalist problem of a crawling cell evolving on a viscous substrate, the motility is governed by a competition between cell's intrinsic and extrinsic phenomena which are represented through the three main non-dimensional parameters $\mathcal{P}$, $\mathcal{S}$, and $\mathcal{Z}$. $\mathcal{S}$ and $\mathcal{Z}$ characterize the substrate viscosity and the cell adhesion and $\mathcal{P}$ the cell contractility. In order to understand the influence of these parameters on cell motility, a set of numerical simulations was performed on the $(\mathcal{S}, \mathcal{Z}, \mathcal{P})$ domain (see Fig. 3.8). We used the dichotomy method in order to draw the frontier between the static and the motile domain. This method consists in choosing two points in the three-dimensional domain $(\mathcal{S}, \mathcal{Z}, \mathcal{P})$. These two initial points (A, B) are taken sufficiently far away from each others, such that one lies in the static domain (A), while the other lies in the motile domain (B). Next we compute the steady-state cell velocity at both points (V_A, V_B) using the previously introduced algorithm (see sec. 3.6, and obtain $|V_A| \simeq 0$ and $|V_B| \neq 0$. At this point, the segment $[A, B]$ is dichotomized in $[A, C]$ and $[C, B]$ where C is the middle point of $[A, B]$. Then the steady-state velocity at C (V_C) is computed, if $|V_C| \simeq 0$ then A and C both lie in the static domain, else B and C both lie in the motile domain. We retain the segment with two extremities in different domains such that C is on one end, e.g. if A is static and C is motile, we keep the segment $[A, C]$. We iterate

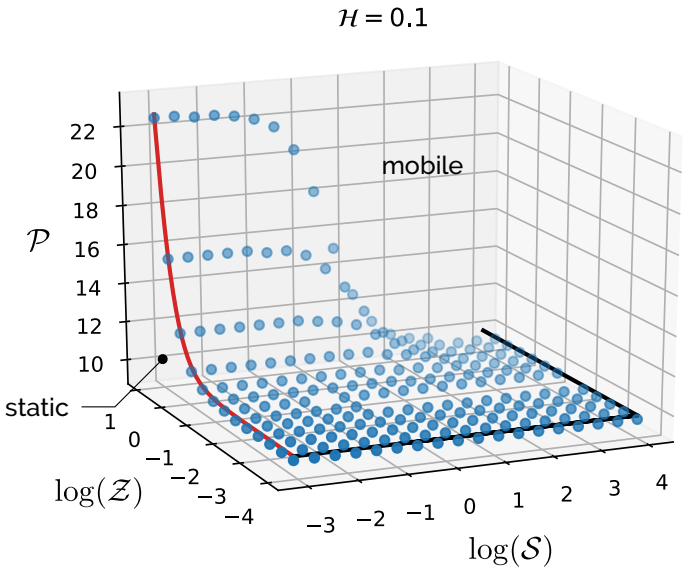

FIGURE 3.8: Three dimensional representation of the bifurcation frontier between the static and motile cell state in the $(\mathcal{S}, \mathcal{Z}, \mathcal{P})$ domain.

the dichotomy process until the length of the segment is arbitrary small. The middle point of this final segment would be on the frontier between the static and motile domain, and is represented by a blue dot in Fig. 3.8.

Fig. 3.8 is a phase diagram delimiting the surface between the motile and static domain, below the surface the cell is static while above it the cell is moving. The plane $\mathcal{P}_0 = \pi^2$ corresponds to the critical contractility in the vanishing friction limit evaluated in the next chapter 4. Below the plane $\mathcal{P} = \mathcal{P}_0$, the cell remains static independently of $(\mathcal{Z}, \mathcal{S})$, in particular, in the frictionless limit $(\mathcal{Z} \to 0)$ and the inviscid limit $(\mathcal{S} \to \infty)$. By definition, $\mathcal{P} = \chi c_0 L^2/(\eta D)$, thus $\mathcal{P} < \mathcal{P}_0$ is equivalent to $\chi c_0 < \mathcal{P}_0 \eta D/L^2$, meaning that the contractility of the motors cannot generate a sufficiently significative advective flow able to counteract the diffusive flow, which tends to uniformize the motors distribution.

Within the framework of our approximation, we introduced an effective friction coefficient $\mathcal{Z}f$, therefore the vanishing friction limit corresponds to $\mathcal{Z}f \to 0 \iff 1/\mathcal{Z} + \mathcal{S}\mathcal{M}_0^e(x)/4\pi \gg 1$.

This limit is reached in particular, for $1/\mathcal{Z} \gg 1$ with finite $\mathcal{S}$ or for $\mathcal{S} \gg 1$ with finite $\mathcal{Z}$. Therefore the inviscid limit is equivalent to the no-friction one, which explains that the same critical contractility is obtained at $\mathcal{Z} \to 0$ and at $\mathcal{S} \to \infty$, represented by the two black lines on Fig. 3.8.

Following Recho, Putelat, and Truskinovsky, 2019, the critical contractility $\mathcal{P}_c$ with respect to the friction $\mathcal{Z}$ for a rigid substrate $(\mathcal{S} \to 0)$, is given by

$$\mathcal{P}_c = \sqrt{\mathcal{Z}/\mathcal{H}}\lambda_c\left(\sqrt{\mathcal{Z}/\mathcal{H}}\right),$$

Where λ_c is obtained by numerically solving the following equation,

$$2\tanh\left(\frac{\sqrt{\mathcal{Z}/\mathcal{H}}}{2}\sqrt{1-\frac{\lambda_c}{\sqrt{\mathcal{Z}/\mathcal{H}}}}\right)=\lambda_c\sqrt{1-\frac{\lambda_c}{\sqrt{\mathcal{Z}/\mathcal{H}}}}.$$

The bifurcation line $\mathcal{P}_c$ corresponding to the rigid substrate limit ($\mathcal{S}\to 0$), is represented by a red line on the bifurcation diagram (see Fig. 3.8). We observe that the simulation is in good agreement with the theory in both, the rigid substrate limit and the no-friction limit investigated in the next chapter, which confirms our numerical simulations.

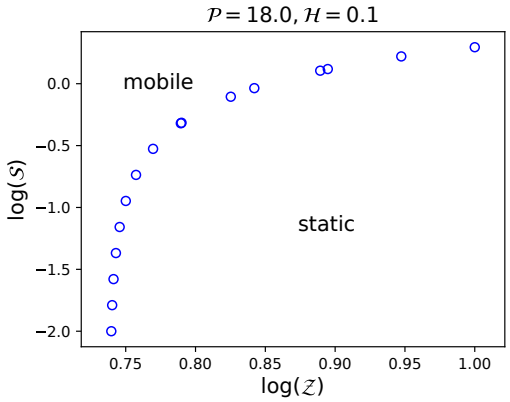

FIGURE 3.9: Two-dimensional representation of the phase diagram in the plane $(\mathcal{Z},\mathcal{S})$ at $\mathcal{P}=18.0$.

At $\mathcal{P}>\mathcal{P}_0$, the motility is governed by the couple of parameters $(\mathcal{Z},\mathcal{S})$, as at $\mathcal{P}$ and $\mathcal{H}$ fixed, (3.21) is completely controlled by $\mathcal{Z}f(\mathcal{Z},\mathcal{S})$. For a better visibility, the bifurcation line at $\mathcal{P}=18.0$ in the plane $(\mathcal{Z},\mathcal{S})$ is represented in Fig. 3.9. The static domain corresponds to values of $(\mathcal{Z},\mathcal{S})$ yielding sufficiently high values of the effective drag coefficient $\mathcal{Z}f(\mathcal{Z},\mathcal{S},\epsilon,x)$, as a decreasing $\mathcal{S}$ and/or an increasing $\mathcal{Z}$ induce an increase in the effective friction coefficient. In the mobile domain, the cell contractility is not only able to overcome the effect of diffusion, but also the resisting effect of the $(\mathcal{Z},\mathcal{S})$-induced effective friction. It is obvious, that the less friction opposes to the cell motion the easier it is able to move. However this also brings a rather counter-intuitive statement, that the cell could better move on an inviscid substrate and or with no friction. This limit is investigated in more details in the next chapter.

In order to gain a better understanding of the influence of both $\mathcal{Z}$, and $\mathcal{S}$ on the cell motility, we study the evolution of the cell speed at steady-state for varying $\mathcal{S}$ and at fixed $\mathcal{Z}$ (see Fig. 3.10a). At $\mathcal{Z}=5.0$, regardless of the value of $\mathcal{S}$ the cell is mobile, while at $\mathcal{Z}=7.0$, the cell passes from static to mobile at a critical value of the substrate viscosity. As shown on Fig. 3.10a, when exclusively evolving in the mobile domain, the cell speed exhibits a monotonous behaviour with respect to $\mathcal{S}$. The profiles reach two plateaus at both the rigid and the inviscid limits. On these

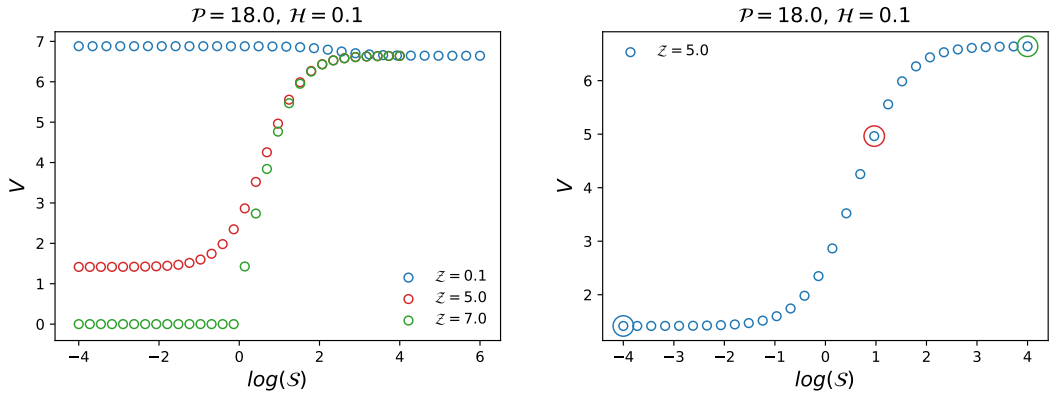

(A) (B)

FIGURE 3.10: (Left) Evolution of the steady-state cell velocity with the substrate viscosity. The cell is moving slower on soft substrates than on rigid ones. At $\mathcal{Z} = 5.0$, the cell remains in the mobile domain. Two plateaus form at both the rigid ($\mathcal{S} \to 0$) and the inviscid ($\mathcal{S} \to \infty$) limits, suggesting a domain of cell sensitivity to the substrate viscosity in between. At $\mathcal{Z} = 7.0$, the cell crosses the frontier between the static and mobile state at a critical value of the substrate viscosity. For $\mathcal{Z} = 0.1$, we observe a shift in the monotony, due to a numerical artefact. (Right) Highlight of the chosen simulation points in the rigid (blue), mechanosensitive (red) and inviscid domain (green).

two plateaus, the cell motility remains unaffected by a variation of the substrate viscosity. This simple mechanical model allows to extract a viscosity range for the cell mechanosensitivity.

For small values of $\mathcal{Z}$, we observe a monotony shift as the cell speed decreases with $\mathcal{S}$ (see Fig. 3.10a). This is most probably the result of a numerical artefact rather than the consequence of an actual physical phenomena. Indeed, we previously mentioned the equivalence between the frictionless limit and the inviscid one. More rigorously, at the inviscid limit we have $\mathcal{Z}f \sim 4\pi/(\mathcal{S}\mathcal{M}_0^\epsilon(x))$, as v remains bounded the force balance combined with the constitutive law gives,

$$\mathcal{H}(\partial_{xx}v + \mathcal{P}\partial_x c) = \frac{4\pi}{\mathcal{S}\mathcal{M}_0^\epsilon} v \to 0. \tag{3.27}$$

After integration it becomes,

$$\partial_x v + \mathcal{P}c = \alpha, \tag{3.28}$$

where α is an integration constant and is evaluated by integrating the previous equation over the length of the cell, therefore

$$\underbrace{\int_{-1/2}^{1/2} \partial_x v}_{=0} + \mathcal{P} \underbrace{\int_{-1/2}^{1/2} c}_{=1} = \mathcal{P} = \alpha.$$

We finally get,

$$\partial_x v = \mathcal{P}(1 - c). \tag{3.29}$$

This is exactly the equation obtained in the next chapter for the frictionless limit, which shows the equivalence between both limits. Therefore the cell speed in the inviscid limit should exactly match the one in the frictionless limit. However, we observe a discrepancy between the cell velocities at both limits, which results in the shift of monotony below a certain $\mathcal{Z}$, corresponding to the entrance in the domain of vanishing friction. The fact that f' blows up at the cell ends causes this numerical artefact, although it is not exactly evaluated at the cell ends, because of our discretization strategy, therefore another numerical method has to be developed in order to address this issue.

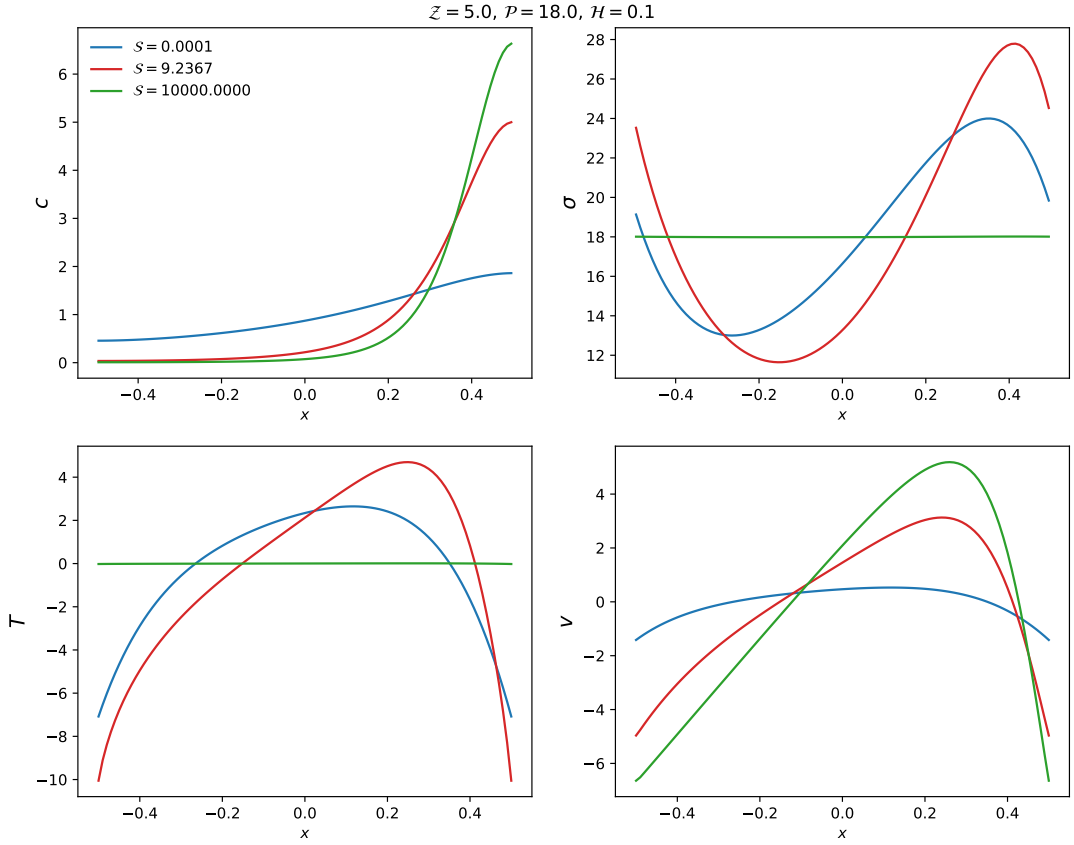

FIGURE 3.11: Representation of the concentration of motors c, the internal stress σ, the cytoskeleton velocity v and the traction force T in the rigid (blue), mechanosensitive (red) and inviscid domain (green). (Top-Left) Representation of the motors distribution inside the cell. The motors concentrate at the back of the cell. As the substrate gets more viscous, the distribution becomes less peaked. (Top-Right) Representation of the stress inside the cell. In the mechanosensitive domain, σ exhibits higher peaks. At the inviscid limit, there is almost no fluctuations of the internal stress, such that $\sigma(x) = \mathcal{P}$. (Bottom-Left) Representation of the traction force exerted by the cell on the substrate. The traction is maximal at the cell ends. At $\mathcal{S} \gg 1$, the traction force vanishes as the cell can not grip. This figure suggests a non-monotonous behaviour of the traction force at the edges with $\mathcal{S}$. (Bottom-Right) Representation of the actin retrograde flow velocity inside the cell. The magnitude of the retrograde flow is greater at small $\mathcal{S}$, as the $\mathcal{S}$-induced friction is lower, thus the cell speed, corresponding to v at the edges follows the same tendency.

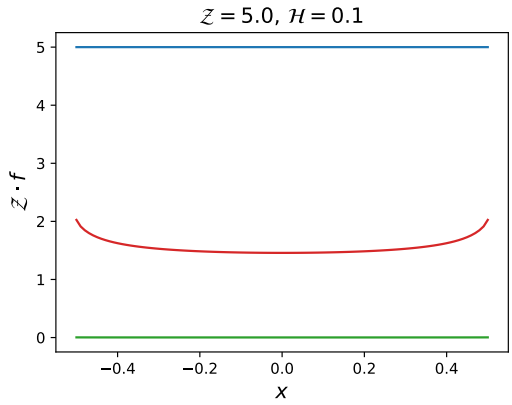

FIGURE 3.12: Representation of the effective friction coefficient in the rigid (blue), mechanosensitive (red) and inviscid domain (green). The inviscid limit is equivalent to the frictionless one.

We plot the local quantities, c, σ, v and the traction force $T = \mathcal{H}\partial_x\sigma$ at the three dots (blue, red, green) in Fig. 3.10a, in order to get a representation of these profiles in the rigid, the mechanosensitive and the inviscid domain, respectively (see Fig. 3.11). Starting from an initial uniform distribution, the motors concentrate at the back of the cell. As a result, when the steady-state is reached, the cell is completely polarized: at the back (x = 1/2), the motors concentrate, inducing a retrograde flow of actin and an overall motion of the cell in the opposite way. The cytoskeleton retrograde flow speed decreases with $\mathcal{S}$ and the distribution of motors is less peaked. The relation between motors concentration and retrograde flow obeys a positive feedback loop, as a local increase of motor density induces a local increase of the retrograde flow velocity, which contributes to the advection of more motors towards this peak. As a decrease of $\mathcal{S}$ induces an increase of the effective drag coefficient $\mathcal{Z}f$ (see Fig. 3.12), the actin retrograde flow slows down with $\mathcal{S}$. The traction forces are maximal at the edges. Because the cell has more grip on a viscous substrate, ultimately the cell pulls more, while on an inviscid one the cell is unable to anchor and therefore the traction force almost vanishes. However, although traction forces are small, the effective friction coefficient is also small in the inviscid limit (see Fig. 3.12). So however small the tractions T may be in that case, there is almost no resistance to motion, which explains this counter-intuitive behaviour of a cell moving faster on an "almost" inviscid substrate. Interestingly, the traction at the edges, which we note $T_\pm$, does not seem to be monotonous with $\mathcal{S}$ as we have $|T_\pm(\mathcal{S} = 10^4)| < |T_\pm(\mathcal{S} = 10^{-4})| < |T_\pm(\mathcal{S} = 9.24)|$.

This tendency is confirmed by plotting the traction force at the edges with respect to $\mathcal{S}$ (see Fig. 3.13), as a biphasic relationship between them is obtained. This is an interesting result, because it means that there is an optimal viscosity at which the transmission of forces from the cell to the substrate is maximal. When considering the motion of a sliding actin filament on an elastic substrate interacting one with another via stochastic bonds, Sens, 2013 obtained a similar behaviour.

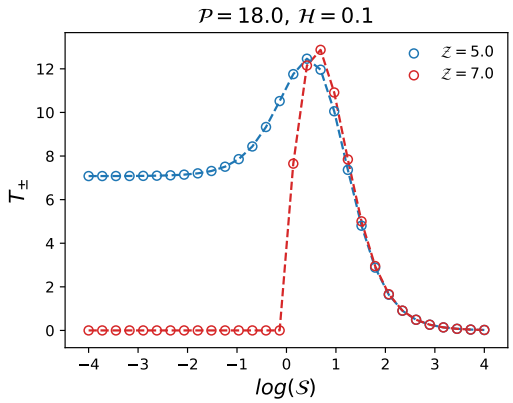

FIGURE 3.13: Evolution of the traction force at the edges of the cell $\mathcal{T}_\pm$ with the substrate viscosity. There is an optimal substrate viscosity at which the traction force reaches a maximum. (The dashed lines are just guides for the eye.)

3.8 Reduced friction coefficient

As previously stated, the governing equations of cell migration (3.21) are completely controlled by $\mathcal{Z}f$, $\mathcal{P}$ and $\mathcal{H}$. In order to explore the effect of the boundary layers in the effective friction coefficient, we approximate $\mathcal{Z}f$ by its mean value $\langle \mathcal{Z}f \rangle = \int_{-1/2}^{1/2} \mathcal{Z}f(x)dx$ in problem (3.21), which becomes

$$\begin{cases} -\frac{\mathcal{H}}{\langle \mathcal{Z}f \rangle}\partial_{xx}\sigma + \sigma = \mathcal{P}c \\ \partial_t c + \partial_x \left[c(\frac{\mathcal{H}}{\langle \mathcal{Z}f \rangle}\partial_x \sigma - V) - \partial_x c \right] = 0. \end{cases} \tag{3.30}$$

Formulating the problem of the cell crawling on a viscous substrate with (3.30), reveals it is actually equivalent to the problem of the cell crawling on a rigid substrate with the space-independent reduced friction coefficient.

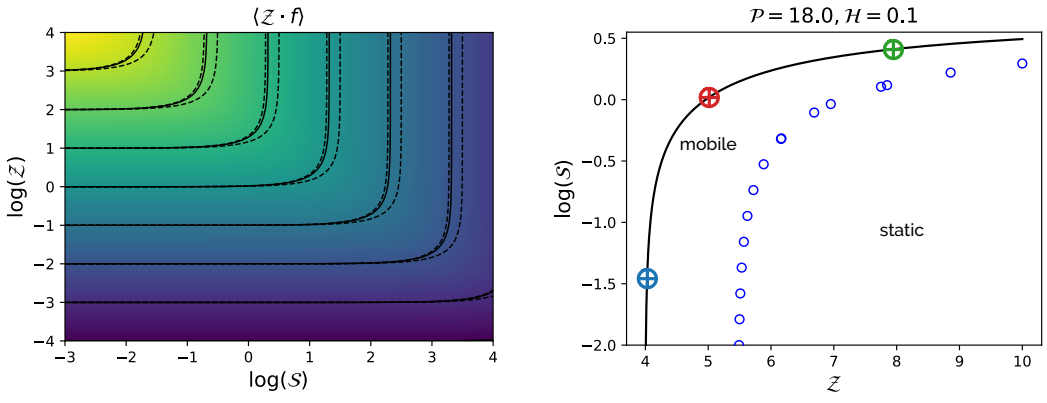

(A) (B)

FIGURE 3.14: (a) Representation of the isolines $\langle \mathcal{Z}f \rangle = \kappa$ (solid lines) in the plane $(\mathcal{S}, \mathcal{Z})$. (b) Isoline $\langle \mathcal{Z}f \rangle = 4$ in the bifurcation plane $(\mathcal{Z}, \mathcal{S})$ at $\mathcal{P} = 18$. This isoline lies in the mobile domain. The targets on this line represent the three chosen simulation points.

Assuming this approximation is accurate, for all $(\mathcal{Z}, \mathcal{S})$ such that $\langle \mathcal{Z} f \rangle = \kappa$, where κ is a constant, we should obtain the same results when solving the system (3.21). The isolines $\langle \mathcal{Z} f \rangle = \kappa$ are represented Fig. 3.14a in the plane $(\mathcal{S}, \mathcal{Z})$. In order to investigate this theory we run three simulations on the isoline $\langle \mathcal{Z} f \rangle = 4$ located in the mobile domain represented by the three dots in Fig. 3.14b.

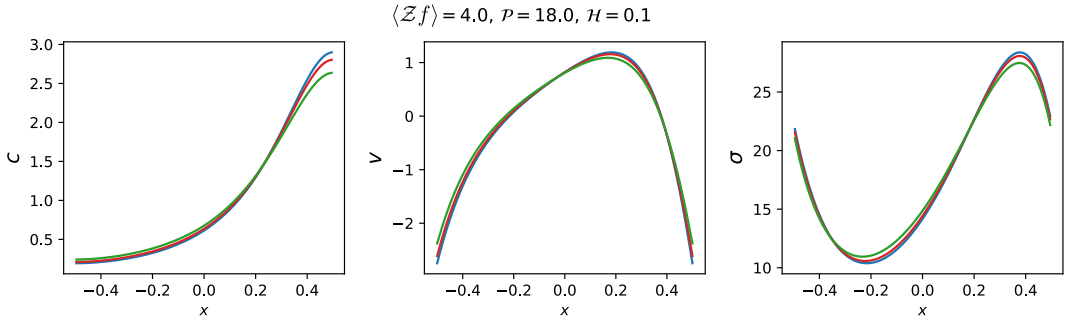

FIGURE 3.15: Representation of the local quantities c, v and σ at the selected points of the isoline $\langle \mathcal{Z} f \rangle = 4$. There is a good match of the quantities on the isoline.

The results of these simulations are compared in Fig. 3.15. Encouragingly, the spatial quantities seem to match with each other quite well. Yet another positive result is represented Fig. 3.16a, where we apposed the profile $V(\mathcal{S})$ obtained in the previous section with the one obtained for $\langle \mathcal{Z} f \rangle(\mathcal{S})$. This result gives an explanation on the shape of $V(\mathcal{S})$ as it exactly follows the shape of $\langle \mathcal{Z} f \rangle(\mathcal{S})$. It also confirms the assumption of the motility properties being characterized by $\langle \mathcal{Z} f \rangle$ for fixed values of $\mathcal{Z}$, $\mathcal{P}$, $\mathcal{H}$ and ϵ. Moreover the bifurcation line previously obtained by the simulation is fitted quite accurately by the isoline $\langle \mathcal{Z} f \rangle = \mathcal{Z}^*(\mathcal{P} = 18)$, where $\mathcal{Z}^*(\mathcal{P} = 18)$ corresponds to the critical value of $\mathcal{Z}$ on a rigid substrate at $\mathcal{P} = 18$ (see Fig. 3.16b). These results enforce the validity of the assumption, thus the three-dimensional bifurcation diagram previously obtained (Fig. 3.8), can be well reconstructed from only the bifurcation line of the rigid limit (see Fig. 3.17).

3.9 Conclusion

Starting from a singular integro-differential formulation of the problem of cell crawling on a viscous substrate, a linearization introduced a space-dependent effective friction coefficient encompassing the non-local response of the substrate to the cell traction forces, thus reducing the problem to a set of PDEs with a non-constant coefficient. This naturally arising space-dependent friction coefficient exhibits boundary layers at the cell edges showing a higher coupling between the cell and the substrate at the boundaries. It increases with the substrate viscosity and with the friction. In comparison with the elastic substrate case, the cell velocity is a decreasing function of the substrate viscosity at a given friction. Indeed, in the inviscid limit while the traction force vanishes, the propulsion is ensured by the molecular motor-driven

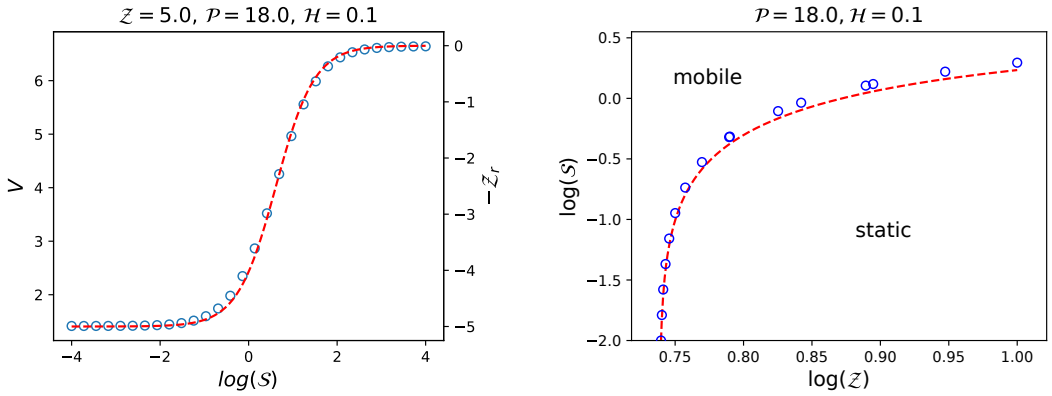

(A) (B)

FIGURE 3.16: (a) Apposition of the profile $V(\mathcal{S})$ (blue circles) with $\langle \mathcal{Z}f \rangle(\mathcal{S})$ (red dashed line). This result explains the behaviour of $V(\mathcal{S})$ as it exactly follows the shape of $\langle \mathcal{Z}f \rangle(\mathcal{S})$. (b) The simulated bifurcation line (blue circles) is accurately fitted by the isoline $\langle \mathcal{Z}f \rangle = \mathcal{Z}^*(\mathcal{P} = 18)$.

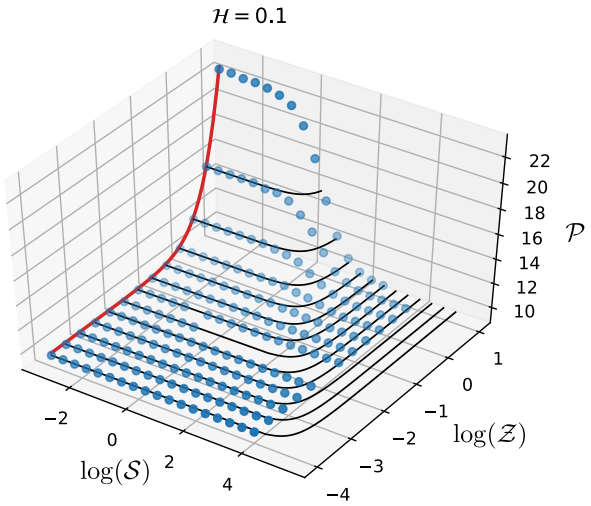

FIGURE 3.17: Reconstruction of the three dimensional phase diagram from the bifurcation line at the rigid limit and the iso-$\langle \mathcal{Z}f \rangle$ lines.

internal flow, which is greater in this limit as the substrate viscosity-induced friction vanishes and therefore explains the higher only contractility dependent velocity. While the cell velocity is monotonic, the magnitude of the traction force is biphasic, which could induce an affinity to an optimal substrate viscosity as has been similarly experimentally observed on a viscoelastic substrate, however further work is needed to confirm this tendency.

We showed that the spatial distribution of the effective friction coefficient was not dictating the cell motility, rather its mean value was. Therefore we were able to further reduce our problem to a set of PDEs with constant coefficient, allowing us to reconstruct any desired quantity at a specific friction and substrate viscosity from the equivalent rigid limit. From this simplified model, the investigation of the cell sensitivity to an external viscosity gradient becomes easier and our approximation

may be of interest for future work in this direction.

Chapter 4

Substrate independent crawling

4.1 Introduction

In three-dimensional biological matrices, cell migration usually does not rely on the formation of focal adhesions (Paluch, Aspalter, and Sixt, 2016) and, using the cell confinement, uses the non-specific friction between the cell and its environement (Bergert et al., 2015) to exert traction forces that break the problem symmetry and lead to motion. Depending on the force production mechanism of the traction forces, several physical models have been put forward to shed light on this instability (Ziebert, Swaminathan, and Aranson, 2012; Tjhung, Marenduzzo, and Cates, 2012; Recho, Putelat, and Truskinovsky, 2013; Callan-Jones and Voituriez, 2013; Camley et al., 2013; Blanch-Mercader and Casademunt, 2013; Giomi and DeSimone, 2014). Still, in such models, a substrate interaction is present in the form of a friction coefficient that can be modulated depending on the affinity of the cell and its environment.

Recently, several two or three dimensional models have been put forward to show that the limit of a vanishing friction coefficient where the traction force of the cell locally vanishes, can still lead to cell motion (Loisy, Eggers, and Liverpool, 2019; Farutin et al., 2019; Le Goff, Liebchen, and Marenduzzo, 2020). In such limit, motility becomes an intrinsic property of the cell that is independent of the environment biophysical details making it an interesting paradigmatic situation from the physical point of view. One can also speculate on the biological role of such mechanism as it would render cell motion robust with respect to a change of the environment chemistry and rheology.

Assuming that cell propulsion in a confined environment such as a track or a channel (Maiuri et al., 2012; Doyle et al., 2013) is mainly driven by its molecular motors (Paluch, Aspalter, and Sixt, 2016), we study one of the most simple one-dimensional model of this substrate independent type of cell motility. We show that, despite its active nature, our model has a variational structure with an effective quasi-potential that is minimized during the cell dynamic and that the minima of

the quasi-potential correspond to the model metastable steady states. These minima represent a static symmetric configuration or a motile asymmetric configuration of the cell and their appearance and relative level are controlled by two non-dimensional parameters driving the motors self-organization: a global contractility coefficient and a parameter representing the steric hindrance between the motors.

Next, by introducing a small stochastic perturbation in the active stress, we show that the metastability of the deterministic system leads to intermittent cell dynamic which can be either dominated by static phases or by motile phases depending on which state is the global or local minimum of the quasi-potential. This result may have importance to physically understand the intermittency of individual cell dynamics (Maiuri et al., 2015; Hennig et al., 2020) but could also be of use to rationalize the fact that in a population of similar cells, a proportion is motile while others are static (Kwon et al., 2019).

4.2 Substrate independent regime

In this chapter, we study the case of vanishing friction between the cell and the substrate. Similarly to the previous chapter, we assume here a contractility-driven cell motion, therefore $v_\pm = 0$ and the moving cell boundaries verify (3.3). The substrate is assumed to be visco-elastic so that certain functional $\mathcal{L}$ relates its velocity with the traction forces exerted by the cell, $v_s = \mathcal{L}[\partial_x \sigma]$. Clearly, if the tractions vanish, the substrate velocity is also zero: $\mathcal{L}[0] = 0$. The vanishing friction limit reads $\xi \to 0$ in (1.8). As the cytoskeleton and substrate velocities remain bounded, we locally have $\partial_x \sigma = 0$, leading to $v_s = 0$. However, the boundary conditions (1.9) imposing the same stress at the two fronts lead to the global constraint,

$$\int_{l_-}^{l_+} (v - v_s) dx = \int_{l_-}^{l_+} v dx = 0.$$

This limit of a small friction coefficient leads to a generic cell crawling dynamic that is independent of the cell/substrate mechanical behavior.

Combining the constitutive relation (1.6) with the no-flux boundary conditions (3.3), we obtain that the homogeneous stress in the cytoskeleton is $\sigma = \chi c_0$. As a result, $\chi(c_0 - c) = \eta \partial_x v$ which leads by integration to,

$$v(x,t) - V(t) = \int_{l_-}^{l_+} \mathrm{H}(x - z)(c_0 - c(z,t)) dz,$$

where H denotes the Heaviside step function.

Defining the non-dimensional traveling coordinate $y = [x - (l_- + l_+)/2]/L$ and rescaling the concentration by c_0, the space by L and the time by L^2/D, we obtain

the following non-dimensional coupled problem:

$$\begin{cases} \mathcal{P}(1-c) = \partial_y w \\ \partial_t c + \partial_y(cw - \partial_y(f(c)c)) = 0, \end{cases} \tag{4.1}$$

with no-flux boundary conditions on c, $\partial_y c(\pm 1/2, t) = 0$ and w, $w(\pm 1/2, t) = 0$. In (4.1), there is only one single non-dimensional (active) parameter that sets the system dynamic $\mathcal{P} = \chi c_0 L^2/(\eta D)$. As $w = v - V$ represents the flow of cytoskeleton in the cell frame of reference, the cell velocity is given by the condition,

$$V(t) = -\int_{-1/2}^{1/2} w(y,t)dy. \tag{4.2}$$

Note that (4.1) can be written as a single non-linear and non-local drift-diffusion equation by solving for w in $(4.1)_1$,

$$w(y,t) = \mathcal{P}\int_{-1/2}^{1/2} \mathrm{H}(y-z)(1-c(z,t))dz \tag{4.3}$$

such that $(4.1)_2$, becomes

$$\partial_t c + \partial_y\left(c\mathcal{P}\int_{-1/2}^{1/2} \mathrm{H}(y-z)(1-c(z,t))dz\right) = \partial_{yy}(f(c)c). \tag{4.4}$$

In this non-dimensional formulation of the problem, the total mass conservation constraint (1.5) becomes

$$\int_{-1/2}^{1/2} c(y,t)dy = 1. \tag{4.5}$$

Note that combining (4.2) and (4.3) and using condition (4.5), we obtain the following formula directly relating the velocity and the first moment of the distribution of motors

$$V(t) = -\mathcal{P}\int_{-1/2}^{1/2} zc(z,t)dz \tag{4.6}$$

showing that the cell motion is supported by the global asymmetry of c.

When $\mathcal{P} = 0$, (4.4) represents a purely passive system where the motors only diffuse and the solution of (4.4) is a homogeneous motor distribution $c \equiv 1$ associated with $V = 0$ (and $w \equiv 0$). However, when $\mathcal{P}$ becomes larger than the critical value $\mathcal{P}_c = \pi^2(f(1) + f'(1))$, where $'$ denotes the derivative, multiple steady states become possible (See Appendix. C.1) and the question of their local and global stability properties arises. We shall address this question in the following section by exhibiting a Lyapunov functional that is minimized during the dynamics of (4.1).

4.3 Variational structure

We define the Lyapunov functional Frank, 2005; Chavanis, 2015, $\mathcal{F} = \mathcal{E} - \mathcal{P}\mathcal{S}$ where the "energetic" and "entropic" terms are

$$\mathcal{E}[w] = -\frac{1}{2}\int_{-1/2}^{1/2} w^2 dy \text{ and } \mathcal{S}[c] = -\int_{-1/2}^{1/2} s(c)dy.$$

In the above formula the entropy per unit volume $s(c)$ is defined in the following way:

$$s''(c) = f'(c) + \frac{f(c)}{c},$$

where we impose that $s(0) = 0$ and $s(\infty) = \infty$. As f is a positive and increasing function, these conditions imply the existence of a minimum $s_{\min} \leq 0$ such that $s \geq s_{\min}$. When $f(c) = 1$, we recover the Boltzmannian entropy $s(c) = c\log(c) - c$ while for our choice

$$f(c) = 1 + rc^2, \tag{4.7}$$

where r is a non-dimensional parameter controlling the strength of the steric hindrance, we obtain,

$$s(c) = rc^3/2 + c\log(c) - c.$$

For the homogeneous solution, only the entropic term contributes to $\mathcal{F} = \mathcal{F}_0 = \mathcal{P}(r/2 - 1)$.

Using (4.1), the inequality

$$\partial_t \mathcal{F} = -\mathcal{P}\int_{-1/2}^{1/2} \frac{(cw - \partial_y(f(c)c))^2}{c} dy \leq 0,$$

shows that $\mathcal{F}$ necessarily decays during the dynamics and that $\partial_t \mathcal{F} = 0$ implies that $\partial_t c = 0$. As using (4.3) we can check that $|w| \leq \mathcal{P}$, we also obtain that $\mathcal{F} \geq -(\mathcal{P}^2/2 - \mathcal{P}s_{\min})$ is bounded from below insuring via Lyapunov theory Frank, 2005 that system (4.1) converges to an equilibrium state.

The effective energy can be expressed as a functional of c only by using (4.3),

$$\mathcal{E}[c] = \frac{\mathcal{P}^2}{2}\int_{-1/2}^{1/2}\int_{-1/2}^{1/2} \max(y,z)(1 - c(y,t))(1 - c(z,t))dydz$$

such that $\mathcal{F}$ is also a functional of c only. Using this expression, we compute the gradient of $\mathcal{F}$ with respect to c

$$\frac{\delta \mathcal{F}}{\delta c}(y,t) = -\mathcal{P}^2\int_{-1/2}^{1/2} \max(y,z)(1 - c(z,t))dz + \mathcal{P}s'(c(y,t)).$$

Thus (4.4) is equivalent to

$$\partial_t c = \partial_y\left(\frac{c}{\mathcal{P}}\partial_y\left(\frac{\delta \mathcal{F}[c]}{\delta c}\right)\right),$$

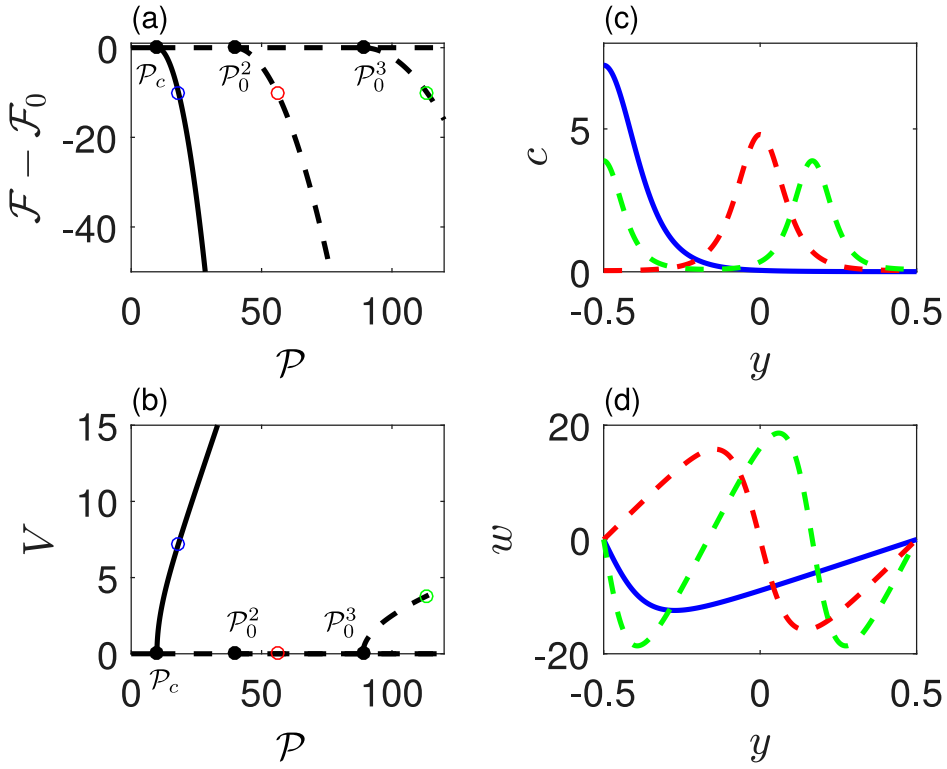

FIGURE 4.1: Three first bifurcations from the homegeneous state for $r = 0$. (a) and (b) are bifurcation diagrams for the quasi-potential and the cell velocity. They have a pitchfork supercritical structure. Black dots localize the bifurcation points. (c) and (d) show the profiles of c and w for some special points labeled with the corresponding colored circles on (a) and (b). Full lines correspond to locally stable branches or solutions while dashed lines are locally unstable

showing that the dynamics of c is driven by its relaxation to the minimum of the quasi-potential $\mathcal{F}$. The globally stable steady state is therefore the $c_{\text{eq}}(y)$ distribution that minimizes $\mathcal{F}$ under the constraints $\partial_y c_{\text{eq}}(\pm 1/2) = 0$ and $\int_{-1/2}^{1/2} c_{\text{eq}}(y)dy = 1$. The local minima of $\mathcal{F}$ are locally stable steady states while maxima and saddle points are unstable steady states Frank, 2005; Chavanis, 2015.

4.4 Metastable steady-states

We begin by characterizing the critical points of $\mathcal{F}$ which correspond to the possible steady states of system (4.1). To do so, we implement a continuation method starting from the homogeneous solution at $\mathcal{P} = 0$ using the software AUTO (Doedel, Keller, and Kernevez, 1991) and follow into the non-linear regime the bifurcations branching from this state as $\mathcal{P}$ increases. The critical values at which these non-trivial solution emerge are given by $\mathcal{P} = \mathcal{P}_0^k = (1 + 3r)k^2\pi^2$, where $k \geq 1$ is an integer (see Appendix. C.1). The first of these values is $\mathcal{P}_c = \mathcal{P}_0^1$. We show the first three branches obtained this way on Fig. 4.1. As solution measures, we show the values of $\mathcal{F} - \mathcal{F}_0$ and V. For each solution bifurcating at an odd bifurcation point

(i.e. k is odd), there is a symmetric solution with respect to the center of the segment associated with the opposite velocity (see Recho, Putelat, and Truskinovsky, 2015). The value of the quasi-potential for these two symmetric solutions is the same. We only show the solution leading to a positive velocity on Fig. 4.1. Each solution bifurcating at an even bifurcation point (i.e. k is even) has an even symmetry with respect to zero and is thus associated with a zero velocity (see (4.6)). As we show on Fig. 4.1, when the bifurcation order increases, the number of patterns in the motor concentration increases. We check in Appendix. C.2 that, except the first bifurcation, all the bifurcating solutions are locally unstable. Added to this, the homogeneous solution cease to be locally stable past the first bifurcation point.

However, the stability status of the first bifurcation branch is interesting. We can analytically show using a normal form expansion (See Appendix. C.1) that the bifurcation is pitchfork supercritical if $r < r_c = (7 + \sqrt{57})/12$ or subcritical if $r > r_c$. In the supercritical case, a local stability of the bifurcating branch is found, leading to a simple situation where the cell converges to either a motile or static (homogeneous) state depending whether $\mathcal{P} \geq \mathcal{P}_c$ or $\mathcal{P} \leq \mathcal{P}_c$. The subcritical case is more complex. As we illustrate on Fig. 4.2, there is a turning point located at $\mathcal{P} = \mathcal{P}_t \leq \mathcal{P}_c$ along the bifurcating branch leading to a fold. We can then again numerically check that solutions before the fold are numerically unstable while solutions after the fold are linearly stable again, although they look qualitatively similar with motors self organizing at the trailing edge of the cell, see Fig. 4.2. Thus, there is a choice of parameters ($r > r_c$ and $\mathcal{P} \in [\mathcal{P}_t, \mathcal{P}_c]$) for which the static and motile configurations can be both locally stable, the globally stable solution being the one corresponding to the minimum of the quasi-potential. We show on Fig. 4.3 the resulting phase diagram where the motile and static phase are shown as well as the third metastable phase where the two configurations can coexist. In this phase, a "Maxwell line" separates the region of parameters space where the motile state is the global minimum of $\mathcal{F}$ and those where it is the static (homogeneous) state.

This property entails interesting consequences when the contractility is no longer deterministic but is subjected to small stochastic fluctuations as the cell can switch between the two configurations leading to stop-and-go dynamics.

4.5 Stochastic contractility

To simply illustrate the effect of metastability on the cell dynamic, we consider a source of noise in the model by changing (1.6) into

$$\sigma = \eta \partial_x v + \chi c + \sigma_s,$$

where $\sigma_s(x,t)$ is a small ($|\sigma_s| \ll \chi c_0$) stochastic spatio-temporal noise. As an example of Σ_s, we take

$$\partial_t \Sigma_s - \Theta \partial_{xx} \Sigma_s = \dot{W}$$

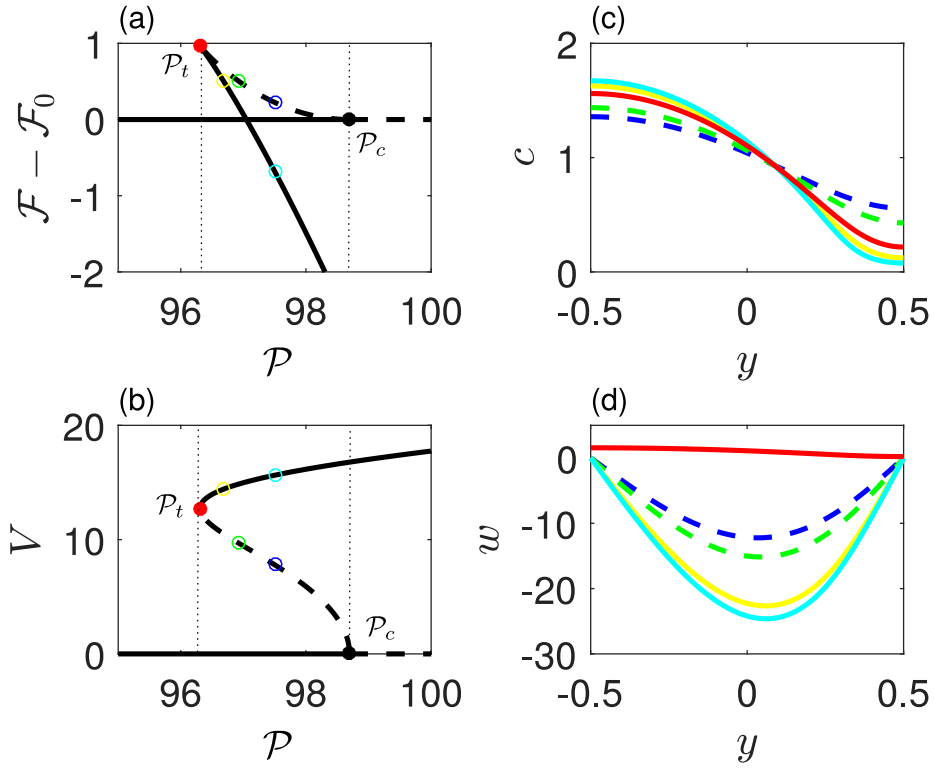

FIGURE 4.2: Structure of the first bifurcation from the homogeneous state for $r = 3$. (a) and (b) are bifurcation diagrams for the quasi-potential and the cell velocity showing the subcritical nature of the bifurcation. The black dot localizes the first bifurcation point and the red dot the turning point. The thin dotted vertical lines represent the domain where both the static and motile configurations are locally stable. (c) and (d) show the profiles of c and w for some special points labeled with the corresponding colored circles on (a) and (b). Full lines correspond to locally stable branches or solutions while dashed lines are locally unstable.

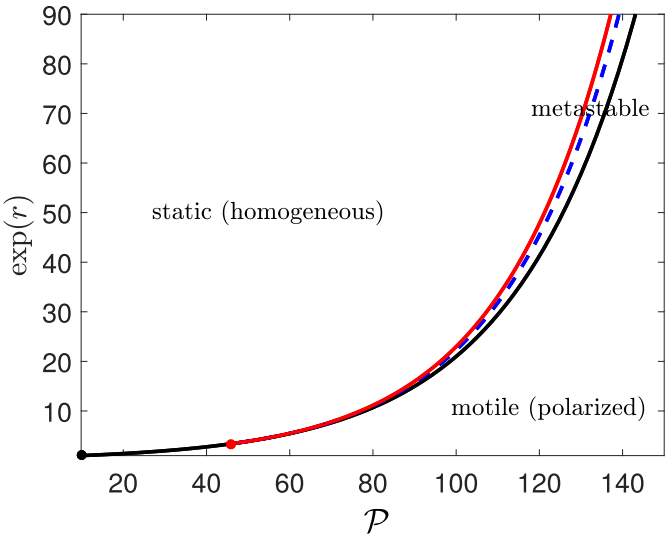

FIGURE 4.3: Phase diagram in the parameter space $(\mathcal{P}, r)$ characterizing the steady state of system (4.1). The black line is the locus of the first bifurcation point and the red line the one of the turning point along the first bifurcating branch (when it exists). The black dashed line represents a "Maxwell line". Above this line, the homogeneous solution is the global minimum of the Lyapunov functional $\mathcal{F}$ while below this line, it is the non-trivial polarized solution.

where Θ is a diffusion coefficient and $\dot{W}(x,t)$ is a spatio-temporal white noise. Thus Σ_s represents small variations of the mechanical stress in the cell skeleton due to some existing random disorder.

The non-dimensional model (4.1) thus becomes

$$\begin{cases} \mathcal{P}(1-c-\delta\sigma_s) = \partial_y w \\ \partial_t c + \partial_y(cw - \partial_y(f(c)c)) = 0 \\ \partial_t \sigma_s - \theta\partial_{yy}\sigma_s = e\dot{\omega}, \end{cases} \tag{4.8}$$

where the new non-dimensional variables are $\theta = \Theta/D$ that quantifies the spatio-temporal correlation of the noise, $e \ll 1$ that represents the small noise magnitude in the system. $\dot{\omega}$ is a normalized white noise such that, denoting $\langle . \rangle$ the ensemble average,

$$\langle \dot{\omega}(y,t) \rangle = 0 \text{ and } \langle \dot{\omega}(y,t)\dot{\omega}(y',t') \rangle = \delta(y-y')\delta(t-t').$$

The stochastic stress $\sigma_s = \Sigma_s/(\chi c_0)$ is shifted by

$$\delta\sigma_s(y,t) = \sigma_s(y,t) - \int_{-1/2}^{1/2} \sigma_s(y',t)dy'$$

such it has a zero spatial average.

Next, we choose $r = 3$ and numerically simulate (4.8) for four values of $\mathcal{P} = 96$, 96.7, 97.5 and 100. The two central values correspond to a metastable regime, see Fig. 4.2, where either the static state or the motile state is the global minimum of

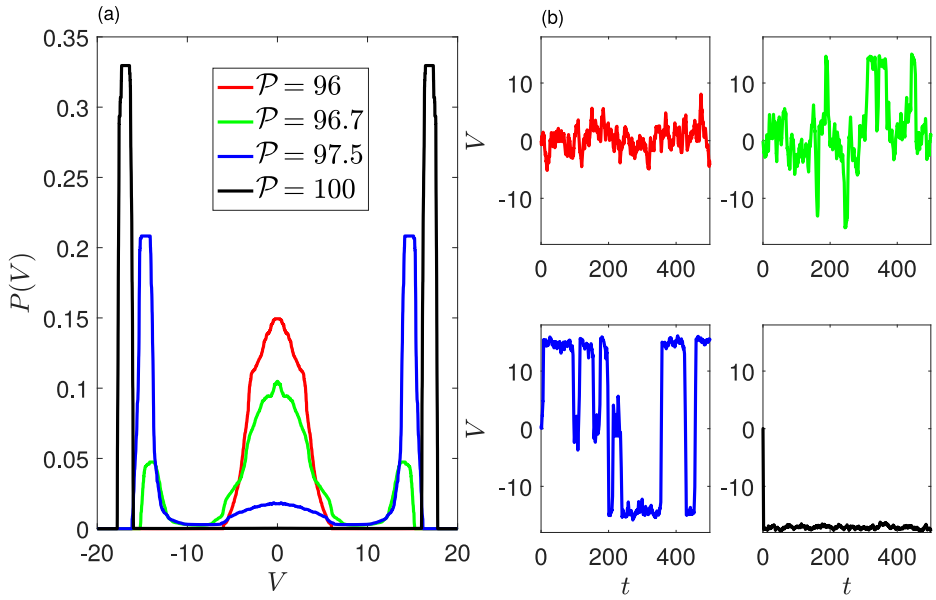

FIGURE 4.4: Effect of stochastic fluctuations on the cell metastable dynamic defined by system (4.8). (a) Probability densities of the distribution of velocity of a moving cell in four typical cases: in red the static configuration is the only steady state of the deterministic cell dynamic, in green both static and motile states are locally stable but the static state is the global minimum of the quasi-potential, in blue the motile state becomes the global minimum and in black only the motile state is locally stable. (b) shows samples of the velocity dynamic in the four cases. Parameter $r = 3$ and parameters defining the noise are $\Theta = 0.01$ and $e = 0.001$. The simulations to obtain the probability densities start from the homogeneous distribution and are run over a non-dimensional time of 1000. The transient state is removed and the distributions are symmetrized with respect to $V = 0$ to minimize the computation cost.

the quasi-potential while the other state is a local minimum. We show on Fig. 4.4, the typical dynamic as well as the probability densities of the cell velocities for all four cases. When the static state is the only existing (and stable) steady state of the deterministic system, the velocity is peaked around $V = 0$. Then, as we reach the metastable regime, the distribution has three peaks corresponding to a static state and the two symmetric motile configurations. The size of the peaks of the probability density of V depends on which state is the global minimum of $\mathcal{F}$ and the system may feature predominantly fluctuations around the static state with rare motile excursions or, on the contrary, a motile dynamic rarely alternating the sign of the velocity and spending a small duration around the static state. As $\mathcal{P}$ increases such that the system leaves the metastable domain, the unstable static state disappears from the velocity distribution.

It is also interesting to interpret these results at the cell population level as metastability can explain why, in a cell population with the same parameters defining their molecular motors dynamics, most of the cells may be almost static with only a certain proportion moving at a large velocity or, on the contrary, most cells can be motile and a few of them static depending which state is the global attractor of the deterministic system.

4.6 Conclusions

We have exhibited one of the simplest model of cell crawling that is independent of its interaction with the substrate as, while they exert vanishingly small traction forces, the molecular motors still produce an internal flow of cytoskeleton that can propel the cell boundary. Such flow has to be coupled with a physical process that insures the recycling of the cytoskeleton building blocks and which is not solved for in this minimalist model. This can be achieved by considering a backflow (Loisy, Eggers, and Liverpool, 2019) or a chemical turnover reaction that depolymerizes the cytoskeleton at the back and polymerizes it at the front (Putelat, Recho, and Truskinovsky, 2018). This substrate independent crawling mode has a variational structure with a quasi-potential that allows to characterize the local and global stability of its steady states. In particular, we find that there exists a region in the non-dimensional parameter space where a static and mobile configuration can co-exist in a metastable fashion. In the presence of an additional small stochastic stress, this leads to the possibility of an intermittent cell dynamics where the static or motile phases of motion dominate depending on which state is the global minimum of the quasi-potential.

Conclusion

It is now widely acknowledged that the extracellular matrix cannot be simply considered as a fixed scaffold supporting the cell during its migration, because a bidirectional interaction occurs between the cell and the substrate at the focal adhesions (a process called mechanoreciprocity). This interaction impacts the cell motility, among other essential functions. The mechanoreciprocity consists in three steps, mechanosensing, mechanotransduction and cell response. However, because of the intrinsic bidirectional feature of the force balance, a part of the mechanoreciprocity pathway is achieved by a bare mechanical process, *i.e.* only through force transmission while ignoring the complexity of the chemo-mechanical coupling occurring at the microstructure level.

In order to extract the cell migration behaviour when considering a simple mechanical mechanoreciprocity, we extended the protrusion-driven and contraction driven models of cell migration on a rigid substrates of Jülicher et al., 2007 and Recho, Putelat, and Truskinovsky, 2015 to the case of migration on a compliant substrate. This amounts to introducing the cell-substrate relative velocity in the linear friction law and building the kernel governing the non-local response of the substrate to cell traction forces.

First we investigated a cell crawling motion driven by the protrusion and retraction velocity of the actin meshwork at the leading and trailing edge in the paradigmatic situation of a semi-infinite incompressible and elastic substrate. Interestingly, just by considering this non-local coupling, the model was able to capture a non-monotonic relationship between the cell velocity and the substrate stiffness and also between the cell velocity and the friction coefficient, both phenomena being observed experimentally. Next we considered a viscous substrate instead, on which the cell propels through the self-organization of its molecular motors. The non-local response of the substrate due to its viscosity is shown to be qualitatively captured by an effective space-dependent coefficient in this case. Compared to the elastic case, the cell exhibited a monotonous decreasing speed with the substrate viscosity, however the traction forces showed a biphasic behaviour with the viscosity. Interestingly, at a vanishing friction and/or viscosity coefficient, cell motility still occurs although the traction forces vanish. This rather counter-intuitive phenomenon has been investigated in depth in the last chapter, by introducing a simple substrate-independent variational model of cell migration. In particular we were able to analytically confirm the critical contractility obtained in chap. 3. The model exhibits a metastable state, in which a small stochastic variation of the stress can induce a cell state switch

between static to motile or motile to static.

By integrating the cell-substrate mechanoreciprocity without its chemo-mechanical contribution, our model was able to extract interesting non-linear behaviours experimentally observed and were able to discriminate pure mechanical effects from biochemical-related ones. In the future, it would be interesting to investigate crawling on non-homogeneous substrate with our model, as capturing durotaxis with our minimalistic would be an interesting result, meaning it would not require the introduction of any *a priori* bias.

Appendix A

Interaction kernel with the substrate with exponential decay

We formulate the new problem where we replace the expression of Φ in (2.16) by $\Phi_{\exp}(x) = Ae^{-|x|}$ where we set the constant

$$A(\epsilon) = \frac{e^{\frac{1}{\epsilon}}\left(\epsilon \log\left(\frac{\sqrt{\epsilon^2+1}+1}{\epsilon}\right) + \sinh^{-1}(\epsilon)\right)}{\left(e^{\frac{1}{\epsilon}} - 1\right)\epsilon},$$

such that $\int_{-1}^{1} \Phi(x/\epsilon)\mathrm{d}x = \int_{-1}^{1} \Phi_{\exp}(x/\epsilon)\mathrm{d}x$. With such exponential kernel, system (2.16) can be written in differential form:

$$\begin{cases} -\alpha^2\partial_{xx}v_x + v_x = -V\partial_x u \\ -\epsilon^2\partial_{xx}u + u = 2\epsilon A\gamma\partial_{xx}v_x \end{cases} \text{ with boundary conditions } \begin{cases} \partial_x v_x|_{-1} = \partial_x v_x|_1 \text{ and } v_x|_1 - v_x|_{-1} = -\Delta V \\ \epsilon\partial_x u|_{-1} - u|_{-1} = 0 \text{ and } \epsilon\partial_x u|_1 + u|_{-1} = 0 \end{cases} \tag{A.1}$$

and the unknown velocity is still fixed by the condition

$$V = V_m + \frac{v_x|_{-1} + v_x|_1}{2}.$$

System (A.1) is a fourth order boundary value problem with a free parameter V that is set by the previous condition. Solving this problem using a continuation method, we construct the $V(\gamma)$ and $V(\alpha)$ curves that we superimpose with their analogue for the elastic kernel Φ on Fig. A.1. We observe that while the global biphasic structure in α is still present, the local one in γ disappears.

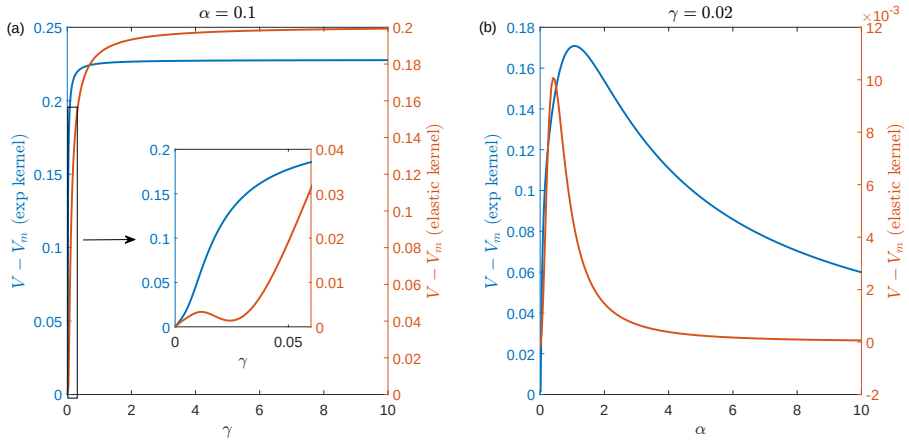

FIGURE A.1: Dependence of the crawling velocity on (a) the substrate softness γ and (b) the substrate slip coefficient α for both the exponential and elastic interaction kernel with the substrate. Parameters are $\epsilon = 0.2$, $\Delta V = 1$ and $V_m = 1.5$.

Appendix B

Experimental and post processing methods

► SYNTHESIS OF HYDROXY-PAAM HYDROGELS

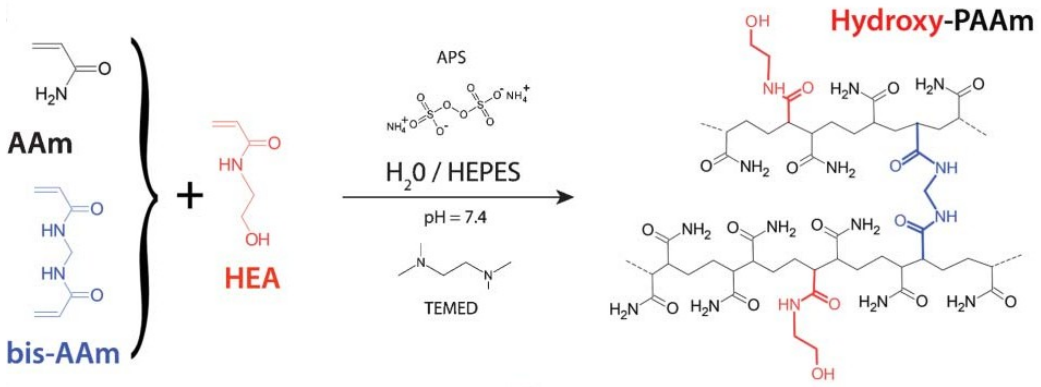

FIGURE B.1: AcrylAmide (AAm, in black), N,N′ methylene–bis–AcrylAmide (bis-AAm, in blue) and N-Hydroxy–EthylAcrylamide (HEA, in red) were mixed together to form hydroxy-PAAm Grevesse et al., 2013.

In order to prepare hydroxy-PAAm gels to be coated with fibronectin for cell adherence, it is necessary to use acrylamide (AAm) mixed with N-hydroxyethylacrylamide (HEA) monomers. The latter contains HO groups that can form a hydrophilic network (see Fig. B.1). Then using bis–acrylamide as a crosslinker and TEMED/APS for catalysis, rapid polymerization of acrylamid monomers is obtained Grevesse, Versaevel, and Gabriele, 2014; Abidine et al., 2018.

Here, we used the protocol explained in Abidine et al., 2018. We prepared solutions by mixing acrylamide (30% weight per weight [w/w]), N-hydroxyethylacrylamide (5.85% w/w), and N,N-methylene-bisacrylamide (2% w/w) in different amounts (Sigma-Aldrich, St. Louis, MO). Three concentrations of bis–acrylamide were used (0.1, 0.3, and 0.6 %), with the acrylamide (3.2%) and N-hydroxyethylacrylamide (1.25%) contents remaining fixed in the final HEPES solution (50 mM). Gels were 70 μm thick with an area 1.5 cm $\times$ 1.5 cm, and were prepared on a glass slide (pre–treated with 3–Aminopropyl–triethoxysilane, APTMS) glued at the bottom of a Petri dish.

The gel rigidity should be chosen as a compromise between the stiffness in physiological conditions and the sufficiently large displacements to be measured in soft gels (on the order of a few μm). Values of elastic modulus (E) between 5kPa and 30 kPa were found to be adequate Peschetola et al., 2013. The elastic Young moduli of the three hydrogels were measured using an Atomic Force Microscope (JPK AFM, NanoWizard II, Berlin) in contact mode, equipped with MLCT cantilevers (pyramidal tips, stiffness 0.01 N/m, Bruker). Five different locations were selected and 5x5 elasticity maps were performed at each location. The values were obtained using the classical relationship $F = \frac{3}{4}\frac{E}{1-\nu^2}\tan\theta\,\delta^2$, where F is the applied force, $\nu \sim 0.5$ is the Poisson ratio, θ the half–pyramid angle, and δ is the indentation. The resulting elastic moduli were found to be 5 ± 1 kPa, 8 ± 1.5 kPa and 28 ± 3 kPa. This is shown in Fig. B.2 with hydrogel elastic moduli increasing with cross-linker concentration as previously measured Abidine, 2015.

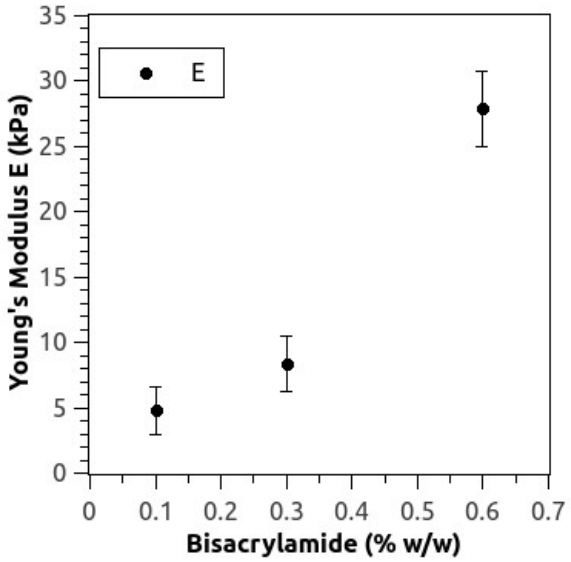

FIGURE B.2: The stiffness of hydroxy-PAAm hydrogels is increasing with the amount of bis-AAm cross-linker Abidine, 2015.

▶ FIBRONECTIN MICROPATTERNING OF HYDROXY-PAAM GELS

Fibronectin (FN) mediates a wide variety of cellular interactions with the ECM and plays an essential role in cell adhesion, migration, growth, and differentiation Pankov and Yamada, 2002. Incubation of fibronectin straight microtracks with a very narrow width (less than 15 μm) and far from each other (more than 40 μm) on micro-fabricated hydroxy-PAAm hydrogels can be used to simulate 1D migration of cells on soft substrates. Here we used a fibronectin micropatterning process by designing the required PDMS[1] stamp Grevesse et al., 2013 as shown in Fig. B.3.

For the preparation of patterns on PDMS, we first made a silicon master using optical lithography with a negative photoresist. Optical lithography is a photographic

[1]Polydimethylsiloxane

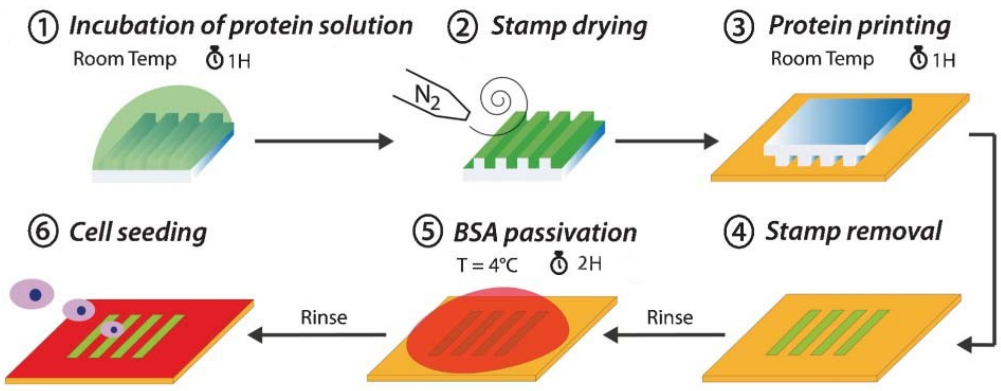

FIGURE B.3: Process of fibronectin micropatterning on hydrogel Grevesse et al., 2013.

method by which a light-sensitive polymer, named a photoresist, is exposed and developed to form 3D features on the silicon substrate. A negative photoresist is one whose UV exposed parts become cross-linked and other parts remain soluble and can be washed away during development. One of the commonly used epoxy–based negative photoresists is SU-8 GM1070, a chemically amplified resist system with excellent sensitivity. The final micropattern presents regions with photoresist and other parts are uncovered. This coated micropattern is needed to shape the PDMS. The common steps for a regular photolithography process are as follows: substrate preparation, photoresist spin coating, prebaking, exposure, post-exposure baking, development, and post-baking Mack, 2016. In order to have the silicon master with about 15 μm in height, we followed the SU8-Photoepoxy GM 1070 datasheet. The essential principle behind this photoresist operation is the change in the solubility of the photoresist in the developer, upon exposure to light. Here we used UV laser exposure with 10 μm laser beamwidth in order to change the solubility of the photoresist and as a result we obtain designed photoresist micro-patterns on top of the silicon wafer (Fig. B.4). Then PDMS is poured onto the substrate, baked at 60°C for 2h, and is finally peeled off.

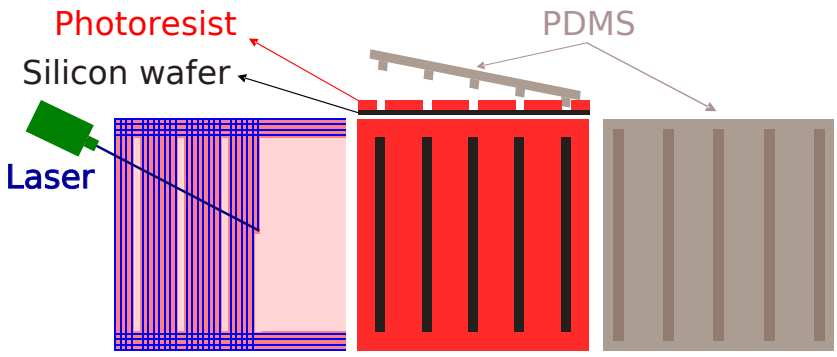

FIGURE B.4: Process of the PDMS stamp fabrication

According to Fig. B.4, by giving a designed pattern to the laser machine, it is possible to make our micro–pattern directly on the photoresist. There are two essential

parameters, the percentage of exposure energy and the time of exposure. The time of exposure comes from the velocity of the moving laser beam. By testing different exposure energy percentages and velocities, we found that 100 % and 25 mm/s give the best results for 15 μm height of photoresist layer on the substrate.

In order to check the final shape of designed PDMS stamps with different patterns (Fig. B.5a), we cut very thin cross-section layers of PDMS and imaged them under an optical microscope (Fig. B.5b–e). Then we measured the width (w) and height (h) of the lines, as well as the distance between two lines (D) using Fiji^{TM} software. According to Fig. B.5f, the results show that $h \simeq 15\,\mu$m and $D \simeq 45\,\mu$m are almost similar for all PDMS with different w. Also, Fig. B.5g shows that the smallest w that we could obtain was $w \simeq 8\,\mu$m. Although for 1D migration it would be better to have stamps with smaller w, the width of laser beam that was accessible (10 μm) gave this limitation for us.

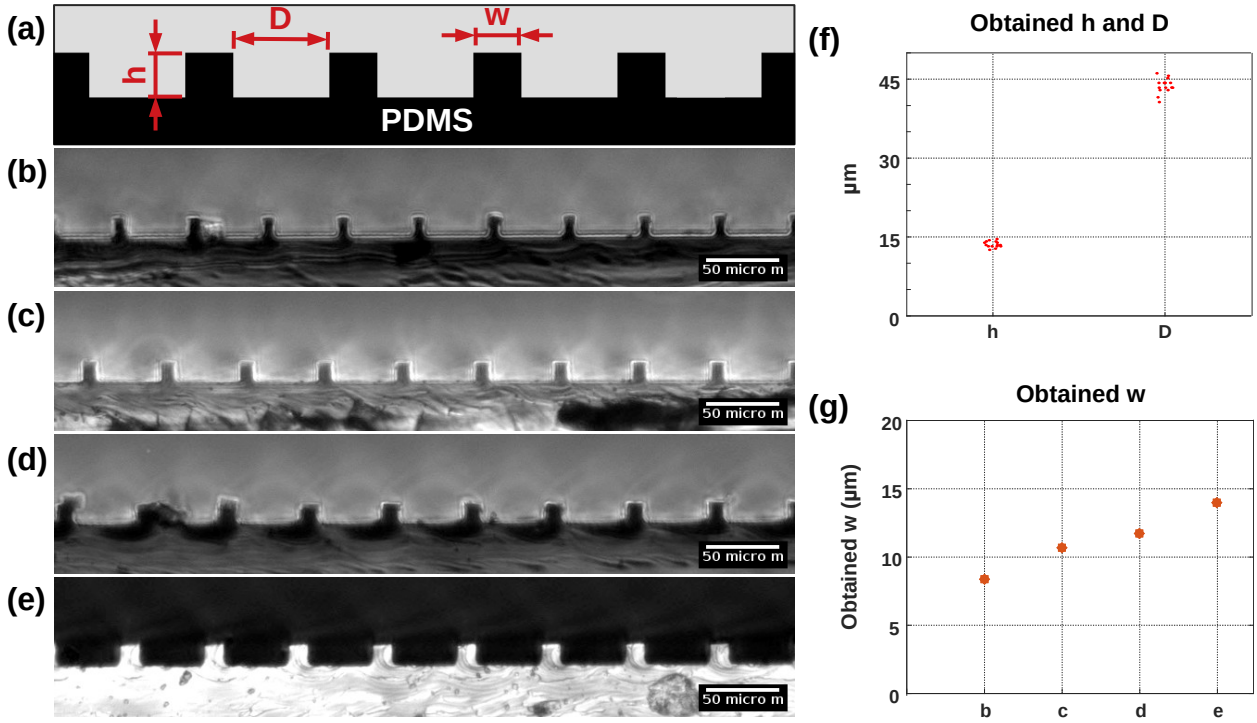

FIGURE B.5: a) Schematic of a cross-section of PDMS stamp with w (width of lines), h (height of lines), and D (distance between two lines) b, c, d, e) Images of PDMS cross-sections with different w f) Distribution of measured values $h \simeq 15\,\mu$m and $D \simeq 45\,\mu$m. g) Values of w: 8, 11, 12, and 14 μm for images b, c, d, and e respectively.

► CELL CULTURE AND SEEDING

First, cells were cultured at 37°C and 5% CO_2 atmosphere. Following growth, they were detached using trypsin-EDTA, resuspended in complete culture medium (RPMI + 10 % FBS + 1 % penicillin–streptomycin) and finally deposited on the gel. A small drop (50 μL) containing $\sim$ 2,000 cells was set onto the micropatterned gel surface (1.5 cm $\times$ 1.5 cm) bound to the bottom of a Petri dish, and left to adhere for 15 min. Then 2 mL of culture medium were added into the Petri dish. It was then

possible to observe them individually under the microscope using the green channel (FITC) of the fluorescence microscope.

▶ **LIVE CELL MICROSCOPY**

We used an Olympus IX83 inverted microscope equipped with a Hamamatsu Camera (Orca G) to capture fluorescent images in green (FITC), blue (DAPI), and red (TRITC). Thus, it is possible to capture fluorescence of the actin cytoskeleton using the green channel (FITC), and the beads fluorescence within the substrate via the blue channel (DAPI) of the microscope. TRITC was only used in a few cases to check the track width, using rhodamin fibronectin (Cytoskeleton, Inc.).

The microscope is equipped with the possibility to program the image acquisition mode (CellSens^{TM}). The loop we chose allowed to quickly capture two images (green and blue). It is important to select the appropriate image frequency, since we need to capture fast actin polymerization but we should not expose the cells to too much light (phototoxicity). Our loop was a series of 15 pairs of images (FITC then DAPI) taken every 5 seconds, then a 15–minute pause was held before starting a new series of images. Thus actin fibers and beads could be followed over short periods of time during cell migration for about 30 minutes.

At the end of the experiment, we added trypsin to the Petri dish to detach the cells from the substrate. After waiting for 15 min, the last beads image was captured to obtain the initial beads position when the gel is in a rest state. Finally, series of FITC and DAPI images could be treated using image processing in Matlab^{TM} and Fiji^{TM} software for tracking beads and PIV analyses of actin motion.

▶ **IMAGE PROCESSING**

Image acquisition

In this work, a code formerly written (Mireux, 2019; Jahangiri, 2020) was improved. The initial code is divided into four main parts. It reads 16-bit images taken from the microscope and converts them into a data sheet. Next, it finds the cell, produces masks at different times and calculates cell contours. Then, it finds the beads and follows their movement in time. Finally, it selects the beads under the cell and calculates the total displacements of beads (DAPI) between the rest state and the present configuration of the gel.

Due to the addition of trypsin to detach cells and also possible shifts of the camera (thermal changes), it was necessary to rewrite the code in order to process images. Here, the DAPI images (15 DAPI images taken every 5 seconds + DAPI image taken after adding trypsin to the Petri dish) as blue color and FITC images (15 FITC images taken every 5 seconds + blank image corresponding to the absence of cell on the substrate) as green color were merged. Then we used the StackReg plugin Thévenaz, 2009 in the Fiji software to shift all images in order to correct for any camera shift. The idea of this plugin is to align or match a stack of images. When the plugin has finished, the current slice works as a global anchor.

Then by separating the blue component from the green one, we could track beads in time using the DAPI images (saved as blue color images) and achieve PIV (Particle Image Velocity) measurements on FITC images (saved as green color images).

Tracking Beads

By using a previously written Matlab code (Mireux, 2019), we could find bead positions at each time (for example DAPI images at t_0 and t_1 in Fig. B.6). The particle tracker is a routine adapted for Matlab of a previous program Crocker and Weeks, 2011. This function reads the first DAPI image and processes it interactively to figure out what settings are needed in order to identify all the beads. It then repeats this process on all the images. Finally, it links the beads coordinates to form trajectories.

By replacing the last image (obtained after adding trypsin, Fig. B.6a at time t_0) from the end of the treated DAPI stack to the first and running the tracking function in Matlab, we obtain a list of trajectories including the beads identities numbered from 1 to the total number of beads as well as their positions (x,y) at each time t (for example at time t_1, Fig. B.6b). Using this data, it is possible to find displacements for each bead between two times (Fig. B.6c).

Actin and PIV

We found Particle Image Velocimetry (PIV) to be a suitable technique to estimate the actin velocity. In general, PIV is an optical technique of flow visualization used to obtain instantaneous velocity measurements and related properties in fluids. Basically, a pair of images is divided into smaller areas named interrogation windows. The cross-correlation between these image sub-regions measures the optical flow (incremental displacement or velocity of the objects) between the two images. To improve resolution, higher PIV resolution can be achieved by progressively decreasing the interrogation window size Tseng, 2014. The PIV analysis was conducted using the MATLAB tool "PIVlab" Thielicke and Stamhuis, 2014, typical outputs from the analysis are shown Fig. B.7.

The post-processing protocol is summarized in Fig. B.8.

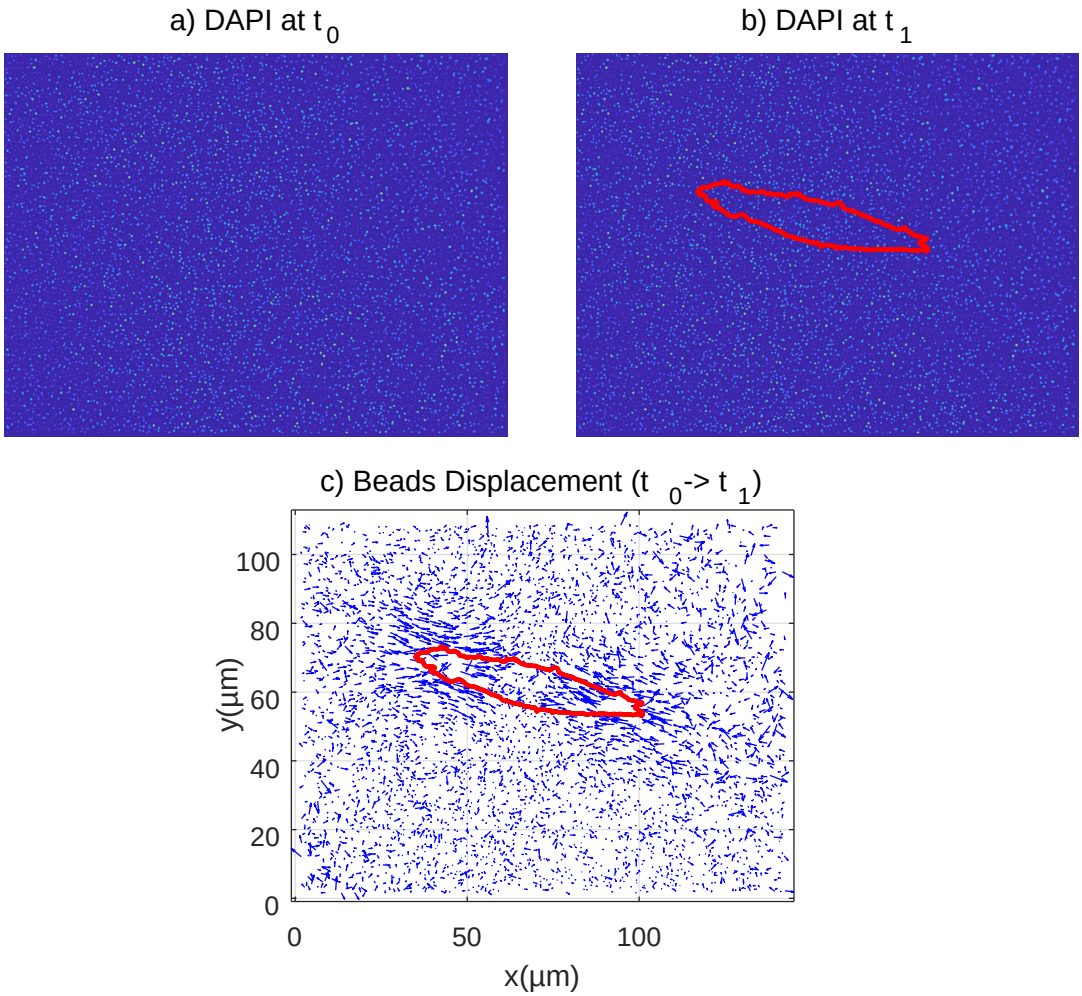

FIGURE B.6: DAPI images. a) time t_0 (after adding trypsin), b) time t_1; c) Beads displacement between t_0 and t_1

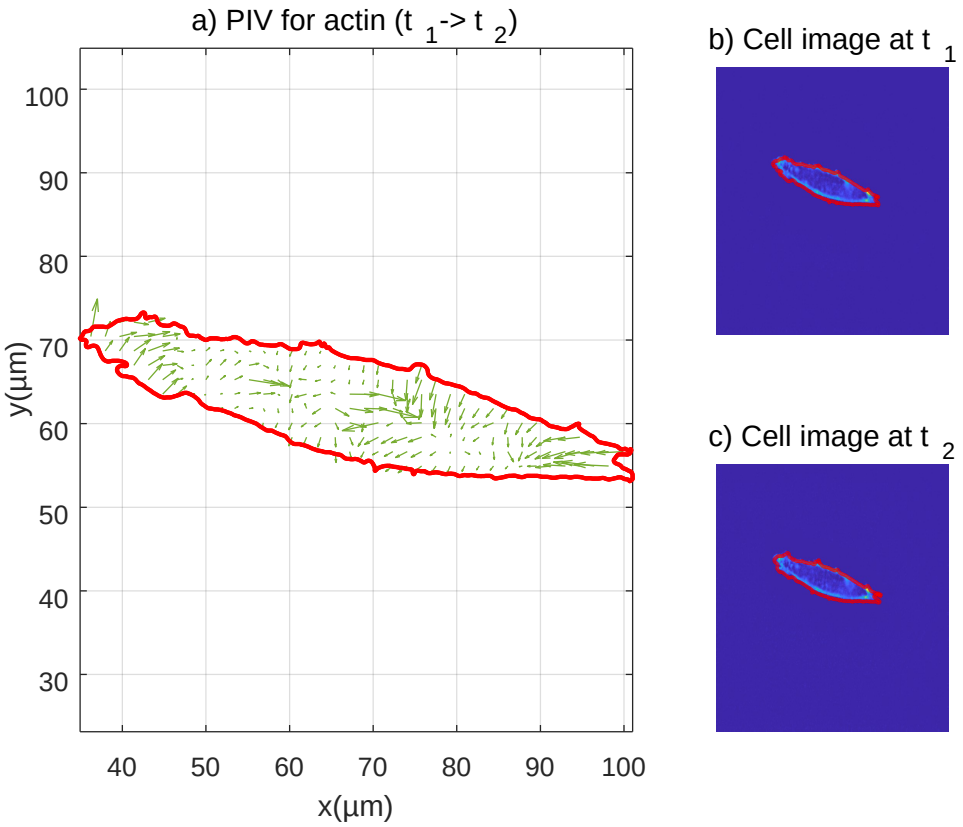

FIGURE B.7: Actin displacements between t_1 and $t_2 = t_1 + 5$s (a); Cell shape at t_1 (b) and t_2 (c)

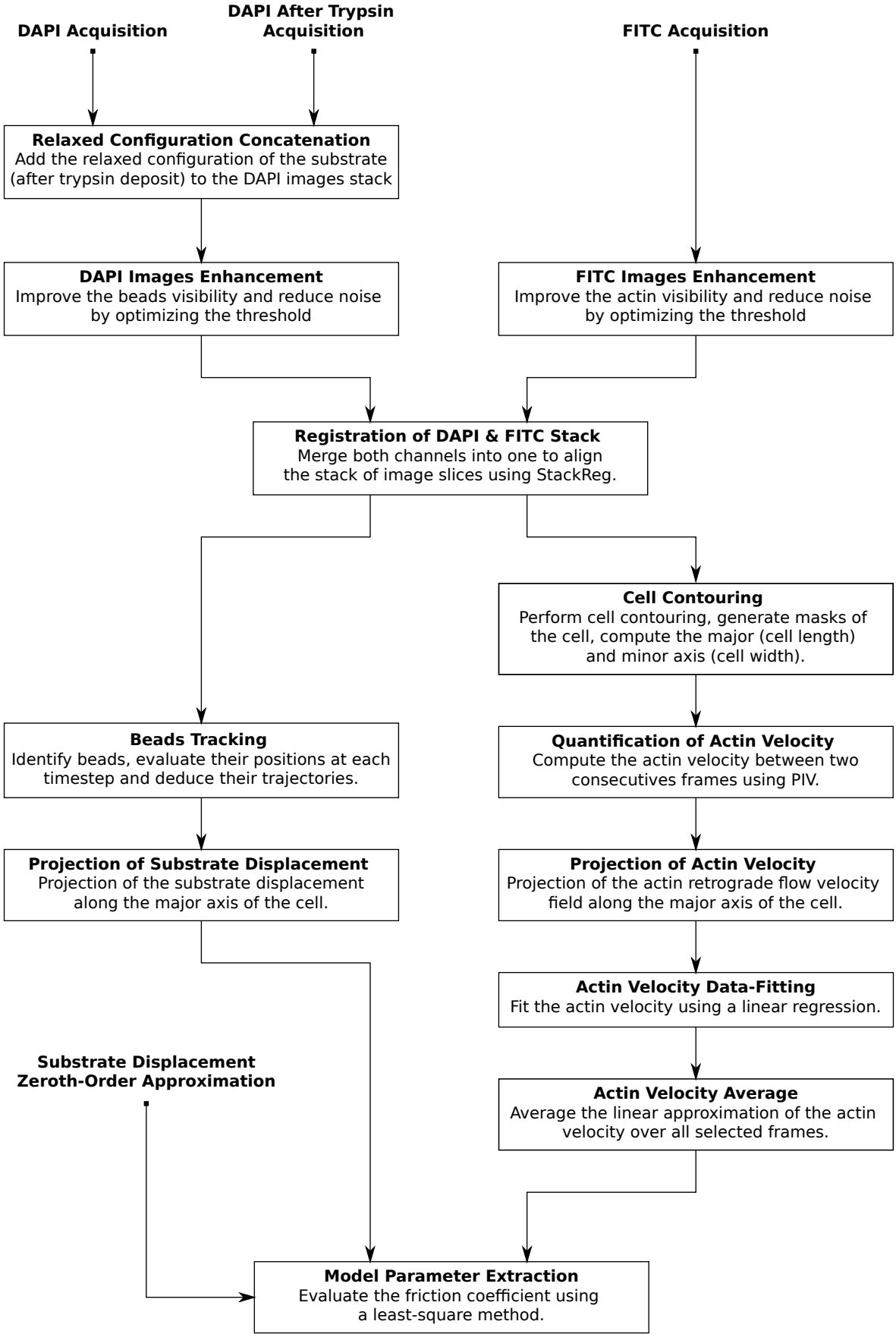

FIGURE B.8: Post-processing method to extract the friction coefficient ζ from the experimental data.

Appendix C

Technical results

C.1 Normal forms of the solutions bifurcating from the homogeneous solution

The steady states of (4.1), for which $\partial_t c = 0$ correspond to the solutions of the equation

$$\partial_y \left(\frac{\partial_y (f(c)c)}{c} \right) + \mathcal{P}(c-1) = 0 \tag{C.1}$$

with Neumann boundary conditions at $y = \pm 1/2$. Eq. (C.1) has the homogeneous solution $c \equiv 1$. From this solution, non-trivial solutions bifurcate at specific values of $\mathcal{P}$. These bifurcation points and the behavior of the bifurcating solutions can be investigated by plugging a Taylor expansion of c and $\mathcal{P}$ in Eq. (C.1),

$$\begin{aligned} c(y,t) &= 1 + \epsilon c_1(y) + \epsilon^2 c_2(y) + \epsilon^3 c_3(y) + ... \\ \mathcal{P} &= \mathcal{P}_0 + \epsilon \mathcal{P}_1 + \epsilon^2 \mathcal{P}_2 + \epsilon^3 \mathcal{P}_3 + ... \end{aligned} \tag{C.2}$$

where the $\mathbb{L}^2$ norm of the c_i is fixed to one and ϵ is a small parameter.

At first order we find that the operator

$$(f(1) + f'(1))\partial_{yy} c_1 + \mathcal{P}_0 c_1 = 0,$$

with Neumann boundary conditions becomes degenerate at the values of $\mathcal{P}_0$ indexed by the integer $k \geq 1$:

$$\mathcal{P}_0^k = (f(1) + f'(1))k^2 \pi^2.$$

The smallest value of $\mathcal{P}_0$ corresponding to $k = 1$ is denoted $\mathcal{P}_c$. At each $\mathcal{P}_0^k$, a solution bifurcates along the two symmetric eigenvectors

$$c_1^k(y) = \pm\sqrt{2}\cos(\pi k(y + 1/2)).$$

At the second order in ϵ, we obtain using the Fredholm alternative that $\mathcal{P}_1^k = 0$ and

$$c_2^k(y) = \Big[c_1^k(y)\sqrt{22f(1)f'(1) + 7f'(1)^2 + 4\left(f(1) - f'(1)\right)f''(1) + 7f(1)^2 - 2f''(1)^2} \\ + \sqrt{2}c_1^k(2y)\left(f(1) - f''(1) - f'(1)\right)\Big] \,/\, \left[3\left(f'(1) + f(1)\right)\right]$$

Finally, the value of $\mathcal{P}_2^k$ fixing the local nature of the bifurcation is classically given by the third order expansion:

$$\mathcal{P}_2^k = \Big[\pi^2 k^2 \left(-4f''(1)^2 - 10f'(1)^2 + f(1)\left(3f^{(3)}(1) + 11f''(1) + 8f'(1)\right)\right. \\ \left. + \; f'(1)\left(3f^{(3)}(1) - 5f''(1)\right) + 2f(1)^2\right)\Big] \,/\, \left[12\left(f'(1) + f(1)\right)\right]$$

Taking the simple form $f(c) = 1 + rc^2$ where r is a non-dimensional parameter fixing the strength of the steric hindrance, we obtain

$$\mathcal{P}_2^k = \frac{\pi^2 k^2\left(-18r^2 + 21r + 1\right)}{18r + 6},$$

which is positive for $r < r_c = (7 + \sqrt{57})/12$ indicating a super-critical pitchfork bifurcation while it becomes negative when $r > r_c$ indicating a sub-critical pitchfork bifurcation.

C.2 Local stability

The local (or linear) stability of a certain steady state $c_{\text{eq}}(y)$ is given by the second variation of $\mathcal{F}$ at this point. Based on the expressions of $\mathcal{E}$ and $\mathcal{S}$, we obtain the following quadratic form:

$$\delta^2\mathcal{F}[h] = \frac{\mathcal{P}^2}{2}\int_{-1/2}^{1/2}\int_{-1/2}^{1/2}\max(y,z)h(z)h(y)dydz \\ + \frac{\mathcal{P}}{2}\int_{-1/2}^{1/2} s''(c_{\text{eq}}(y))h(y)^2 dy. \tag{C.3}$$

If $\delta^2\mathcal{F}$ is strongly positive for all test functions h that satisfy the Neumann boundary conditions at $\pm 1/2$ and the constraint

$$\int_{-1/2}^{1/2} h(y)dy = 0,$$

the steady state c_{eq} is linearly stable. It is unstable otherwise. Such condition is equivalent to checking the positivity of the eigenvalues of the polar form associated to $\delta^2\mathcal{F}$. This leads to the eigenproblem

$$\mathcal{P}^2\int_{-1/2}^{1/2}\max(y,z)h(z)dz + \mathcal{P}s''(c_{\text{eq}}(y))h(y)dy = \mu h(y),$$

where μ is the eigenvalue and h the eigenvector. Differentiating twice this relation, we obtain the boundary value problem

$$\begin{gathered}\mathcal{P}^2 h(y) = \partial_{yy}\left((\mu - \mathcal{P}s''(c_{\text{eq}}(y)))h(y)\right) \\ \text{with } \partial_y h(\pm 1/2) = 0.\end{gathered} \tag{C.4}$$

Each eigenvector being defined up to a constant, we additionally impose the normalization

$$\int_{-1/2}^{1/2} h(y)^2 dy = 1.$$

The local stability of the homogeneous solution $c_{\text{eq}}(y) \equiv 1$ can be resolved analytically since the solution of (C.4) is explicit in this case and we obtain:

$$\mu = \frac{-\mathcal{P}^2}{k^2\pi^2} + \mathcal{P}(f(1) + f'(1)),$$

where $k \geq 1$ is a positive integer. It therefore exists at least one negative eigenvalue as soon as $\mathcal{P} > \mathcal{P}_c$ indicating the loss of local stability of the homogeneous solution past the first bifurcation point.

For the non-homogeneous branches, it is not straightforward to solve (C.4) and we investigate the local stability properties numerically by using the test function combining the first Q modes

$$h(y) = \sum_{k=1}^{Q} h_k c_1^k(y)$$

in (C.3). We thus have to test the positivity of the eigenvalues of the symmetric matrix $\delta\mathbb{F} = \delta\mathbb{E} - \mathcal{P}\delta\mathbb{S}$ with

$$\delta\mathbb{E}_{i,j} = \frac{\mathcal{P}^2}{2}\int_{-1/2}^{1/2}\int_{-1/2}^{1/2} \max(y,z) c_1^i(y) c_1^j(z) dy dz = -\frac{\mathcal{P}^2\delta_{ij}}{2i^2\pi^2}$$

and

$$\delta\mathbb{S}_{i,j} = -\frac{1}{2}\int_{-1/2}^{1/2} s''(c_{\text{eq}}(y)) c_1^i(y) c_1^j(y) dy$$

and where δ_{ij} is the Kronecker symbol and i, j are integers in $1..Q$.

Appendix D

Stochastic sliding friction

In the present appendix, we investigate the friction of an actin filament sliding at a constant imposed speed v_0 on a compliant substrate from a microscopic perspective using an agent-based model, in order to understand the influence of the substrate stiffness on the local relationship between the actin-induced traction force and the actin retrograde flow velocity. The present approach is based on the stochastic clutch-model (Chan and Odde, 2008; Sens, 2013) described in the general introduction (see chap. 1). In the model developed by Chan and Odde, 2008, the friction relationship we are actually trying to deduce is *a priori* assumed and follows Hill's law (Hill, 1938) and the stiffness of the substrate is approximated by a single spring. In contrast, Sens, 2013 used an analytical mean-field theory to take into account the displacement of the substrate and deduced non-monotonous actin force-velocity relationship. Whereas in this mean-field theory the attached linkers are assumed to be uniformly distributed, we wanted to computationally investigate the effect of their spatial distribution on the sliding friction. We also proposed an improvement to the method used in classical motor-clutch simulations.

D.1 The model and algorithm workflow

The actin filament is equiped with N uniformly distributed linkers, which can be either attached to the substrate or detached. The configuration of the linker i at time t is given by $\mathcal{C}_i(t)$ where it is equal to unity if attached, to zero otherwise.

At the start of the simulation, all linkers are assumed to be attached to the substrate, thus the initial condition is given by

$$\forall i \in [1, N], \quad \mathcal{C}_i(0) = 1.$$

The problem can be formulated as finding the next reaction to occur (binding or unbinding) between the N possible reactions and the time at which it occurs. At a reaction site, a bond can switch from attached to detached with a rate k^- and from detached to attached with a rate k^+. The attachment rate k^+ is assumed to be constant while the detachment rate is force sensitive and follows Bell's law (Bell, 1978). Therefore supposing the i-th linker being attached, the detachment rate at

time t reads

$$k_i^-(t) = k^0 \exp\left(f_i(t)/f^*\right),$$

where k^0 represents the unloaded unbinding rate, $f_i(t)$ is the force in bond i and f^* is the characteristic bond breaking force.

Step 1: The first reaction method The *first reaction method* introduced by Gillespie, 1976, is an algorithm allowing to predict the next reaction to occur (either bond binding: B or unbinding: U) and the time at which it occurs. First an expression of the probability density $p(t, B/U)$ that a reaction occurs in a defined timespan at a specific bonding site is deduced from the attachment and detachment rates. Next a random value of the next event time t is obtained according to $p(t, B/U)$ using the *inversion method*. This method consists in computing the cumulative distribution function CDF based on $p(t, B/U)$ and defined as

$$CDF(t) = \int_{t_0}^{t} p(t', B/U)dt',$$

representing the probability of an event to occur between two times t_0 and t. Then a random number r is generated from the uniform distribution in the unit interval and the random time of the next event is deduced by inverting CDF

$$t = CDF^{-1}(r).$$

This process is repeated for each of the N binding sites and the first reaction to occur is the one having the shortest generated time.

At the reaction site i, the probability at time t_0 that the next event will occur in the differential time interval $[t,\ t + \mathrm{d}t]$ is given by

$$p_i(t, B/U)\mathrm{d}t = P_i^0(t) \cdot p_i(B/U)\mathrm{d}t \tag{D.1}$$

where $P_i^0(t)$ is the probability at time t_0 that no event will occur in the time interval $[t_0,\ t]$ at the reaction site i, and $p_i(B/U)\mathrm{d}t$ is the probability at reaction site i that the event will occur in the next differential time interval $[t,\ t + \mathrm{d}t]$ defined as

$$p_i(B/U) = \mathcal{C}_i(t_0)k_i^-(t) + [1 - \mathcal{C}_i(t_0)]k_+. \tag{D.2}$$

Considering once again a Markov chain, the probability at time t_0 that the $i-$th bond will remain in the same state until $t + \mathrm{d}t$, $P_i^0(t + \mathrm{d}t)$, is defined by the product of the probability that its configuration will not change between t_0 and t, $P_i^0(t)$ and the probability that no change will happen between t and $t + \mathrm{d}t$ given by $1 - p_i(B/U)\mathrm{d}t$

$$P_i^0(t + \mathrm{d}t) = P_i^0(t)[1 - p_i(B/U)\mathrm{d}t], \tag{D.3}$$

which in the limit $\mathrm{d}t \to 0$ becomes

$$\frac{\mathrm{d}P_i^0(t)}{\mathrm{d}t} = -p_i(B/U)P_i^0(t), \tag{D.4}$$

whose solution is

$$P_i^0(t) = \exp\left(-\int_{t_0}^{t} p_i(B/U)\mathrm{d}t'\right). \tag{D.5}$$

Plugging this expression into (D.1) gives

$$p_i(t, B/U) = p_i(B/U)\exp\left(-\int_{t_0}^{t} p_i(B/U)\mathrm{d}t'\right) = -\frac{d}{dt}\left[\exp\left(-\int_{t_0}^{t} p_i(B/U)\mathrm{d}t'\right)\right]. \tag{D.6}$$

The probability at the $i-$th binding site of an event to occur between times t_0 and t_i is given by the cumlative distribution function $CDF_i(t_i) = \int_{t_0}^{t_i} p_i(t, B/U)dt$, plugging (D.2) into (D.6) we obtain

$$CDF_i(t_i) = -\exp\left(-\int_{t_0}^{t_i}\left[\mathcal{C}_i(t_0)k_i^-(t) + (1-\mathcal{C}_i(t_0))k_+\right]\mathrm{d}t\right), \tag{D.7}$$

A classical implicit assumption when computationally modeling sliding friction with the help of a Gillespie algorithm, is that the forces within the bonds remain constant between two configuration changes, *i.e.* during one timestep. However this assumption oversimplifies the problem, because the filament is sliding between two events, therefore the bonds continue to extend and thus the bonds loading rates do not vanish. In the general case, the loading rate within a bond remains constant between two reactions, because the filament is sliding at constant speed, therefore the force within a bond i at time t is given exactly by

$$f_i(t) = f_i(t_0) + \partial_t f_i(t_0)(t - t_0), \tag{D.8}$$

where f_i is the force in the $i-$th bond and $\partial_t f_i$ is the corresponding loading rate.

Plugging this expression of the force into the expression of the mechanosensitive unbinding rate and combining with (D.2), (D.7) becomes

$$\begin{aligned} CDF_i(t_i) = -\exp\big(&\mathcal{C}_i(t_0)k^0\frac{f^*}{\dot{f}_i(t_0)}\exp\left(\frac{f_i(t_0)}{f^*}\right)\left[\exp\left(\frac{\dot{f}_i(t_0)(t-t_0)}{f^*}\right) - 1\right] \\ &+[1-\mathcal{C}_i(t_0)]k_+(t-t_0)\big) \end{aligned} \tag{D.9}$$

Then we deduce the time of the next occurring event at the $i-$th linker using

$$t_i = CDF^{-1}(r_i), \tag{D.10}$$

where r_i is a random number generated from the uniform distribution, and we finally obtain

The time of the next reaction at the site i

$$\begin{cases} t_i = t_0 + \frac{f^*}{\partial_t f_i} \ln\left[1 - \frac{\partial_t f_i}{f^* k^0} \ln(r_i) \exp\left(-\frac{f_i(t_0)}{f^*}\right)\right], & \text{if } \mathcal{C}_i(t_0) = 1 \\ t_i = t_0 + \frac{1}{k_+} \ln\left(\frac{1}{r_i}\right), & \text{if } \mathcal{C}_i(t_0) = 0. \end{cases} \tag{D.11}$$

The first reaction occurs at the site k such that the first reaction time $t_k = \min_i t_i$. At the end of this step the time is updated to $t_0 := t_0 + t_k$.

Step 2: The force balance The event type and location obtained from the Gillespie step allows to update the forces in the bonds by performing a force balance.

Assuming a semi-infinite elastic and incompressible substrate, within the small deformation framework the displacement of the substrate at the location of the $i-$th bond is given by the Boussinesq-Cerruti solution and is the sum of a local contribution due to the force exerted by the $i-$th bond and a non-local contribution due to the forces of all other bonds

$$u_i^s(t_0) = \underbrace{\sum_{\substack{j=1 \\ j\neq i}}^{N_a} \frac{3 f_j(t_0)}{2\pi E_s |x_i - x_j|}}_{\text{Non-local contribution}}, + \underbrace{\frac{3 f_i(t_0)}{2\pi E_s a}}_{\text{Local contribution}} \tag{D.12}$$

where N_a is the number of attached linkers, x_k corresponds to the attached position of the $k-$th bond on the substrate in the undeformed configuration, E_s represents the Young modulus of the substrate and a is a cutoff length of the order of the integrin head diameter. Furthermore assuming that the bonds are hookean springs characterized by a stiffness k_b and a zero rest length. The filament slides at a constant velocity v_0, therefore the force in the $i-$th bond reads

$$f_i(t_0) = k_b[v_0(t_0 - t_i^b) - u_i^s(t_0)], \tag{D.13}$$

where t_i^b represents the time at which the $i-$th linker attached. Thus we deduce another expression of the substrate displacement,

$$u_i^s(t_0) = v_0(t_0 - t_i^b) - \frac{f_i(t_0)}{k_b}. \tag{D.14}$$

Equating (D.12) and (D.14) gives

$$v_0(t_0 - t_i^b) = \sum_{\substack{j=1 \\ j\neq i}}^{N_a} \frac{3 f_j(t_0)}{2\pi E_s |x_i - x_j|} + \left(\frac{3}{2\pi E_s a} + \frac{1}{k_b}\right) f_i(t_0). \tag{D.15}$$

The forces in the bonds are computed by solving the system (D.15).

By differentiating (D.15) with respect to time, we obtain a similar system of N_a equations in $\partial_t f$

$$v_0 = \sum_{\substack{j=1 \\ j\neq i}}^{N_a} \frac{3\partial_t f_j(t_0)}{2\pi E_s |x_i - x_j|} + \left(\frac{3}{2\pi E_s a} + \frac{1}{k_b}\right) \partial_t f_i(t_0). \tag{D.16}$$

The loading rates in the bonds are computed by solving the system (D.16).

Using a trapezoidal integration formula, the time-averaged sum of the exerted forces by the bonds on the substrate over one time step is given by

$$\langle F \rangle = \frac{1}{t - t_0} \int_{t_0}^{t} \sum_{i=1}^{N} f_i(t')dt' = \sum_{i=1}^{N} \left[f_i(t_0) + \partial_t f_i(t_0) \left(\frac{t - t_0}{2}\right)\right]. \tag{D.17}$$

The computed forces and loading rates become an input for the Gillespie algorithm in order to update the time-dependent unloading rate. The process is iterated until an arbitrary number of simulations.

D.2 The dimensionless problem

Introducing the scaled quantities $\bar{t} = tk^0$, $\bar{k_+} = k_+/k^0$, $\bar{f} = f/f^*$, $\overline{\partial_t f} = \partial_t f/(f^* k^0)$, we re-write (D.11)

$$\begin{cases} \bar{t_i} = \bar{t_0} + \frac{1}{\overline{\partial_t f_i}} \ln\left[1 - \overline{\partial_t f_i} \ln(r_i) \exp(-\bar{f_i}(\bar{t_0}))\right], & \text{if } C_i(\bar{t_0}) = 1 \\ \bar{t_i} = \bar{t_0} + \frac{1}{\bar{k_+}} \ln\left(\frac{1}{r_i}\right), & \text{if } C_i(\bar{t_0}) = 0. \end{cases} \tag{D.18}$$

Re-scaling (D.15) gives

$$\bar{v_0}(\bar{t_0} - \bar{t_i^b}) = \mathcal{L}\left(\mathcal{K} \sum_{\substack{j=1 \\ j\neq i}}^{N_a} \frac{\bar{f}_j(t_0)}{|\bar{x}_i - \bar{x}_j|} + (1 + \mathcal{K})\bar{f}_i(t_0) \right), \tag{D.19}$$

while (D.16) becomes

$$\bar{v_0} = \mathcal{L}\left(\mathcal{K} \sum_{\substack{j=1 \\ j\neq i}}^{N_a} \frac{\overline{\partial_t f}_j(\bar{t_0})}{|\bar{x}_i - \bar{x}_j|} + (1 + \mathcal{K})\overline{\partial_t f}_i(\bar{t_0}) \right), \tag{D.20}$$

and the normalized time-averaged traction force

$$\langle \bar{F} \rangle = \frac{1}{N} \sum_{i=1}^{N} \left[\bar{f}_i(\bar{t_0}) + \overline{\partial_t f_i}(\bar{t_0}) \left(\frac{\bar{t} - \bar{t_0}}{2}\right)\right], \tag{D.21}$$

where $\mathcal{L}$ and $\mathcal{K}$ are two dimensionless numbers defined as

$$\mathcal{L} = f^* / (k_b a),$$

the ratio between the bond failure length and the cut-off length a and

$$\mathcal{K} = 3k_b / (2\pi E_s a),$$

represents the ratio between the bond rigidity and substrate rigidity.

D.3 Results

In fig. D.1, we show the evolution of the time-averaged traction force with the sliding velocity for a stiff $\mathcal{K} = 0.5$ and a soft substrate $\mathcal{K} = 100$, where each dot represents a simulation. On both rigidities the relationship between the force and the velocity is biphasic. This result is in qualitative agreement with Sens, 2013. On a soft substrate the shift in monotony occurs much later than on a stiff substrate, indeed it is located at $v_0 \simeq 3000$ for $\mathcal{K} = 100$ and at $v_0 \simeq 50$ for $\mathcal{K} = 0.5$. Throughout this work, we assumed a viscous friction law (1.7) to model the cell-substrate interaction, which is valid at sufficiently low speed, as illustrated here. Interestingly this domain of validity is extended as the substrate becomes softer, meaning that for very soft substrate the assumption of linear friction law could be always valid.

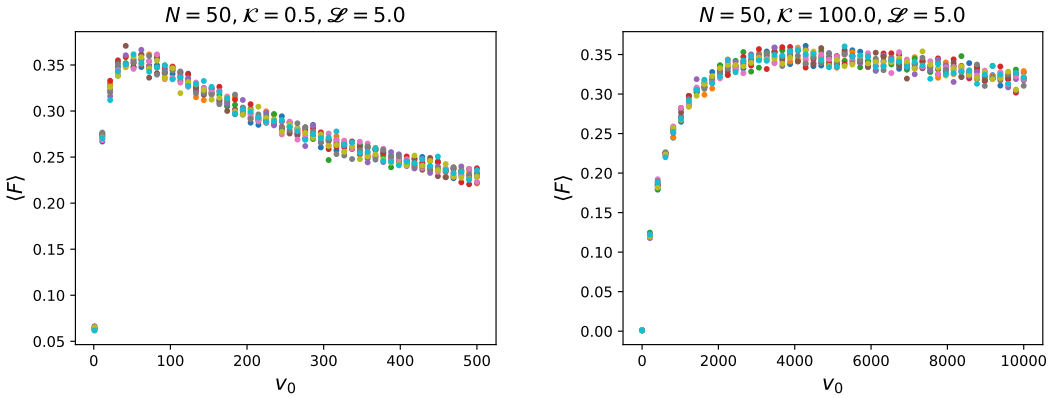

FIGURE D.1: Biphasic evolution of the mean traction force with the sliding speed (left) on a stiff ($\mathcal{K} = 0.5$) and (right) on a soft substrate ($\mathcal{K} = 100$).

In fig. D.1, we show the evolution of the time-averaged traction force with the substrate rigidity at two different filament sliding velocities $v_0 = 20$ and $v_0 = 100$. At $v_0 = 20$, the force is monotonically increasing with the substrate rigidity, however at $v_0 = 100$, the relationship becomes biphasic, meaning that the force transmission is maximal at an optimal substrate rigidity. These results are also in qualitative agreement with Sens, 2013.

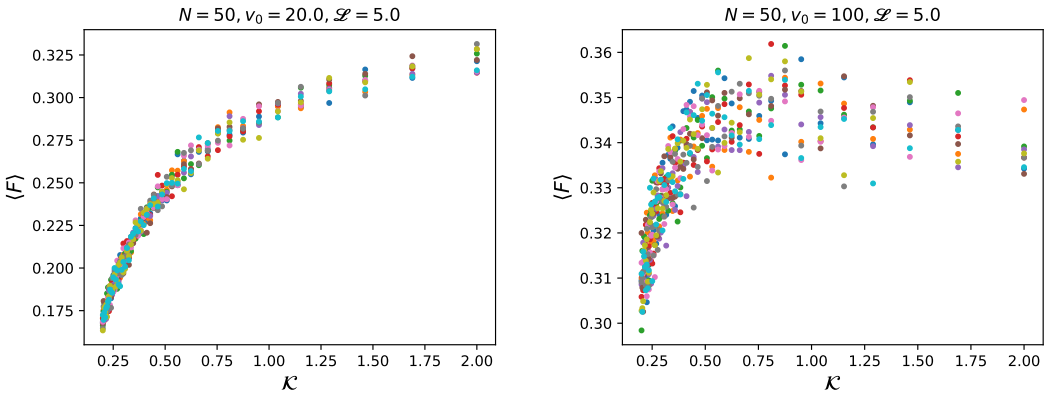

FIGURE D.2: Evolution of the mean traction force with the substrate rigidity.

D.4 Simplified model

In this section, we want to discard the non-local effects due to the compliance of the substrate by using a simple one-spring (of stiffness k_s) representation of the substrate rigidity, in the fashion of Chan and Odde, 2008. We re-write the previous model to match this representation, where only the overall substrate displacement is taken into account due to the single spring model. Therefore the force balance at the interface gives

$$u^s(t_0) = (1/k_s) \sum_{i=1}^{N_a} f_i(t_0). \tag{D.22}$$

Moreover (D.14) becomes

$$u^s(t_0) = v_0(t_0 - t_i^b) - \frac{f_i(t_0)}{k_b}. \tag{D.23}$$

Following the same methods as in sec. D.1 we obtain

$$v_0(t_0 - t_i^b) = \sum_{\substack{j=1 \\ j \neq i}}^{N_a} \frac{1}{k_s} + \left(\frac{1}{k_s} + \frac{1}{k_b} \right) f_i(t_0). \tag{D.24}$$

The forces in the bonds are computed by solving the system (D.15).

By differentiating (D.24) with respect to time, we get

$$\partial_t f = v_0 / \left(\frac{N_a}{k_s} + \frac{1}{k_b} \right) \tag{D.25}$$

We observe that, in this simplified representation the loading rate is identical in each and every bond, because all the bonds are linked at both ends to the same moving rigid surfaces.

Using the same previous scaling parameters, the dimensionless problem reads

$$\bar{v_0}(\bar{t_0} - \bar{t_i^b}) = \mathcal{L}\left(\mathcal{K}\sum_{\substack{j=1\\ j\neq i}}^{N_a}\frac{\bar{f}_j(t_0)}{|\bar{x}_i - \bar{x}_j|} + (1+\mathcal{K})\bar{f}_i(t_0)\right), \tag{D.26}$$

while (D.25) becomes

$$\overline{\partial_t f} = \bar{v_0}/\left(\mathcal{L}(1+N_a\mathcal{K})\right), \tag{D.27}$$

where $\mathcal{K} = k_b/k_s$. The stochastics part remains unchanged.

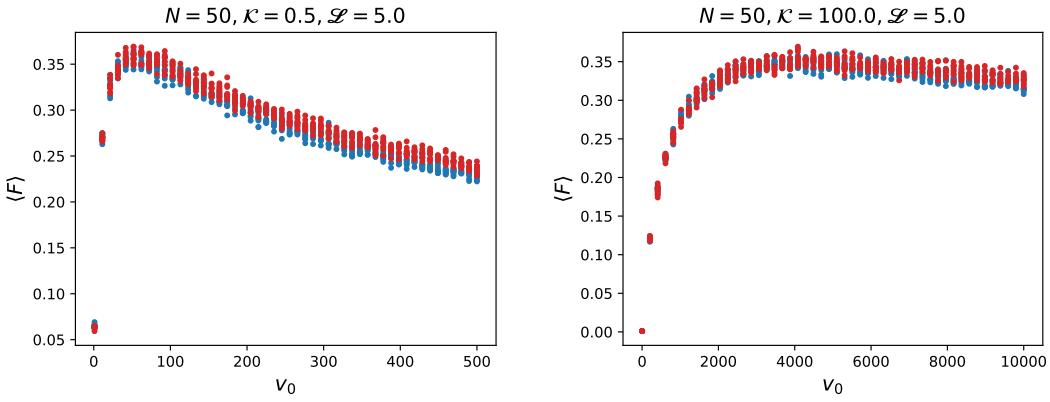

FIGURE D.3: Force-velocity relationship comparison between the previous (blue) and the simplified model (red)

In fig. D.3 we compare the force-velocity relationship between the previous (blue) and the simplified model (red) on a soft and on a stiff substrate. In both cases, the two models deliver similar results, meaning that the non-locality does not play a significant role in this specific case. Therefore the approximation made by Chan and Odde, 2008 to model deformation of the substrate by a single spring is quite accurate when modeling stochastic sliding friction.

D.5 Conclusion

In this part we investigated the friction of an actin filament sliding at constant speed on a compliant substrate using a method based on the stochastic clutch-model (Chan and Odde, 2008; Sens, 2013), in order to understand the influence of the substrate stiffness on the local relationship between the actin-induced traction force and the actin retrograde flow velocity. We developed a computational model, that takes into account the local deformations of the substrate and proposed an improvement to the stochastic algorithm by considering time-dependent unloading rates. The results were in good agreement with Sens, 2013, as we obtained the expected force-velocity biphasic relationship. We showed that the domain of validity of the viscous friction law (1.7) depends on the stiffness of the substrate, being wider for softer substrate.

We also showed the equivalence of this model with a simplified model, which integrates the compliance of the substrate with a single spring, suggesting that the non-local effects are not meaningful when considering the sliding friction of a passive rigid filament at the scale of focal adhesion.

It would be interesting to compare this model with the classical model (time-independent unloading rates) in order to confirm (or not) its relevance.

Bibliography

Abercrombie, Michael (1980). "The Croonian Lecture, 1978-The crawling movement of metazoan cells". In: *Proceedings of the Royal Society of London. Series B. Biological Sciences* 207.1167, pp. 129–147.

Abidine, Yara (2015). "Propriétés mécaniques de cellules cancéreuses mesurées par AFM". PhD thesis. Université Grenoble Alpes.

Abidine, Yara et al. (2018). "Mechanosensitivity of cancer cells in contact with soft substrates using AFM". In: *Biophys. J.* 114, pp. 1165–1175.

Alt, Wolfgang and Micah Dembo (1999). "Cytoplasm dynamics and cell motion: two-phase flow models". In: *Mathematical Biosciences* 156.1, pp. 207 –228. ISSN: 0025-5564. DOI: https://doi.org/10.1016/S0025-5564(98)10067-6. URL: http://www.sciencedirect.com/science/article/pii/S0025556498100676.

Ambrosi, Davide (2006). "Cellular traction as an inverse problem". In: *SIAM Journal on Applied Mathematics* 66.6, pp. 2049–2060.

Ambrosi, Davide and Anna Zanzottera (2016). "Mechanics and polarity in cell motility". In: *Physica D: Nonlinear Phenomena* 330, pp. 58–66.

Bangasser, Benjamin L et al. (2017). "Shifting the optimal stiffness for cell migration". In: *Nature communications* 8.1, pp. 1–10.

Barnhart, Erin et al. (2015). "Balance between cell- substrate adhesion and myosin contraction determines the frequency of motility initiation in fish keratocytes". In: *Proceedings of the National Academy of Sciences* 112.16, pp. 5045–5050.

Barnhart, Erin L. et al. (May 2011). "An Adhesion-Dependent Switch between Mechanisms That Determine Motile Cell Shape". In: *PLOS Biology* 9.5, pp. 1–19. DOI: 10.1371/journal.pbio.1001059. URL: https://doi.org/10.1371/journal.pbio.1001059.

Bell, GI (1978). "Models for the specific adhesion of cells to cells". In: *Science* 200.4342, pp. 618–627. ISSN: 0036-8075. DOI: 10.1126/science.347575. eprint: https://science.sciencemag.org/content/200/4342/618.full.pdf. URL: https://science.sciencemag.org/content/200/4342/618.

Bergert, Martin et al. (2015). "Force transmission during adhesion-independent migration". In: *Nature cell biology* 17.4, pp. 524–529.

Biben, T. and C. Misbah (2003). "Tumbling of vesicles under shear flow within an advected-field approach". In: *Phys. Rev. E* 67 (3), p. 031908. DOI: 10.1103/PhysRevE.67.031908. URL: https://link.aps.org/doi/10.1103/PhysRevE.67.031908.

Biben, Thierry, Klaus Kassner, and Chaouqi Misbah (2005). "Phase-field approach to three-dimensional vesicle dynamics". In: *Phys. Rev. E* 72 (4), p. 041921. DOI:

10.1103/PhysRevE.72.041921. URL: https://link.aps.org/doi/10.1103/PhysRevE.72.041921.

Blanch-Mercader, Carles and J Casademunt (2013). "Spontaneous motility of actin lamellar fragments". In: *Physical review letters* 110.7, p. 078102.

Boyd, John P (2001). *Chebyshev and Fourier spectral methods*. Courier Corporation.

Burnette, Dylan T et al. (2014). "A contractile and counterbalancing adhesion system controls the 3D shape of crawling cells". In: *Journal of Cell Biology* 205.1, pp. 83–96.

Callan-Jones, A C and R Voituriez (2013). "Active gel model of amoeboid cell motility". In: *New Journal of Physics* 15.2, p. 025022. DOI: 10.1088/1367-2630/15/2/025022. URL: https://doi.org/10.1088%2F1367-2630%2F15%2F2%2F025022.

Camley, Brian A et al. (2013). "Periodic migration in a physical model of cells on micropatterns". In: *Physical review letters* 111.15, p. 158102.

Camley, Brian A. et al. (2017). "Crawling and turning in a minimal reaction-diffusion cell motility model: Coupling cell shape and biochemistry". In: *Phys. Rev. E* 95 (1), p. 012401. DOI: 10.1103/PhysRevE.95.012401. URL: https://link.aps.org/doi/10.1103/PhysRevE.95.012401.

Canuto, Claudio et al. (2012). *Spectral methods in fluid dynamics*. Springer Science & Business Media.

Chan, Clarence E. and David J. Odde (2008). "Traction Dynamics of Filopodia on Compliant Substrates". In: *Science* 322.5908, pp. 1687–1691. ISSN: 0036-8075. DOI: 10.1126/science.1163595. eprint: https://science.sciencemag.org/content/322/5908/1687.full.pdf. URL: https://science.sciencemag.org/content/322/5908/1687.

Chandler, Chelsea et al. (2019). "The double edge sword of fibrosis in cancer". In: *Translational Research* 209. Pathologic fibrosis: disease mechanisms and novel therapeutics, pp. 55 –67. ISSN: 1931-5244. DOI: https://doi.org/10.1016/j.trsl.2019.02.006. URL: http://www.sciencedirect.com/science/article/pii/S1931524419300386.

Chavanis, Pierre-Henri (2015). "Generalized stochastic Fokker-Planck equations". In: *Entropy* 17.5, pp. 3205–3252.

Crocker, John C and Eric R Weeks (2011). "Particle tracking using IDL". In: *Retreived from http://www. physics. emory. edu/faculty/weeks//idl*.

Dado, Dekel and Shulamit Levenberg (2009). "Cell–scaffold mechanical interplay within engineered tissue". In: *Seminars in Cell I& Developmental Biology* 20.6. Regenerative Biology and Medicine: II and Patterning and Evolving the Vertebrate Forebrain, pp. 656 –664. ISSN: 1084-9521. DOI: https://doi.org/10.1016/j.semcdb.2009.02.001. URL: http://www.sciencedirect.com/science/article/pii/S1084952109000214.

Dembo, Micah and Francis Harlow (1986). "Cell motion, contractile networks, and the physics of interpenetrating reactive flow". In: *Biophysical journal* 50.1, pp. 109–121.

Dembo, Micah et al. (1996). "Imaging the traction stresses exerted by locomoting cells with the elastic substratum method". In: *Biophysical journal* 70.4, pp. 2008–2022.

Deshpande, Vikram S, Robert M McMeeking, and Anthony G Evans (2006). "A bio-chemo-mechanical model for cell contractility". In: *Proceedings of the National Academy of Sciences* 103.38, pp. 14015–14020.

— (2007). "A model for the contractility of the cytoskeleton including the effects of stress-fibre formation and dissociation". In: *Proceedings of the Royal Society A: Mathematical, Physical and Engineering Sciences* 463.2079, pp. 787–815.

DiMilla, PA, Kenneth Barbee, and DA Lauffenburger (1991). "Mathematical model for the effects of adhesion and mechanics on cell migration speed". In: *Biophysical journal* 60.1, pp. 15–37.

Discher, Dennis, Paul Janmey, and Yu-Li Wang (Dec. 2005). "Tissue Cells Feel and Respond to the Stiffness of Their Substrate". In: *Science (New York, N.Y.)* 310, pp. 1139–43. DOI: 10.1126/science.1116995.

Doedel, E. J., H. B. Keller, and J. P. Kernevez (1991). "Numerical analysis and control of bifurcation problems". In: *Int. J. Bifurcation and Chaos* 1.3. AUTO 07P available via Internet from http://indy.cs.concordia.ca/auto/, pp. 493–520.

Dokukina, Irina V. and Maria E. Gracheva (2010). "A Model of Fibroblast Motility on Substrates with Different Rigidities". In: *Biophysical Journal* 98.12, pp. 2794 –2803. ISSN: 0006-3495. DOI: https://doi.org/10.1016/j.bpj.2010.03.026. URL: http://www.sciencedirect.com/science/article/pii/S0006349510003589.

Doyle, Andrew D et al. (2013). "Dimensions in cell migration". In: *Current opinion in cell biology* 25.5, pp. 642–649.

Dufort, C, M Paszek, and V Weaver (2011). "Balancing forces: architectural control of mechanotransduction". In: *Nat Rev Mol Cell Biol* 12, pp. 308–319. DOI: 10.1038/nrm3112.

Dvorak, Harold F (1986). "Tumors: wounds that do not heal". In: *New England Journal of Medicine* 315.26, pp. 1650–1659.

Elosegui-Artola, Alberto, Xavier Trepat, and Pere Roca-Cusachs (2018). "Control of Mechanotransduction by Molecular Clutch Dynamics". In: *Trends in Cell Biology* 28.5, pp. 356 –367. ISSN: 0962-8924. DOI: https://doi.org/10.1016/j.tcb.2018.01.008. URL: http://www.sciencedirect.com/science/article/pii/S0962892418300175.

Engler, Adam J et al. (2006). "Matrix elasticity directs stem cell lineage specification". In: *Cell* 126.4, pp. 677–689.

Farutin, Alexander et al. (2019). "Crawling in a fluid". In: *Physical review letters* 123.11, p. 118101.

Frank, Till Daniel (2005). *Nonlinear Fokker-Planck equations: fundamentals and applications*. Springer Science & Business Media.

Geiger, B, J Spatz, and A Bershadsky (2009). "Environmental sensing through focal adhesions". In: *Nat Rev Mol Cell Biol* 10, pp. 21–33.

Gillespie, Daniel T (1976). "A general method for numerically simulating the stochastic time evolution of coupled chemical reactions". In: *Journal of Computational Physics* 22.4, pp. 403 –434. ISSN: 0021-9991. DOI: https://doi.org/10.1016/0021-9991(76)90041-3. URL: http://www.sciencedirect.com/science/article/pii/0021999176900413.

Giomi, Luca and Antonio DeSimone (2014). "Spontaneous division and motility in active nematic droplets". In: *Physical review letters* 112.14, p. 147802.

Giverso, Chiara and Luigi Preziosi (2018). "Mechanical perspective on chemotaxis". In: *Physical Review E* 98.6, p. 062402.

Goychuk, Andriy et al. (2018). "Morphology and Motility of Cells on Soft Substrates". In: arXiv: 1808.00314 [physics.bio-ph].

Grevesse, Thomas, Marie Versaevel, and Sylvain Gabriele (2014). "Preparation of hydroxy-PAAm hydrogels for decoupling the effects of mechanotransduction cues". In: *JoVE (Journal of Visualized Experiments)* 90, e51010.

Grevesse, Thomas et al. (2013). "A simple route to functionalize polyacrylamide hydrogels for the independent tuning of mechanotransduction cues". In: *Lab on a Chip* 13.5, pp. 777–780.

Haak, Andrew J., Qi Tan, and Daniel J. Tschumperlin (2018). "Matrix biomechanics and dynamics in pulmonary fibrosis". In: *Matrix Biology* 73, pp. 64 –76. ISSN: 0945-053X. DOI: https://doi.org/10.1016/j.matbio.2017.12.004. URL: http://www.sciencedirect.com/science/article/pii/S0945053X17303220.

Hassan, Abdel-Rahman, Thomas Biel, and Taeyoon Kim (2019). "Mechanical Model for Durotactic Cell Migration". In: *ACS Biomaterials Science & Engineering* 5.8, pp. 3954–3963. DOI: 10.1021/acsbiomaterials.8b01365. eprint: https://doi.org/10.1021/acsbiomaterials.8b01365. URL: https://doi.org/10.1021/acsbiomaterials.8b01365.

Hennig, K et al. (2020). "Stick-slip dynamics of cell adhesion triggers spontaneous symmetry breaking and directional migration of mesenchymal cells on one-dimensional lines". In: *Science Advances* 6.1, eaau5670.

Hill, Archibald Vivian (1938). "The heat of shortening and the dynamic constants of muscle". In: *Proceedings of the Royal Society of London. Series B - Biological Sciences* 126.843, pp. 136–195. DOI: 10.1098/rspb.1938.0050. eprint: https://royalsocietypublishing.org/doi/pdf/10.1098/rspb.1938.0050. URL: https://royalsocietypublishing.org/doi/abs/10.1098/rspb.1938.0050.

Humphrey, Jay D, Eric R Dufresne, and Martin A Schwartz (2014). "Mechanotransduction and extracellular matrix homeostasis". In: *Nature reviews Molecular cell biology* 15.12, pp. 802–812.

Jahangiri, Amir (2020). "1D migration of cancer cells on soft substrates: experiments and theory". In: *Masters 2 Report, 'Nanoscience and Nanotechnology', Grenoble*.

Johnson, Kenneth Langstreth (1987). *Contact mechanics*. Cambridge university press.

Juanes-García, Alba, Clara Llorente-González, and Miguel Vicente-Manzanares (2018). "Nonmuscle Myosin II". In: *Encyclopedia of Signaling Molecules*. Ed. by Sangdun

Choi. Cham: Springer International Publishing, pp. 3541–3553. ISBN: 978-3-319-67199-4. DOI: 10.1007/978-3-319-67199-4_101734. URL: https://doi.org/10.1007/978-3-319-67199-4_101734.

Jülicher, F. et al. (2007). "Active behavior of the Cytoskeleton". In: *Physics Reports* 449.1. Nonequilibrium physics: From complex fluids to biological systems III. Living systems, pp. 3 –28. ISSN: 0370-1573. DOI: https://doi.org/10.1016/j.physrep.2007.02.018. URL: http://www.sciencedirect.com/science/article/pii/S0370157307001330.

Karpenko, L.N (1966). "Approximate solution of a singular integral equation by means of jacobi polynomials". In: *Journal of Applied Mathematics and Mechanics* 30.3, pp. 668–675. ISSN: 0021-8928. DOI: https://doi.org/10.1016/0021-8928(67)90103-7. URL: https://www.sciencedirect.com/science/article/pii/0021892867901037.

Kruse, K et al. (2006). "Contractility and retrograde flow in lamellipodium motion". In: *Physical biology* 3.2, p. 130.

Kuusela, Esa and Wolfgang Alt (2009). "Continuum model of cell adhesion and migration". In: *Journal of mathematical biology* 58.1-2, p. 135.

Kwon, Taejin et al. (2019). "Stochastic and heterogeneous cancer cell migration: experiment and theory". In: *Scientific reports* 9.1, pp. 1–13.

Lacker, H. M. and Charles Peskin (1986). "A mathematical method for the unique determination of cross-bridge properties from steady-state mechanical and energetic experiments on macroscopic muscle". English (US). In: *Lectures on Mathematics in the Life Sciences*. Vol. 16. AMS, pp. 121–153.

Lampi, Marsha C. and Cynthia A. Reinhart-King (2018). "Targeting extracellular matrix stiffness to attenuate disease: From molecular mechanisms to clinical trials". In: *Science Translational Medicine* 10.422. ISSN: 1946-6234. DOI: 10.1126/scitranslmed.aao0475. eprint: https://stm.sciencemag.org/content/10/422/eaao0475.full.pdf. URL: https://stm.sciencemag.org/content/10/422/eaao0475.

Landau, Lev Davidovich and Eugin M Lifshitz (1959). *Course of Theoretical Physics Vol 7: Theory and Elasticity*. Pergamon press.

Larripa, Kamila and Alex Mogilner (2006). "Transport of a 1D viscoelastic actin–myosin strip of gel as a model of a crawling cell". In: *Physica A: Statistical Mechanics and its Applications* 372.1, pp. 113–123.

Le Goff, Thomas, Benno Liebchen, and Davide Marenduzzo (2020). "Actomyosin contraction induces in-bulk motility of cells and droplets". In: *Biophysical Journal* 119.5, pp. 1025–1032.

Lelidis, I and J-F Joanny (2013). "Interaction of focal adhesions mediated by the substrate elasticity". In: *Soft Matter* 9.46, pp. 11120–11128.

Li, Ying, Prabhakar Bhimalapuram, and Aaron R Dinner (2010). "Model for how retrograde actin flow regulates adhesion traction stresses". In: *Journal of Physics:*

Condensed Matter 22.19, p. 194113. DOI: 10.1088/0953-8984/22/19/194113. URL: https://doi.org/10.1088%2F0953-8984%2F22%2F19%2F194113.

Lo, Chun-Min et al. (2000). "Cell Movement Is Guided by the Rigidity of the Substrate". In: *Biophysical Journal* 79.1, pp. 144 –152. ISSN: 0006-3495. DOI: https://doi.org/10.1016/S0006-3495(00)76279-5. URL: http://www.sciencedirect.com/science/article/pii/S0006349500762795.

Löber, Jakob, Falko Ziebert, and Igor S Aranson (2014). "Modeling crawling cell movement on soft engineered substrates". In: *Soft matter* 10.9, pp. 1365–1373.

Loisy, Aurore, Jens Eggers, and Tanniemola B Liverpool (2019). "Tractionless self-propulsion of active drops". In: *Physical review letters* 123.24, p. 248006.

Ma, Xiaoyue et al. (2013). "Fibers in the Extracellular Matrix Enable Long-Range Stress Transmission between Cells". In: *Biophysical Journal* 104.7, pp. 1410 –1418. ISSN: 0006-3495. DOI: https://doi.org/10.1016/j.bpj.2013.02.017. URL: http://www.sciencedirect.com/science/article/pii/S0006349513002075.

Mack, Chris (2016). "Semiconductor Lithography (Photolithography)-The Basic Process". In: *The Basics of Microlithography*. URL: http://lithoguru.com/scientist/lithobasics.html#top.

Maiuri, Paolo et al. (2012). "The first world cell race". In: *Current Biology* 22.17, R673–R675.

Maiuri, Paolo et al. (2015). "Actin flows mediate a universal coupling between cell speed and cell persistence". In: *Cell* 161.2, pp. 374–386.

Michel, Richard et al. (2013). "Mathematical framework for traction force microscopy". In: *ESAIM: Proceedings*. Vol. 42. EDP Sciences, pp. 61–83.

Mireux, Matthieu (2019). "Migration cellulaire Expérimentale: force de traction et flux d'actine". In: *Stage 2 année PHELMA, Grenoble*.

Mogilner, A and D Verzi (Apr. 2003). "A Simple 1-D Physical Model for the Crawling Nematode Sperm Cell". In: *Journal of statistical physics* 110, pp. 1169–1189. DOI: 10.1023/A:1022153028488.

Möhl, Christoph (2005). "Modellierung von Adhäsions-und Cytoskelett-Dynamik in Lamellipodien migratorischer Zellen". PhD thesis. Diploma thesis, Universität Bonn.

Molecular biology of the cell. (2008). eng. 5th ed. New York: Garland Science. ISBN: 9780815341055.

Nicolas, A and SA Safran (2004). "Elastic deformations of grafted layers with surface stress". In: *Physical Review E* 69.5, p. 051902.

Nicolas, Alice and Samuel A Safran (2006). "Limitation of cell adhesion by the elasticity of the extracellular matrix". In: *Biophysical journal* 91.1, pp. 61–73.

Novak, Igor L. et al. (2004). "Cooperativity between Cell Contractility and Adhesion". In: *Phys. Rev. Lett.* 93 (26), p. 268109. DOI: 10.1103/PhysRevLett.93.268109. URL: https://link.aps.org/doi/10.1103/PhysRevLett.93.268109.

Oers, René F. M. van et al. (Aug. 2014). "Mechanical Cell-Matrix Feedback Explains Pairwise and Collective Endothelial Cell Behavior In Vitro". In: *PLOS Computational Biology* 10.8, pp. 1–14. DOI: 10.1371/journal.pcbi.1003774. URL: https://doi.org/10.1371/journal.pcbi.1003774.

Palecek, Sean P, Alan F Horwitz, and Douglas A Lauffenburger (1999). "Kinetic model for integrin-mediated adhesion release during cell migration". In: *Annals of biomedical engineering* 27.2, pp. 219–235.

Palecek, Sean P et al. (1997). "Integrin-ligand binding properties govern cell migration speed through cell-substratum adhesiveness". In: *Nature* 385.6616, pp. 537–540.

Paluch, Ewa K, Irene M Aspalter, and Michael Sixt (2016). "Focal adhesion–independent cell migration". In: *Annual review of cell and developmental biology* 32, pp. 469–490.

Pankov, Roumen and Kenneth M Yamada (2002). "Fibronectin at a glance". In: *Journal of cell science* 115.20, pp. 3861–3863.

Pelham, Robert J. and Yu-li Wang (1997). "Cell locomotion and focal adhesions are regulated by substrate flexibility". In: *Proceedings of the National Academy of Sciences* 94.25, pp. 13661–13665. ISSN: 0027-8424. DOI: 10.1073/pnas.94.25.13661. eprint: https://www.pnas.org/content/94/25/13661.full.pdf. URL: https://www.pnas.org/content/94/25/13661.

Peschetola, Valentina et al. (2013). "Time-dependent traction force microscopy for cancer cells as a measure of invasiveness". In: *Cytoskeleton* 70.4, pp. 201–214.

Peyton, Shelly R. and Andrew J. Putnam (2005). "Extracellular matrix rigidity governs smooth muscle cell motility in a biphasic fashion". In: *Journal of Cellular Physiology* 204.1, pp. 198–209. DOI: 10.1002/jcp.20274. eprint: https://onlinelibrary.wiley.com/doi/pdf/10.1002/jcp.20274. URL: https://onlinelibrary.wiley.com/doi/abs/10.1002/jcp.20274.

Putelat, Thibaut, Pierre Recho, and Lev Truskinovsky (2018). "Mechanical stress as a regulator of cell motility". In: *Physical Review E* 97.1, p. 012410.

Qian, Jin, Jizeng Wang, and Huajian Gao (2008). "Lifetime and Strength of Adhesive Molecular Bond Clusters between Elastic Media". In: *Langmuir* 24.4. PMID: 18179265, pp. 1262–1270. DOI: 10.1021/la702401b. eprint: https://doi.org/10.1021/la702401b. URL: https://doi.org/10.1021/la702401b.

Recho, P, T Putelat, and L Truskinovsky (2013). "Contraction-driven cell motility". In: *Physical review letters* 111.10, p. 108102.

Recho, P., T. Putelat, and L. Truskinovsky (2019). "Active gel segment behaving as an active particle". In: *Phys. Rev. E* 100 (6), p. 062403. DOI: 10.1103/PhysRevE.100.062403. URL: https://link.aps.org/doi/10.1103/PhysRevE.100.062403.

Recho, Pierre, Thibaut Putelat, and Lev Truskinovsky (2015). "Mechanics of motility initiation and motility arrest in crawling cells". In: *Journal of the Mechanics and Physics of Solids* 84, pp. 469 –505. ISSN: 0022-5096. DOI: https://doi.org/10.1016/j.jmps.2015.08.006. URL: http://www.sciencedirect.com/science/article/pii/S0022509615300612.

Recho, Pierre and Lev Truskinovsky (2013). "Asymmetry between pushing and pulling for crawling cells". In: *Physical Review E* 87.2, p. 022720.

Reinhart-King, Cynthia A., Micah Dembo, and Daniel A. Hammer (2008). "Cell-Cell Mechanical Communication through Compliant Substrates". In: *Biophysical Journal* 95.12, pp. 6044 –6051. ISSN: 0006-3495. DOI: https://doi.org/10.1529/biophysj.107.127662. URL: http://www.sciencedirect.com/science/article/pii/S0006349508820188.

Roskelley, C. D. and M. J. Bissell (1995). "Dynamic reciprocity revisited: a continuous, bidirectional flow of information between cells and the extracellular matrix regulates mammary epithelial cell function". In: *Biochemistry and Cell Biology* 73.7-8. PMID: 8703411, pp. 391–397. DOI: 10.1139/o95-046. eprint: https://doi.org/10.1139/o95-046. URL: https://doi.org/10.1139/o95-046.

Roux, Clément et al. (2016). "Prediction of traction forces of motile cells". In: *Interface focus* 6.5, p. 20160042.

Rubinstein, Boris et al. (2009). "Actin-Myosin Viscoelastic Flow in the Keratocyte Lamellipod". In: *Biophysical Journal* 97.7, pp. 1853 –1863. ISSN: 0006-3495. DOI: https://doi.org/10.1016/j.bpj.2009.07.020. URL: http://www.sciencedirect.com/science/article/pii/S0006349509012417.

Sabass, Benedikt and Ulrich S Schwarz (2010). "Modeling cytoskeletal flow over adhesion sites: competition between stochastic bond dynamics and intracellular relaxation". In: *Journal of Physics: Condensed Matter* 22.19, p. 194112.

Sabass, Benedikt et al. (2008). "High resolution traction force microscopy based on experimental and computational advances". In: *Biophysical journal* 94.1, pp. 207–220.

Sarvestani, Alireza S (2011). "A model for cell motility on soft bio-adhesive substrates". In: *Journal of biomechanics* 44.4, pp. 755–758.

Savill, Nicholas J. and Paulien Hogeweg (1997). "Modelling Morphogenesis: From Single Cells to Crawling Slugs". In: *Journal of Theoretical Biology* 184.3, pp. 229 –235. ISSN: 0022-5193. DOI: https://doi.org/10.1006/jtbi.1996.0237. URL: http://www.sciencedirect.com/science/article/pii/S0022519396902374.

Schäfer, Matthias and Sabine Werner (2008). "Cancer as an overhealing wound: an old hypothesis revisited". In: *Nature reviews Molecular cell biology* 9.8, pp. 628–638.

Schultz, Gregory S. et al. (2011). "Dynamic reciprocity in the wound microenvironment". In: *Wound Repair and Regeneration* 19.2, pp. 134–148. DOI: 10.1111/j.1524-475X.2011.00673.x. eprint: https://onlinelibrary.wiley.com/doi/pdf/10.1111/j.1524-475X.2011.00673.x. URL: https://onlinelibrary.wiley.com/doi/abs/10.1111/j.1524-475X.2011.00673.x.

Schwarz, Ulrich S and Margaret L Gardel (2012). "United we stand–integrating the actin cytoskeleton and cell–matrix adhesions in cellular mechanotransduction". In: *Journal of cell science* 125.13, pp. 3051–3060.

Seetharaman, Shailaja and Sandrine Etienne-Manneville (2020). "Cytoskeletal crosstalk in cell migration". In: *Trends in cell biology*.

Sens, Pierre (2013). "Rigidity sensing by stochastic sliding friction". In: *EPL (Europhysics Letters)* 104.3, p. 38003.

— (2020). "Stick-Slip model for actin-driven cell protrusions, cell polarisation and crawling". In: *arXiv preprint arXiv:2006.00122*.

Solon, Jérôme et al. (2007). "Fibroblast Adaptation and Stiffness Matching to Soft Elastic Substrates". In: *Biophysical Journal* 93.12, pp. 4453 –4461. ISSN: 0006-3495. DOI: https://doi.org/10.1529/biophysj.106.101386. URL: http://www.sciencedirect.com/science/article/pii/S000634950771696X.

Srinivasan, Manoj and Sam Walcott (2009). "Binding site models of friction due to the formation and rupture of bonds: state-function formalism, force-velocity relations, response to slip velocity transients, and slip stability". In: *Physical Review E* 80.4, p. 046124.

Stroka, Kimberly M. and Helim Aranda-Espinoza (2009). "Neutrophils display biphasic relationship between migration and substrate stiffness". In: *Cell Motility* 66.6, pp. 328–341. DOI: 10.1002/cm.20363. eprint: https://onlinelibrary.wiley.com/doi/pdf/10.1002/cm.20363. URL: https://onlinelibrary.wiley.com/doi/abs/10.1002/cm.20363.

Stéphanou, Angélique et al. (2008). "A computational model of cell migration coupling the growth of focal adhesions with oscillatory cell protrusions". In: *Journal of Theoretical Biology* 253.4, pp. 701 –716. ISSN: 0022-5193. DOI: https://doi.org/10.1016/j.jtbi.2008.04.035. URL: http://www.sciencedirect.com/science/article/pii/S0022519308002130.

Thévenaz, P (2009). *StackReg. Switzerland: École Polytechnique Fédérale de Lausanne; 2009*.

Thielicke, William and Eize Stamhuis (2014). "PIVlab–towards user-friendly, affordable and accurate digital particle image velocimetry in MATLAB". In: *Journal of Open Research Software* 2.1.

Timoshenko, Stephen and J. N. Goodier (1970). *Theory of elasticity*. International Student. Vol. Engineering Societies Monographs. McGraw-Hill.

Tjhung, Elsen, Davide Marenduzzo, and Michael E Cates (2012). "Spontaneous symmetry breaking in active droplets provides a generic route to motility". In: *Proceedings of the National Academy of Sciences* 109.31, pp. 12381–12386.

Tseng, Q (2014). *PIV (Particle Image Velocimetry)-ImageJ plugin*.

Van Helvert, Sjoerd, Cornelis Storm, and Peter Friedl (2018). "Mechanoreciprocity in cell migration". In: *Nature cell biology* 20.1, p. 8.

Wong, Henry C. and William C. Tang (2011). "Finite element analysis of the effects of focal adhesion mechanical properties and substrate stiffness on cell migration". In: *Journal of Biomechanics* 44.6, pp. 1046 –1050. ISSN: 0021-9290. DOI: https://doi.org/10.1016/j.jbiomech.2011.02.004. URL: http://www.sciencedirect.com/science/article/pii/S0021929011000856.

Zhang, Zhiwen et al. (2020). "A minimal mechanosensing model predicts keratocyte evolution on flexible substrates". In: *Journal of the Royal Society Interface* 17.166, p. 20200175.

Ziebert, Falko and Igor S Aranson (2013). "Effects of adhesion dynamics and substrate compliance on the shape and motility of crawling cells". In: *PloS one* 8.5, e64511.

Ziebert, Falko, Sumanth Swaminathan, and Igor S Aranson (2012). "Model for self-polarization and motility of keratocyte fragments". In: *Journal of The Royal Society Interface* 9.70, pp. 1084–1092.